AN ABSTRACT OF THE DISSERTATION OF

Han Song for the degree of Doctor of Philosophy in Materials Science presented on September 15, 2015.

Title: Soft Magnetic Composites for High Frequency Applications

Abstract approved:

_____

Albrecht Jander

Soft magnetic composites, consisting of fine metallic particles in a non-magnetic, insulating matrix, have great potential for integrated inductor and antenna applications. The dielectric and magnetic properties of soft magnetic composites can be tailored by the choice of matrix as well as particle composition, size, and concentration for reduction in device footprint and improvement in performance. In particular, unlike conventional single-phase materials, magnetic anisotropy in the composites can be controlled by choice of particle shape and alignment to overcome the Snoek's limit, enabling both high permeability and high ferromagnetic resonance frequency.

To develop a soft magnetic composite with 1) high permeability, 2) high ferromagnetic resonance frequency, 3) low hysteresis loss, and 4) low eddy current loss, material design considerations are first examined in terms of magnetic particle design and matrix design. The effects of constituent particle shape and alignment, volume fraction, and composite shape on microstructural and magnetic properties are studied in Ni-Fe microdisk composites and $NiFe_2O_4$ nanocomposites. The total magnetic anisotropy of the composites is determined by the sometimes-competing influences of composite demagnetizing field and particle shape anisotropy. To lift the Snoek's limit and obtain simultaneous high permeability and high

ferromagnetic resonance frequency, planar magnetic anisotropy is introduced to the composites by aligning the shape anisotropy of individual Ni-Fe microdisks in an in-plane rotating field. This planar alignment process is investigated by a systemic experimental and theoretical study of magnetic disk rotation in a Newtonian fluid, which yields insights necessary for both alignment process optimization and magnetic anisotropy fine-tuning. Finally, the magnetic alignment process is integrated to an inkjet printer, and magnetic samples with arbitrary aligned anisotropy are demonstrated by printing a magnetic nanoparticle bearing ink.

Soft Magnetic Composites for High Frequency Applications

by
Han Song

A DISSERTATION

submitted to

Oregon State University

in partial fulfillment of
the requirements for the
degree of

Doctor of Philosophy

Presented September 15, 2015
Commencement June 2016

Doctor of Philosophy dissertation of Han Song presented on September 15, 2015

APPROVED:

Major Professor, representing Materials Science

Head of the School of Mechanical, Industrial, and Manufacturing Engineering

Dean of the Graduate School

I understand that my dissertation will become part of the permanent collection of Oregon State University libraries. My signature below authorizes release of my dissertation to any reader upon request.

Han Song, Author

ACKNOWLEDGEMENTS

To my advisors, Dr. Albrecht Jander and Dr. Pallavi Dhagat, thank you for giving me the opportunity of working in your research group, and introducing me to the world of magnetism. I am truly grateful for your guidance and advice in my learning and research. I would also like to thank the rest of my committee: Dr. Julie A. Greenwood, Dr. Brady Gibbons, and Dr. Travis W. Walker. Thank you for your help and feedback on my dissertation. Especially to Dr. Travis W. Walker, thank you for expanding the scope of this work.

I want to thank Dr. Alex Yokochi for the collaboration on the $NiFe_2O_4$ nanocomposite project. I want to thank Hewlett-Packard for supporting the magnetic inkjet printing project. To all the graduate and undergraduate students who made a significant contribution to this work: Mingyang Tan, Garrett Clay, Sam Mulley, Jeremy Spencer, and Nathan Coussens, thank you and it is always a pleasure to work with you. To all my fellow Magnetics Laboratory members, thank you for the helpful discussions and assistance leading up to this result.

To the professors and facility staff I have worked with: Dr. Oleh Taratula, Chris Tasker, Rick Presley, and Teresa Sawyer, thank you for giving me training and access to your lab equipment.

To Weiyang, Shan, Xin, Ren and many others, thank you for all the good times at Corvallis. Especially to Weiyang Li, thank you for all the help on and off campus these 6 years.

Finally I want to thank my parents and my girlfriend, Yan Zhang. Without your support none of this would have been possible.

CONTRIBUTION OF AUTHORS

Dr. Travis W. Walker and Mingyang Tan developed the theoretical model for describing magnetic disk rotation in a Newtonian fluid under an in-plane rotating field (Section 5.2). Jeffrey Nielsen, James Stasiak, and Dr. Vladek Kasperchik from Hewlett-Packard provided the TIPS controller and MICR magnetic ink (Section 6.2.1). Garrett Clay and Jeremy Spencer designed and implemented the magnetic inkjet printing setup (Section 6.2.2). Dr. Alex Yokochi and Nathan Coussens provided the lab tools and potassium bromide binder for the $NiFe_2O_4$ nanocomposite preparation (Section 7.2). Sam Mulley assisted the implementation of Lock-in FMR setup for $NiFe_2O_4$ nanocomposite characterization (Section 7.3).

TABLE OF CONTENTS

TABLE OF CONTENTS (Continued)

TABLE OF CONTENTS (Continued)

Page

TABLE OF CONTENTS (Continued)

Page

LIST OF FIGURES

LIST OF FIGURES (Continued)

LIST OF FIGURES (Continued)

LIST OF FIGURES (Continued)

LIST OF FIGURES (Continued)

LIST OF FIGURES (Continued)

LIST OF TABLES

CHAPTER 1. INTRODUCTION

1.1 High-Frequency Soft Magnetic Applications

With the recent booming of smart devices that rely on wireless communications, such as smartphones, smartwatches, and tablets, there is an increasing demand for faster wireless speed and smaller device size. To meet these demands, the size and performance of on-chip inductor and antenna components in the smart devices play an important role.

The integration of on-chip inductors and antennae with soft magnetic materials of high permeability offers the potential benefits of reduction in device size and improvement in performance [1]. For instance, the length of a quarter-wavelength microstrip antenna [2-3] is determined by

$$\frac{\lambda}{4} = \frac{c}{4f\sqrt{\mu^E \varepsilon^E}}, \tag{1.1}$$

where λ is the wavelength, c the speed of light, f the frequency, μ^E the effective permeability, and ε^E the effective permittivity of the microstrip. With the increased permeability from the integration of a soft magnetic material, the microstrip antenna length can be minimized for portable communication devices. The same effect can also be found in inductors. For a solenoid coil with a magnetic core, the inductance, L, is given by

$$L = \frac{N_c{}^2 \mu A_c}{l}, \tag{1.2}$$

where N_c is the number of turns, A_c the coil area, l the coil length, μ the permeability of the magnetic core. By incresing the permeability, an improved performance can be obtained with the same coil area, or the inductor footprint can be reduced while maintaining the performance [4-6].

However, the onging demands for high data transmission rate (Fig. 1.1) presents a great challenge to these devices. To increase the data transmission rate from the current 1 Gbit/s of 4G mobile network [7] to the proposed 10 Gbit/s of the 5G mobile network, the integrated inductor and antenna components in the wireless

devices must be able to operate at 10 GHz or even higher while maintaining the performance. At high frequency, the current single-phase soft magnetic materials suffer from either high energy loss, or low ferromagnetic resonance (limiting the operating frequency). Development of novel soft magnetic materials possessing both high permeability and high ferromagnetic resonance frequency while keeping a low energy loss are desired.

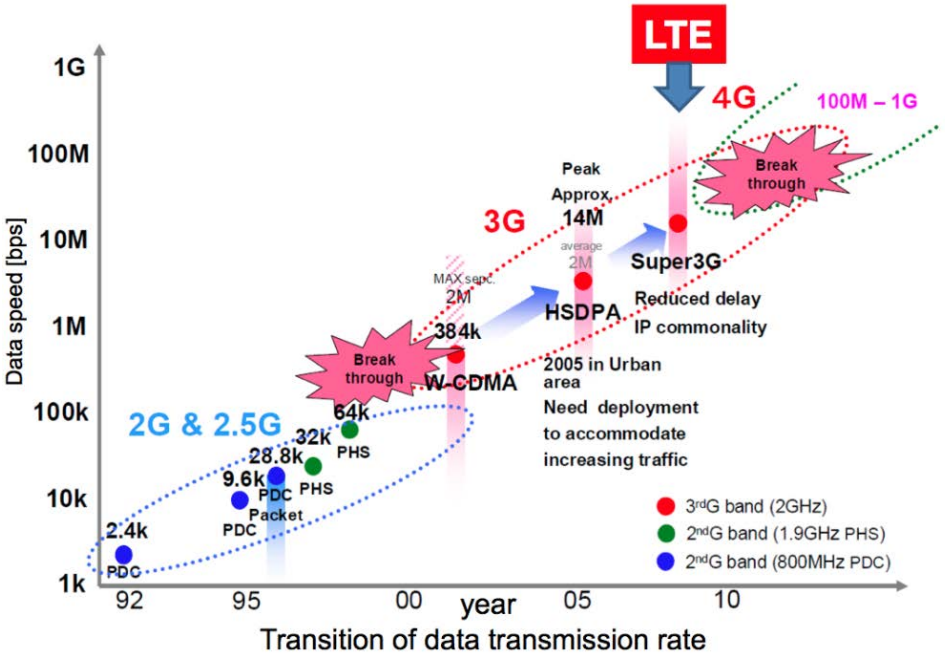

Fig. 1.1 Evolution in data transmission rate. (Reprinted with permission from Miki *et al*. [7].)

1.2 Soft Magnetic Composites

Soft magnetic composites, consisting of fine metallic magnetic particles in a non-magnetic, insulating matrix, can have properties not achievable in traditional, single-phase materials [8-10]. The dielectric and magnetic properties of soft magnetic composites can be tailored to obtain high permeability and low losses by the choice of matrix as well as particle composition, size, and concentration. In particular, unlike conventional single-phase polycrystalline materials, magnetic

anisotropy in the composites can be controlled by choice of particle shape and alignment (Fig. 1.2) to achieve simultaneous high ferromagnetic resonance frequency and high permeability. Furthermore, the versatile fabrication process of soft magnetic composites offers good compatibility with both standard semiconductor process and 3D inkjet printing technique. Other advantages of soft magnetic composites include light weight, good chemical resistance, and moderate mechanical properties.

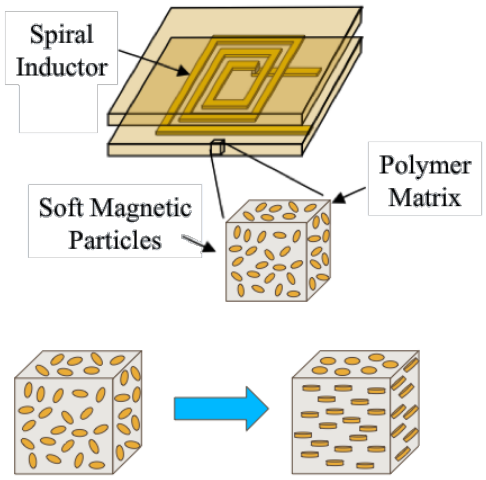

Fig. 1.2 Soft magnetic composites with aligned anisotropic particles for high frequency inductor application.

1.3 Scope of This Work

In Chapters 2 and 3, basic concepts of ferromagnetism are first introduced, and then employed for the discussions of composite optimization in terms of magnetic particle design and matrix design. The optical and magnetic characterization techniques used in this work are presented in Chapter 4.

Magnetic particle design is first studied experimentally in Chapter 5. To investigate the effect of particle shape and alignment on magnetic anisotropy of the composites, Ni-Fe microdisks are fabricated in-lab, dispersed in a UV-curable matrix, and aligned by an in-plane rotating field. To achieve simultaneous high

permeability and high ferromagnetic resonance frequency, planar magnetic anisotropy is introduced to the composites from aligning the individual shape anisotropy of Ni-Fe microdisks. A systematic experimental study of the planar alignment process is conducted by imaging magnetic disk rotations in a Newtonian fluid, and a theoretical model is developed to provide guidelines for process optimization.

In Chapter 6, the magnetic alignment process as well as UV-curing is integrated to an inkjet printer to enable 3D magnetic inkjet printing. Magnetic samples with arbitrary aligned anisotropy are demonstrated by printing and aligning a magnetic nanoparticle bearing ink.

Matrix design by engineering composite volume fraction and shape is explored in Chapter 7. To achieve high volume fractions, commercial $NiFe_2O_4$ nanopowder is used instead because of the large available quantity. The sometimes-competing influences of demagnetizing field and particle anisotropy are examined in $NiFe_2O_4$ nanocomposites.

The International System of Units (SI Units) is used in equations and results throughout this work.

CHAPTER 2. BASICS OF FERROMAGNETISM

2.1 Magnetic Moment

The macroscopic magnetism of materials comes from the magnetic moments associated with individual electrons. Each electron in an atom has two sources of magnetic moments: 1) orbital moment and 2) spin moment [11-12]. These concepts involve some quantum-mechanical principles beyond the scope of this discussion, and hence simplifications have been made. The orbital moment can be seen as a consequence of orbital motion of the electron around the atomic nucleus (Fig. 2.1a). The orbiting electron is considered as a small current loop, generating a magnetic moment along the orbiting axis. Meanwhile, the electron has an intrinsic spin, a quantum mechanical principle that can be simplified as the electron spinning around its own axis (Fig. 2.1b). The electron spin can only have two states: either in spin "up" direction or in an anti-parallel "down" direction. In sum, each electron in an atom may be viewed as a tiny permanent magnet with contribution from both orbital and spin moments.

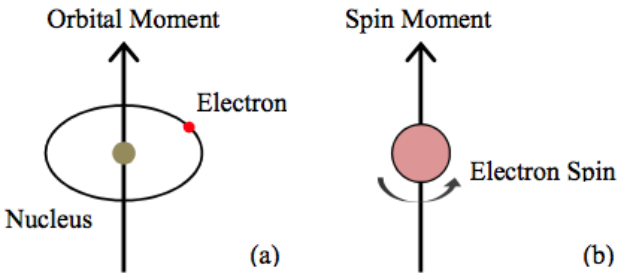

Fig. 2.1 Magnetic moment associated with (a) an orbiting electron, and (b) a spinning electron.

The net magnetic moment from electron orbital and spin motion depends on the atomic electron configuration. The spin moment of an electron with spin "up" will cancel that of one with spin "down". This also holds for the electron orbital motion; some electron pairs cancel each other's orbital moments. Therefore,

only materials with unpaired electrons have a net magnetic moment. Among these materials, only ferromagnetic materials, in which the unpaired electrons become spontaneously aligned due to exchange interaction between spins, exhibit a strong enough magnetic response for practical use.

2.2 Magnetic Hysteresis

Magnetization, M, is a macroscopic property of magnetic moment per unit volume of a sample. To reduce the internal magnetic energy, a ferromagnetic material spontaneously divides into so-called “magnetic domains”, which are small regions with a uniform magnetization direction. Inside magnetic domains, individual magnetic moments of atoms are aligned and pointed in the same direction; while the magnetizations of different domains may point in different directions. When an external magnetic field, H, is applied, domains will rotate their magnetizations to the applied field direction, and grow into larger domains. These two types of magnetization processes are called domain rotation (low energy cost) and domain wall motion (high energy cost), respectively.

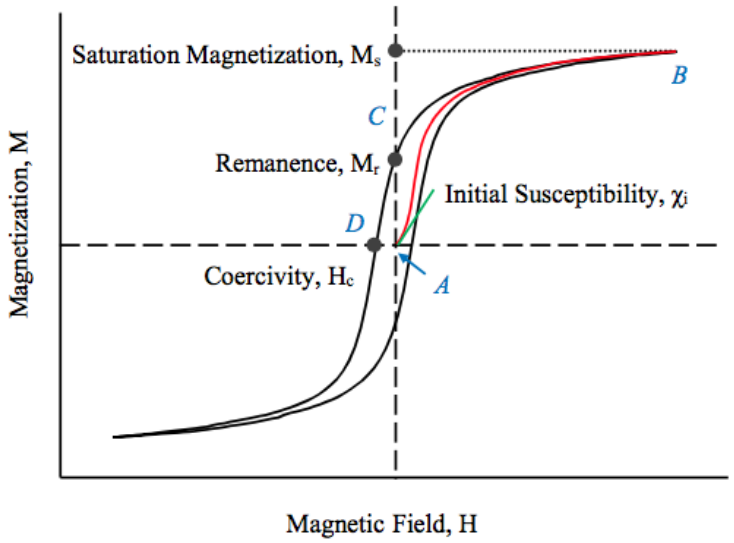

Fig. 2.2 Magnetization, M, versus magnetic field, H, behavior of a ferromagnetic material.

An example magnetization, M, versus magnetic field, H, response of a ferromagnetic material is shown in Fig. 2.2.

Assume the ferromagnetic material starts with the random domain orientations under zero field (point *A* on Fig. 2.2). With increasing magnetic field, H, the magnetization keeps rising following the initial magnetizing curve (red curve). When the magnetic field is strong enough to align all domains in the applied field direction, the magnetization reaches the maximum (point *B*) and will not increase any further with stronger magnetic fields. This is called saturation magnetization, M_s. Subsequently, with decreasing magnetic field the magnetization response follows a different curve (*B*-*C* curve) than the initial magnetizing curve. When reduced back to zero field, rather than being demagnetized, the magnetization holds a remanence M_r (point *C*). To fully demagnetize the material, a coercive field in the opposite direction is required to reverse to zero magnetization, which is called coercivity, H_c (point *D*). This phenomenon is called magnetic hysteresis, and the loop is called a hysteresis loop. The saturation magnetization, M_s, is solely a material dependent property. Remanence, M_r, and coercivity, H_c, are caused by domain wall pinning from imperfections in the materials, such as grain boundaries, dislocations, and impurities.

Due to the extra coercive force required to exceed domain wall pinning, energy will be lost as heat during the magnetization switching. This is called hysteresis loss [13-14]. The power dissipated per unit volume due to the hysteresis, P_h, is given by

$$P_h = f \oint H \, dB = f A_h \,, \tag{2.1}$$

where A_h corresponds to the area enclosed by the hysteresis loop (in unit of J/m^3) in one cycle, and f the magnetization switching frequency. Ferromagnetic materials with high coercivity are called hard magnetic materials and are used to make permanent magnets. Materials with low coercivity are called soft magnetic materials. Due to the low coercivity/low hysteresis loss, soft magnetic material are used in high frequency applications such inductors and antennae.

2.3 Magnetic Susceptibility and Permeability

Magnetic susceptibility, χ, is a measure of the degree of magnetization with a material in response to an applied magnetic field,

$$M = \chi H. \tag{2.2}$$

The slope of the M-H hysteresis curve corresponds to the susceptibility of the material, and its non-linear behavior can be explained by different types of magnetization processes. Following the initial magnetizing curve at a magnetic field close to zero the ferromagnetic material shows an initial susceptibility, χ_i (Fig. 2.2). With increasing magnetic field, the susceptibility reaches its maximum, χ_{max}, which is mainly attributed to the process of multiple domains growing into a single one (domain wall motion). Increasing the magnetic field further will rotate this single domain to the field direction, which causes a relatively small increase in magnetization and a decrease in susceptibility.

Magnetic flux density, B, represents the magnitude of the internal field strength within a material that is subjected to a magnetic field. Assume a linear response,

$$B = \mu_0(M + H) = \mu_0(\chi + 1)H = \mu_0\mu_r H\ . \tag{2.3}$$

where μ_0 is the permeability of free space, which is a constant equal to $4\pi \times 10^{-7}$ H/m. The relative permeability, μ_r, is a dimensionless ratio of the permeability of the material compared to that of free space. Among ferromagnetic materials, metallic materials based on Fe and Ni generally possess the highest relative permeability.

Inductance, representing the ability to store magnetic energy, is a important property for electronic devices utilizing magnetic materials. For a solenoid coil with a magnetic core, the inductance, L, is determined by

$$L = \frac{N_c B A_c}{i} = \frac{{N_c}^2 \mu_0 \mu_r i}{l}\frac{A_c}{i} = \frac{{N_c}^2 \mu_0 \mu_r A_c}{l}\ , \tag{2.4}$$

where N_c is the number of turns, A_c the coil area, l the coil length, i the applied current, and μ_r the relative permeability of the magnetic core. Improvement in the

permeability of magnetic core enables the inductor to accomplish higher inductance/better performance while keeping the same coil area A_c, or a reduction of footprint while sustaining the same inductance.

2.4 Magnetic Anisotropy

Magnetic anisotropy represents the dependence of the internal energy on the direction of spontaneous magnetization. A material with magnetic anisotropy has favorable and unfavorable directions for the orientation of magnetization, which are called the easy axis and the hard axis, respectively. In contrast, a material with zero magnetic anisotropy is isotropic, that is, no preferential direction for spontaneous magnetization.

This diretioncal dependence of magnetic properties is usually a combined results of three different anisotropy sources [13-15]: magnetocrystalline anisotropy, magnetoelastic anisotropy, and shape anisotropy. Magnetocrystalline anisotropy mainly results from spin-orbit coupling, which couples the spin moments to the crystal lattice via orbital electrons and produces preferential directions for the magnetization in the lattice. The anisotropy energy is larger in lattices of low symmetry and smaller in lattices of high symmetry. If the crystal lattice is deformed by a strain, the interaction energy, and hence magneocrystalline anisotropy, can be altered as a result, which creates magnetoelastic anisotropy. Shape anisotropy is derived from long-range dipolar coupling in a non-spherical object, and its origin will be discussed in the next section.

In bulk materials and spherical particles, magnetiocrystalline and magntoelastic anisotropy are the main sources of anisotropy, whereas in thin films and non-spherical particles, shape anistropy can play an important role.

2.5 Demagnetizing Field and Shape Anisotropy

Demagnetization effects arise in magnetic samples of finite size. For example, consider a disk-shaped magnetic sample (Fig. 2.3). Under an external field in the perpendicular (out-of-plane) direction, magnetizing of the sample will induce magnetic poles on the top and bottom surfaces. These magnetic poles in turn generate an internal field opposing the external field. This is the demagnetizing field, H_d, which can be described as

$$H_d = -NM\ , \tag{2.5}$$

where N is the demagnetizing factor in the external field direction. In SI units the demagnetizing factors in any three orthogonal directions add up to 1,

$$N_x + N_y + N_z = 1\ . \tag{2.6}$$

The demagnetizing field reduces the actual field experienced by the sample, and thus lowers the total magnetization.

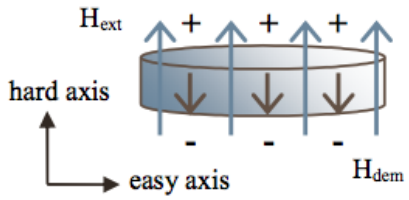

Fig. 2.3 Demagnetizing field in a magnetized disk.

Assuming a uniformly magnetized sample of finite size, Eqn. (2.2) can be written as

$$M = \chi H = \chi(H_{ext} + H_d) = \chi(H_{ext} - NM)\ , \tag{2.7}$$

where H_{ext} is the external field. The demagnetizing factor depends on the separation between magnetic poles on the surface. The perpendicular field induces poles with small separations, generating a strong demagnetizing field and a large demagnetizing factor close to 1. If the field is applied in-plane with the disk,

induced poles are further apart, resulting in a weak demagnetizing field and a low demagnetizing factor close to 0.

The magnetostatic energy from the demagnetizing field, U_d, in a uniformly magnetized sample can be expressed as

$$U_d = \frac{1}{2} NVM^2, \tag{2.8}$$

where V is the volume of the sample. With the external field, H_{ext}, applied along a long axis, the resulting demagnetizing factor is small, and the sample will have a reduced magnetostatic energy compared to the case of external field along a short direction. This directional dependence of demagnetizing fields make it easier to magnetize along a long axis than along a short direction, giving rise to shape anisotropy.

Table 2.1 Demagnetizing factors for different shapes.

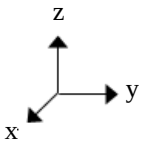

	N_x	N_y	N_z
Sphere 	1/3	1/3	1/3
Thin Disk 	0	1	0
Long Rod 	0.5	0.5	0

A list of demagnetizing factors for different shape can be found in Table 2.1. A spherical sample has all three demagnetizing factors equal to 1/3, showing zero shape anisotropy. A disk-shaped sample possess planar anisotropy with an

easy plane and a hard axis normal to the disk plane; while for a rod-shaped sample, uniaxial anisotropy with one easy axis along rod axis and a hard plane exists for the magnetization.

Demagnetizing fields and demagnetizing factors are uniform only in ellipsoids. For more general shapes, an average demagnetizing factor can be calculated by two methods: magnetometric method and ballistic method. The former employs averaging of demagnetizing factors over the volume of the sample, whereas the later use a cross section perpendicular to the field direction for the calculation. A simple, close-form expression of ballistic demagnetizing factor is obtained for magnetic disks in Ref. [17], and the dependence of demagnetizing factors, both in-plane and out-of-plane, on the aspect ratio is calculated in Fig. 2.4. The aspect ratio, κ, is defined as the ratio of the disk diameter, d, to the disk thickness, h. Magnetic disks with higher aspect ratios are found to have a larger difference between the demagnetizing factors of easy plane and hard axis, offering a stronger shape anisotropy.

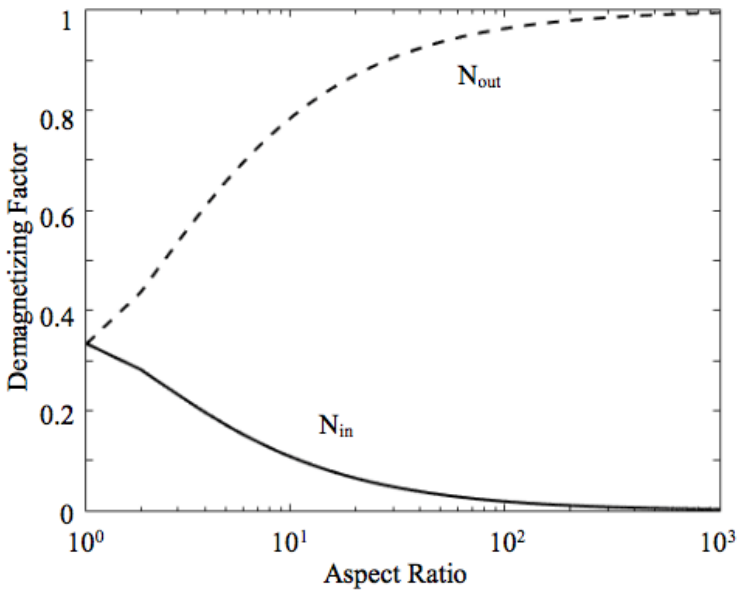

Fig. 2.4 Calculated demagnetizing factor versus aspect ratio for magnetic disks.

The sample's magnetization response to a magnetic field will be affected by the demagnetizing fields. The effective susceptibility, χ^E, which takes account of demagnetizing fields, is derived from

$$M = \chi H = \chi(H_{ext} - NM) = \chi^E H_{ext} , \quad (2.9)$$

$$\chi^E = \chi/(1 + N\chi) . \quad (2.10)$$

The measured effective susceptibilities of disk-shaped Ni-Fe particles are shown in Table 5.1.

2.6 Ferromagnetic Resonance (FMR)

At high frequency, the magnetization of a magnetic material cannot react fast enough in response to the changing magnetic field, causing a phase lag between the two. This phenomenon can be represented by a complex relative permeability, $\mu_r = \mu' - j\mu''$ [18]. The real part of complex permeability, μ', reflects the material's ability to store magnetic energy, whereas the imaginary part, μ'', represents the magnetic energy loss. At a certain frequency known as ferromagnetic resonance (FMR) frequency, f_{FMR}, the imaginary part of complex permeability reaches a peak value as the real part rapidly drops, indicating a maximum energy loss (Fig. 2.5). This frequency, which limits the working frequency of soft magnetic materials, is an important material design consideration.

The ferromagnetic resonance arises from the natural precession resonance of magnetic moments in an external field. Under a static magnetic field, H, the magnetic moments tend to lineup parallel to the field. The precession motion of the magnetization can be predicted by Landau-Lifshitz-Gilbert (LLG) equation [19-21],

$$\frac{dM}{dt} = -\gamma M \times H_{eff} - \frac{\alpha\gamma}{M_s} M \times (M \times H_{eff}) , \quad (2.11)$$

where γ is the electron gyromagnetic ratio (typically, $\gamma/2\pi \approx 28$ GHz/T), and α the damping constant, a dimensionless constant characterizing the damping force opposing the precession. The H_{eff} is the effective internal field experienced by the

magnetization, a combination of the external magnetic field, demagnetizing field, and other anisotropy fields.

As shown schematically in Fig. 2.6, a static field, H, aligns the magnetic moments, as a microwave field, $H_{microwave}$, is applied perpendicular to the static field to make the magnetic moments precess. If the frequency of $H_{microwave}$ matches the natural precession frequency of magnetization, maximum energy will be absorbed by the ferromagnetic sample and transferred to the magnetization precession. This is called ferromagnetic resonance.

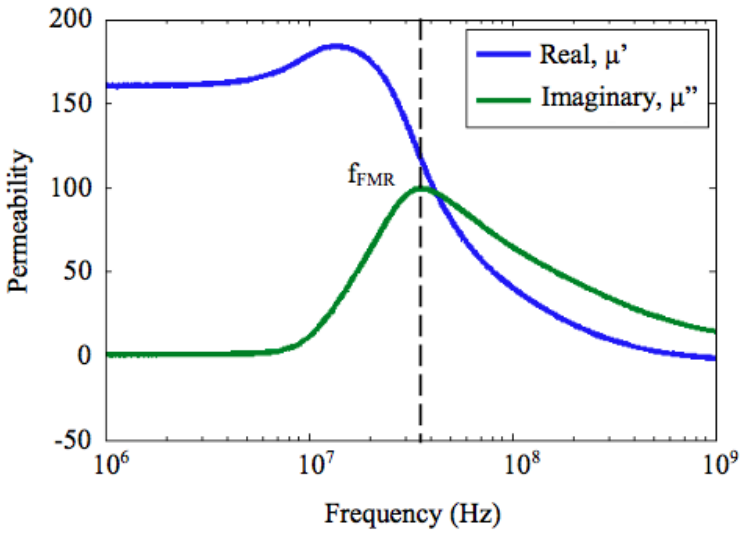

Fig. 2.5 Complex permeability of a ferrite core measured from 1 MHz to 1 GHz.

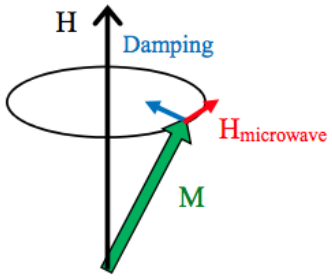

Fig. 2.6 Schematic of magnetization precession around a *dc* magnetic field, H.

Assuming a uniform magnetization precession with a small precession angle (weak microwave field $H_{microwave}$), the ferromagnetic resonance frequency can be solved analytically from the LLG equation (Eqn. (2.11). Two approaches are generally used: the ferromagnetic resonance frequency can be determined either by the coupled differential equations for the time-dependent magnetization components [13,20], or the double derivatives magnetic free energy [21-22]. The ferromagnetic resonance of an ideal bulk magnetic sample without any anisotropy is

$$f_{FMR} = \frac{\gamma}{2\pi}\mu_0 H_r \,. \tag{2.12}$$

The magnetic anisotropy fields from shape anisotropy, magnetocrystalline anisotropy, and magnetoelastic anisotropy would act as an internal magnetic field, H_{int}, and modify the local ferromagnetic resonance condition as

$$f_{FMR} = \frac{\gamma}{2\pi}\mu_0 (H_r + H_{int}) \,. \tag{2.13}$$

If H_r is applied in the same direction of H_{int}, ferromagnetic resonance frequency, f_{FMR}, is shifted higher, yielding a higher working frequency for the material.

The effect of shape anisotropy on ferromagnetic resonance is described by Kittel's equation [20]:

$$f_{FMR} = \frac{\gamma}{2\pi}\mu_0 \sqrt{(H_r + (N_y - N_z)M_s)(H_r + (N_x - N_z)M_s)} \,, \tag{2.14}$$

where N_x, N_y, N_z are the demagnetizing factors in the x-, y-, and z-directions, and H_r is applied in z-direction. Plugging in the demagnetizing factors in Table 2.1, ferromagnetic resonance frequencies in the magnetic sphere, thin disk, and long rod are obtained with H_r applied in the easy axis directions (Table 2.2).

The sphere-shaped magnetic sample shows a ferromagnetic resonance response identical to that of an ideal bulk sample due to the uniform demagnetizing field in all directions. By exploiting the shape anisotropy of magnetic disk and rod, the ferromagnetic resonance frequency is raised above the isotropic case (Eqn. (2.12)) for both geometries.

Table 2.2 Ferromagnetic resonance frequencies for different shapes.

	N_x	N_y	N_z	Kittel's Equation
Sphere 	1/3	1/3	1/3	$f_{FMR} = \frac{\gamma}{2\pi}\mu_0 H_r$ (same as 2.12)
Thin Disk 	0	1	0	$f_{FMR} = \frac{\gamma}{2\pi}\mu_0\sqrt{(H_r + M_s)H_r}$ (2.15)
Long Rod 	0.5	0.5	0	$f_{FMR} = \frac{\gamma}{2\pi}\mu_0(H_r + 0.5M_s)$ (2.16)

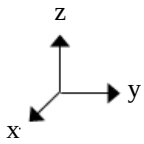

Example FMR responses of Ni-Fe thin films measured in out-of-plane orientation are shown in Fig. 2.7. The FMR microwave power absorption profiles are measured at different frequencies (Fig. 2.7a). A resonance field, H_r, and a full-width-half-maximum linewidth (FWHM), ΔH, can be extracted from each resonance curve. Assume that the sample has an out-of-plane anisotropy field, H_{anis}. For field applied out-of-plane orientation, $N_x = N_y = 0$, $N_z = 1$,

$$f_{FMR} = \frac{\gamma}{2\pi}\mu_0(H_r - M_s + H_{anis}) . \qquad (2.17)$$

The measured resonance field, H_r, versus frequency, f_{FMR}, response shows a linear response as predicted by Eqn. (2.17). The slope of the linear response is equal to $\gamma/2\pi$; the internal magnetic field, $H_{int} = H_{anis} - M_s$, can be extracted from the vertical offset between measured response and the "ideal bulk" response described by Eqn. (2.12).

The FMR linewidth, ΔH, is also frequency dependent as explained below [23-26]

$$\Delta H = \Delta H_{int} + \Delta H_{ext} = \frac{4\pi\alpha}{\mu_0\gamma} f + \Delta H_{ext} . \qquad (2.18)$$

The FMR linewidth has contributions from two mechanisms: intrinsic linewidth from Gilbert damping and extrinsic linewidth from inhomogeneous broadening. The Gilbert damping constant, α, is mostly a material dependent property. While the inhomogeneous broadening is associated with local anisotropy field dispersions and lattice defects caused magnon scatterings.

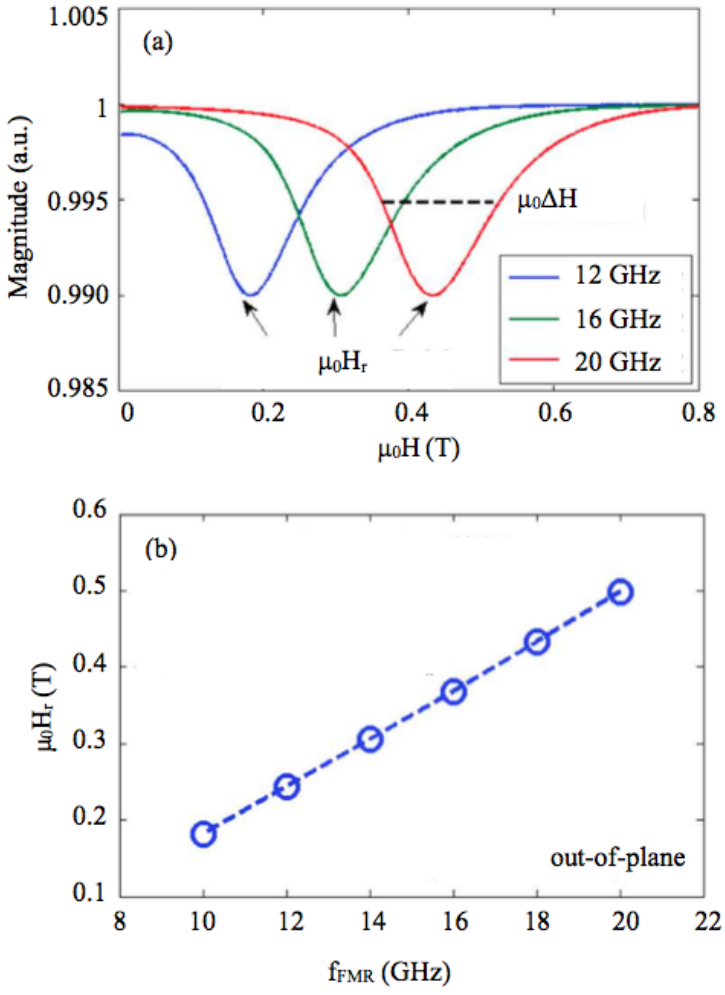

Fig. 2.7 (a) Ferromagnetic resonance absorption profile and (b) resonance field response with varying frequencies.

2.7 Snoek's Limit

According to Eqn. (2.12) the ferromagnetic resonance of an ideal bulk magnetic sample without any anisotropy is

$$f_{FMR} = \frac{\gamma}{2\pi}\mu_0 H_r \, .$$

By solving the LLG equation (Eqn. (2.11)), permeability, μ_r, under an external field of H_r can be written as

$$\mu_r - 1 = \frac{M_s}{H_r} \, . \tag{2.19}$$

Multiply the two equations,

$$\frac{\mu_r - 1}{\mu_0 M_s} f_{FMR} = \frac{\gamma}{2\pi} \, . \tag{2.20}$$

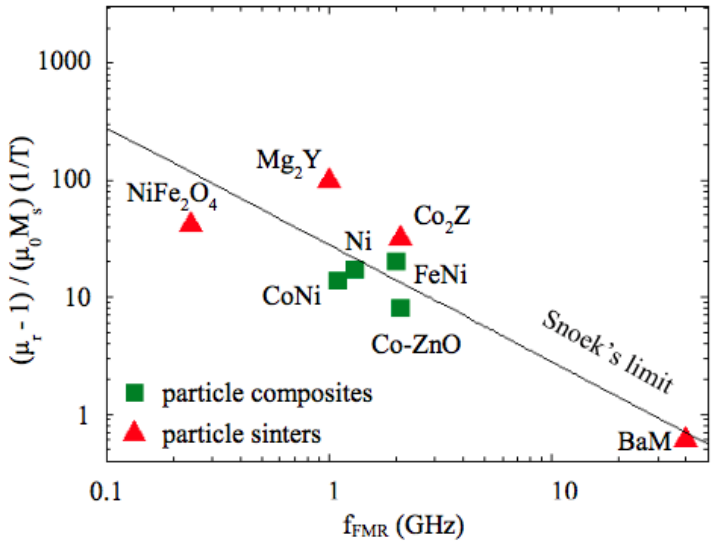

Fig. 2.8 Ratio of $(\mu_r - 1) / (\mu_0 M_s)$ as a function of the resonance frequency, f_{FMR}, for soft magnetic materials with weak anisotropies. (Reprinted with permission from Xue *et al.* [28].)

There exists a trade-off between permeability and ferromagnetic resonance frequency. That is to say, high permeability and high ferromagnetic resonance frequency cannot be reached at the same time. This is called the Snoek's limit [27].

For a soft magnetic material, the f_{FMR} sets the upper limit of working frequency, while $(\mu_r - 1) / (\mu_0 M_s)$ can be seen as a measure of the performance. Snoek's limit presents a trade-off between permeability and working frequency in soft magnetic materials with weak anisotropy (Fig. 2.8), restricting their high frequency performance.

Snoek's limit can be raised by introducing shape anisotropy to the soft magnetic material [28-30]. The Kittel's equation as shown in Eqn. (2.14) is

$$f_{FMR} = \frac{\gamma}{2\pi}\mu_0\sqrt{(H_r + (N_y - N_z)M_s)(H_r + (N_x - N_z)M_s)}\,.$$

Rewrite the Kittel's equation as

$$f_{FMR} = \frac{\gamma}{2\pi}\mu_0\sqrt{H_\theta H_\phi}\,, \text{ with} \tag{2.21}$$

$$H_\theta = H_r + (N_y - N_z)M_s,\ H_\phi = H_r + (N_x - N_z)M_s$$

where H_θ and H_ϕ are the effective field out-of-plane and in-plane with the FMR excitation plane, respectively; the magnetization precession is excited with H_r field applied in z-direction and $H_{microwave}$ in x-direction. Eqn. (2.19) can be rewritten as

$$\mu_r - 1 = \frac{M_s}{H_\phi}\ . \tag{2.22}$$

Then, the Snoek's limit with shape anisotropy is given by

$$\frac{\mu_r - 1}{\mu_0 M_s} f_{FMR} = \frac{\gamma}{2\pi}\sqrt{\frac{H_\theta}{H_\phi}}\,. \tag{2.23}$$

From Table 2.2, the Snoek's limits in the magnetic sphere, thin disk, and long rod are calculated assuming the magnetization precession is excited with H_r field applied in z-direction and $H_{microwave}$ in x-direction (shown in Table 2.3). As expected, the magnetic sphere experiences the same Snoek's limit as that of an ideal bulk due to the zero shape anisotropy. For magnetic materials with uniaxial anisotropy, like a magnetic rod, the high frequency properties are still restricted by the Snoek's limit described in Eqn. (2.20) because $H_\theta = H_\phi$. Only in magnetic samples with planar anisotropy, like a magnetic disk, can achieve $H_\theta > H_\phi$. As a result, the Snoek's limit is lifted proportional to the square root of H_θ / H_ϕ ratio,

enabling high permeability in addition to the already raised ferromagnetic resonance frequency.

Plotted in Fig. 2.9 is the ratio of $(\mu_r - 1) / (\mu_0 M_s)$ as a function of the resonance frequency, f_{FMR}, for magnetic materials with varying planar anisotropies. As the difference between easy plane and hard axis grows larger, the increased anisotropy raises the Snoek's limit higher, yielding the material with improved soft magnetic performance at high frequency.

As for soft magnetic composites, planar anisotropy can be introduced into the material by aligning the constituent oblate- or disk-shaped particles. The more anisotropic that the particle geometry is, the higher Snoek's limit is raised. Walser *et al.* [30] reports a theoretical work on the shape dependence of Snoek's limit in oblate-shaped magnetic particles with varying aspect ratios. With the same resonance conditions (resonance frequency and applied field), a higher fractional increase in the susceptibilities relative to that of a sphere is observed in oblate spheroids with higher aspect ratios (Fig. 2.10), confirming the effect of shape anisotropy on overcoming the Snoek's limit.

Table 2.3 Snoek's limits for different shapes.

	H_θ	H_ϕ	Snoek's Limit
Sphere	H_r	H_r	$\frac{\mu_r - 1}{\mu_0 M_s} f_{FMR} = \frac{\gamma}{2\pi}$ (same as 2.20)
Thin Disk	$H_r + M_s$	H_r	$\frac{\mu_r - 1}{\mu_0 M_s} f_{FMR} = \frac{\gamma}{2\pi} \sqrt{\frac{H_r + M_s}{H_r}}$ (2.24)
Long Rod	$H_r + 0.5M_s$	$H_r + 0.5M_s$	$\frac{\mu_r - 1}{\mu_0 M_s} f_{FMR} = \frac{\gamma}{2\pi}$ (same as 2.20)

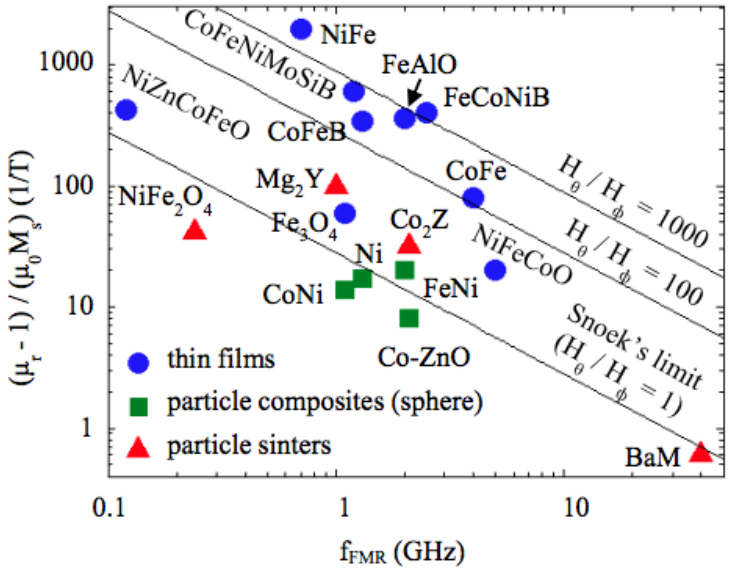

Fig. 2.9 Ratio of $(\mu_r - 1) / (\mu_0 M_s)$ as a function of the resonance frequency, f_{FMR}, for soft magnetic materials with varying anisotropies. (Reprinted with permission from Xue *et al*. [28].)

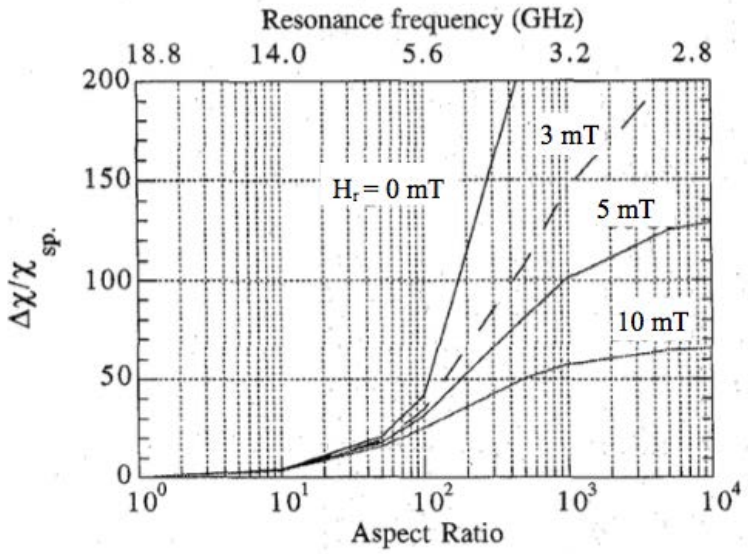

Fig. 2.10 Fractional increase in the susceptibilities of oblate spheroids relative to that of a sphere with varying aspect ratios and applied fields, H_r. (Reprinted with permission from Walser *et al*. [30].)

2.8 Mixing Rules of Magnetic Composites

The above discussions have examined the principles governing high frequency magnetic properties of single-phase materials. For a magnetic composite made from two materials, the interaction between magnetic particles and non-magnetic matrix, and its effect on permeability and ferromagnetic resonance at different mixing ratios must also be taken into consideration.

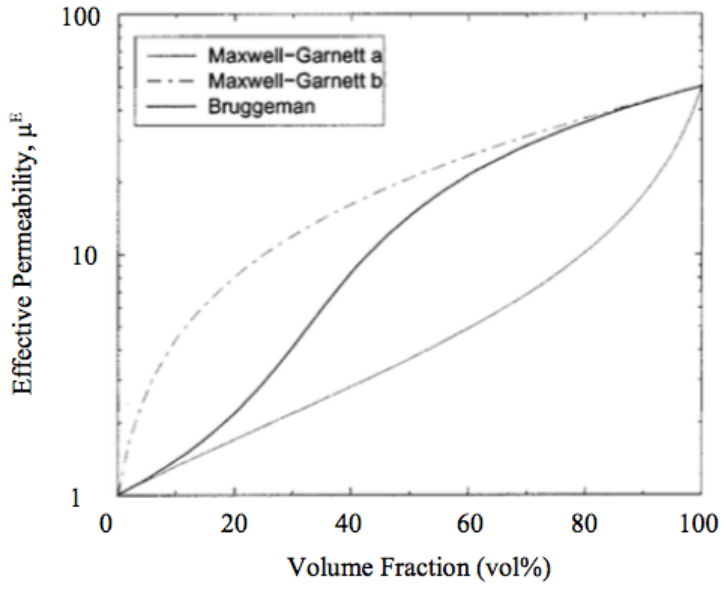

Fig. 2.11 Comparison between the Maxwell-Garnett and the Bruggeman theories for predicting the effective permeability of a composite with spherical particles. $\mu^p = 50$, $\mu^m = 1$. (Reprinted with permission from Ramprasad *et al*. [10].)

First, the composite permeability depends on the volume fraction of magnetic particles. Assuming the magnetic particles are not touching each other, physically or electrically (volume fraction below the percolation limit), the composite's permeability can be enhanced with increasing volume fraction. The effective medium theory is widely used for calculating the effective properties of the composite system [31-33]. For uniformly distributed spherical particles, the

effective permeability, μ^E, of composites can be calculated from the Bruggeman effective medium theory:

$$v\frac{\mu^p-\mu^E}{\mu^p+2\mu^E}+(1-v)\frac{\mu^m-\mu^E}{\mu^m+2\mu^E}=0\,, \tag{2.25}$$

where v is the volume fraction of magnetic particles, μ^p the intrinsic permeability of magnetic particles, μ^m the permeability of the matrix (μ^m = 1 for non-magnetic matrix, such as the acrylic UV-resin and epoxy used in this work).

In case of non-spherical particles, the above equation can be modified as [34]

$$v\frac{\mu^p-\mu^E}{\mu^E+(\mu^p-\mu^E)N}+(1-v)\frac{\mu^m-\mu^E}{\mu^E+(\mu^m-\mu^E)N}=0\,. \tag{2.26}$$

For sphere-shaped particles, N = 1/3, and the above equation is reversed to the original form of Eqn. (2.25).

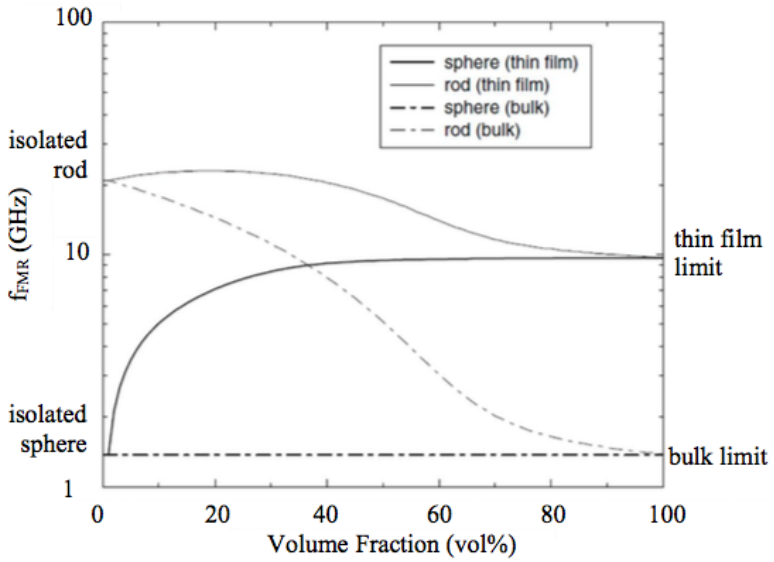

Fig. 2.12 FMR frequency, f_{FMR}, versus particle volume fraction for spherical and rod-shaped particle composites. “Bulk limit” means demagnetizing field is negligible in any direction; “thin film limit” means demagnetizing field is significant only along the film normal. (Reprinted with permission from Ramprasad *et al*. [10].)

The Bruggeman theory works best for moderate volume fractions [35], where the particles and medium have roughly equal amount. As for low volume fractions and high volume fractions, the Maxwell-Garnett theory [34-35] gives better predictions (Fig. 2.11):

Maxwell-Garnett *a*: $\frac{\mu^E-\mu^m}{\mu^E+2\mu^m} = v\frac{\mu^p-\mu^m}{\mu^p+2\mu^m}$ for low v, and (2.27)

Maxwell-Garnett *b*: $\frac{\mu^E-\mu^p}{\mu^E+2\mu^p} = (1-v)\frac{\mu^m-\mu^p}{\mu^m+2\mu^p}$ for high v. (2.28)

Second, the ferromagnetic resonance frequency is determined by the sometimes-competing influences of particle shape, and composite shape. A phenomenological model of high frequency magnetic behavior in composites using an iterative application of the effective medium theory, Landau-Lifshitz spin dynamics and self-consistent calculation of demagnetizing field is developed by Ramprasad *et al*. [9-10]. The bulk magnetic properties of the modeled particles are chosen corresponding to a material intermediate between pure Fe and Fe-Co alloy ($Fe_{80}Co_{20}$). All particles are aligned parallel to the easy axis of the composites, and assumed to have identical properties. The composites are modelded as an infinite bulk as well as a thin film, with the embeded particles having the particle shape of either a sphere or a rod.

The modeled ferromagnetic resonance frequency versus volume fraction response, reproduced in Fig. 2.12, shows that the high frequency magnetic response depends on the particle anisotropy, volume fraction and composite shape in a complex way. At a near-zero volume fraction, the composite demagnetizing field is negligible because the particles are isolated from each other. The ferromagnetic resonance response is dictated by the particle anisotropy, H_{pa}; compared with sphere-shaped particles, the composite with rod-shaped particles possesses an increased f_{FMR} due to the shape anisotropy. On the opposite side of volume fraction, there is the 100 vol% limit, in which the composite becomes a fully dense, single-phase magnetic material. As the volume fraction approaches 100% and the demagnetizing field, H_{dem}, becomes more and more dominant, modeled curves

collapse to the values of either an infinite bulk or a thin film, no matter the shape of constituent particles. In-between these two extreme cases, the ferromagnetic resonance, which is now determined by the relative importance of particle shape anisotropy and composite demagnetizing field at the corresponding volume fraction, exhibits a intermediate response between that of isolated magnetic particles and that of a single-phase magnetic material.

A detailed discussion on material design considerations and optimization of soft magneti composites for high frequency operations can be found in the next Chapter (Chapter 3).

CHAPTER 3. MATERIAL DESIGN CONSIDERATIONS

3.1 Desired Material Properties

For high frequency, soft magnetic applications, the magnetic composites must meet the following demands [36]: 1) high permeability (high inductance), 2) high working frequency (high FMR frequency), 3) low hysteresis loss, and 4) low eddy current loss. The requirements 1) – 3) have already been discussed in the previous chapter. The eddy current loss comes from the eddy currents induced in the composites by a changing magnetic field (Fig. 3.1). According to Faraday's law of induction, a varying magnetic field induces circular electric currents within the material, which generate heat in material of non-zero resistivity as energy loss. The eddy current loss, P_e, is given by:

$$P_e = C_e B^2 f^2 A_e / \rho \,, \tag{3.1}$$

where C_e is a proportionality constant that depends on the material geometry, B the magnetic field strength, f the frequency, A_e the current loop area, and ρ the resistivity. At low frequency, the hysteresis loss is the main source of energy loss; the eddy current loss dominates at high frequencies. The eddy current loss can be minimized by raising resistivity and/or restricting the eddy current paths. For soft magnetic composites, eddy currents are induced both within the constituent particles and in the matrix between particles.

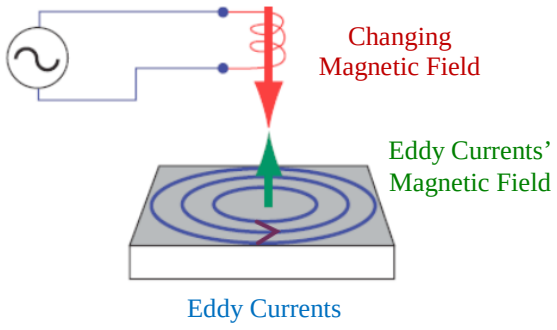

Fig. 3.1 Eddy current loops induced by a changing magnetic field.

The following sections discuss material engineering of soft magnetic composites for high frequency application by both constituent particle design and matrix design.

3.2 Magnetic Particle Design

3.2.1 Particle Material

The choice of particle material is crucial to the high frequency properties of soft magnetic composites, as the hysteresis loss and permeability are mostly material dependent properties. Two types of soft magnetic materials are generally used for high frequency applications: 1) ferrimagnetic materials that are based on ceramic oxides of metals, and 2) ferromagnetic materials based on Fe and Ni. Compared with traditional ferrite materials, ferromagnetic Ni-Fe alloys provides high permeability and low coercivity (low hysteresis loss) for high frequency applications [37-38]. In addition, Ni-Fe alloys offer other advantages like good corrosion resistance and low magnetostriction. Stress-induced anisotropy caused by the fabrication process can be ignored. The disadvantage of Ni-Fe alloys lies in its low resistivity compared with ferrites, which increases the eddy current loss within the particles. A summary of Ni-Fe alloys used in this work can be found in Table 5.1.

3.2.2 Particle Size

The effect of magnetic particle size on coercivity is shown in Fig. 3.2 [38-39]. Transitioning from single-domain to multi-domain, the coercivity of magnetic particles reaches a maximum. For larger particle sizes, the coercivity is lowered as the particle subdivides into domains; while for smaller particle sizes, the randomizing effect of thermal energy on magnetization again reduces coercivity. If the ferromagnetic particles become sufficiently small (15-20 nm for iron oxide), the magnetization can randomly flip directions under thermal fluctuations at room

temperature. The averaged magnetization is zero, and thus the particle exhibits zero hysteresis/coercivity. This phenomenon is called superparamagnetism, in which the material shows a magnetic response similar to those of paramagnetic materials but with a much higher susceptibility.

Smaller particle sizes are preferred for soft magnetic composites because of the shrinking of eddy current loop area and hence the reduction of eddy current loss within the particles. As a result, a higher permeability as well as a reduced loss is observed in magnetic composites with decreased particle sizes [40-41]. Ramprasad *et al*. [9-10] predict in theory that the eddy current loss is negligible below 10 GHz for magnetic particles with a particle size as small as 100 nm. Recently, magnetic composites made with superparamagnetic particles have attracted a lot of interest [41-43]. The benefits include reduced eddy current loss from the small particle size, and minimized hysteresis loss from the near zero coercivity. Also, a higher volume fraction can be obtained in the composites without percolation by using smaller particles.

In this work, the Ni-Fe particle size is limited to micron-size by the feature size of photolithography process in the cleanroom.

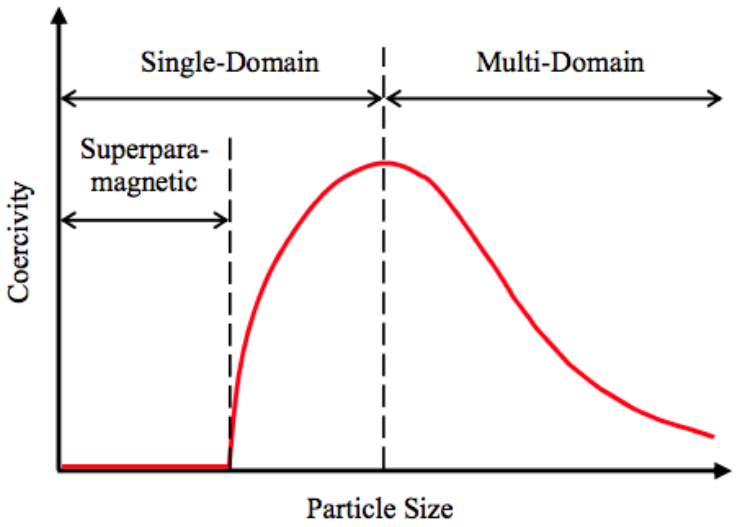

Fig. 3.2 Coercivity dependence of magnetic particle size.

3.2.3 Particle Shape

As discussed in Sections 2.5-2.7, by incorporating rod- or disk-shaped ferromagnetic particles and aligning them in the matrix, the total magnetic anisotropy in the composites can be increased despite the comparatively small magnetocrystalline anisotropy of the particles. Even with random orientations, the anisotropic magnetic particles are reported to improve the composite's soft magnetic properties. In Refs. [44-47], micron-sized, spherical iron-based particles are ball milled for various durations to obtain flake-shaped particles with varying aspect ratios, and then embedded in magnetic composites to compare the soft magnetic properties. With increasing duration of ball milling process, the obtained particles show higher aspect ratios, providing the composites with increased anisotropy and improved permeability.

The disk-shaped magnetic particles are chosen over rod-shaped in this work because 1) it is limited by the photolithography and wet etching fabrication process used in this work, and 2) the disk-shaped particles can help the composites overcoming the Snoek's limit and obtain both high permeability and high ferromagnetic resonance frequency (see Section 2.7). Compared with rod-shaped particles with uniaxial anisotropy, in which magnetization rotates from easy axis to hard plane and creates high loss domain wall movement at high frequency, the disk-shaped particles offer lower loss magnetization rotation in the easy planes of disks, and hence exhibit higher permeability. A summary of dimensions of fabricated Ni-Fe disks can be found in Table 5.1.

3.2.4 Particle Alignment

Aligning the easy planes of disk-shaped magnetic particles inside the composites can further improve the soft magnetic properties. By planar alignment of magnetic disks, 1) Snoek's limit is raised by the induced anisotropy of the whole material, and 2) the eddy current loss is reduced as eddy current loops are limited

to perpendicular to disk planes. Recent experiments presented in Refs. [48-52] explore two-axis alignment. A strong magnetic field is applied for particle alignment while the magnetic flake suspension is rotated till the paraffin wax is solidified. Planar alignment is obtained to some degree from orienting the constituent flake-shaped particles, resulting in an improved permeability and a raised Snoek's limit compared with the unaligned composites. However, the effects of rotating field duration on the composite microstructural and magnetic properties have not been investigated experimentally until this work (see Chapter 5 for details).

3.3 Matrix Design

3.3.1 Matrix Material

Table 3.1 Comparison between insulating polymer matrices.*

Polymer Matrix	Material Requirements			
	High Resistivity	Low Viscosity	On-Demand Curing	Low Shrinkage
Paraffin Wax	√	√	×	×
Epoxy	√	×	×	×
Acrylic UV-Resin	√	√	√	√

* "√" indicates meeting the material requirement; "×" represents failing the material requirement.

The matrix material for soft magnetic composites is required to have 1) high resistivity to reduce eddy current loss between particles, 2) low fluid viscosity before solidification for fast particle alignment process, 3) quick and on-demand solidification to secure the aligned orientations of particles, and 4) low volume shrinkage after solidification to minimize the stress on incorporated particles. Three

types of insulating polymer matrices are considered: paraffin wax, epoxy, and acrylic UV-resin. A summary of material properties is shown in Table. 3.1.

Besides the advantages shown above, acrylic UV-resin also offers good transparency, moderate mechanical properties, and high chemical resistance, making it promising for practical soft magnetic composite applications.

3.3.2 Composite Volume Fraction

With increasing volume fraction of magnetic particles, clustering of particles (particles start touching physically or electrically) lowers the composite's resistivity, and thus raises eddy current loss in the matrix between particles.

Below this percolation limit, the composite's permeability can be enhanced with increasing volume fraction. The effective medium theory predicts higher composite permeability with increasing volume fraction, which is confirmed experimentally in Refs. [47-48,53]. In addition, the experimental work discussed in Chapter 7 demonstrates that the effect of composite shape and orientation grows stronger with increasing volume fractions.

3.3.3 Composite Shape

Similar to particle shape design, the composite shape can be optimized to minimize eddy current loss in the matrix between particles and improve permeability from the composite shape anisotropy [9-10,53].

In conclusion, the soft magnetic composite design considerations are summarized in Table 3.2.

Table 3.2 Design considerations of soft magnetic composites.*

Design Considerations	Desired Material Properties			
	High Permeability	Raise Snoek's Limit	Low Hysteresis Loss	Low Eddy Current Loss
Ferromagnetic Material	√	-	√	×
Small Particle Size	√	-	√	√
Planar Particle Shape	√	-	√	√
Particle Alignment	√	√	√	√
Insulating Matrix	×	-	-	√
High Volume Fraction	√	-	-	×
Planar Composite Shape	√	√	√	√

* "√" represents positive effect, "-"no effect, and "×" negative effect to the desired property.

CHAPTER 4. CHARACTERIZATION TECHNIQUES

4.1 Optical Imaging

4.1.1 Dark Field Imaging of Composite Cross Sections

Dark field optical microscopy is used to image the cross sections of magnetic composites and examine the particle chaining (Section 5.5.7). In contrast to standard bright field microscopy in which the specimen is imaged by the directly transmitted light, dark field microscopy is a specialized technique that excludes the directly transmitted light and capitalizes on the scattered light to enhance contrast.

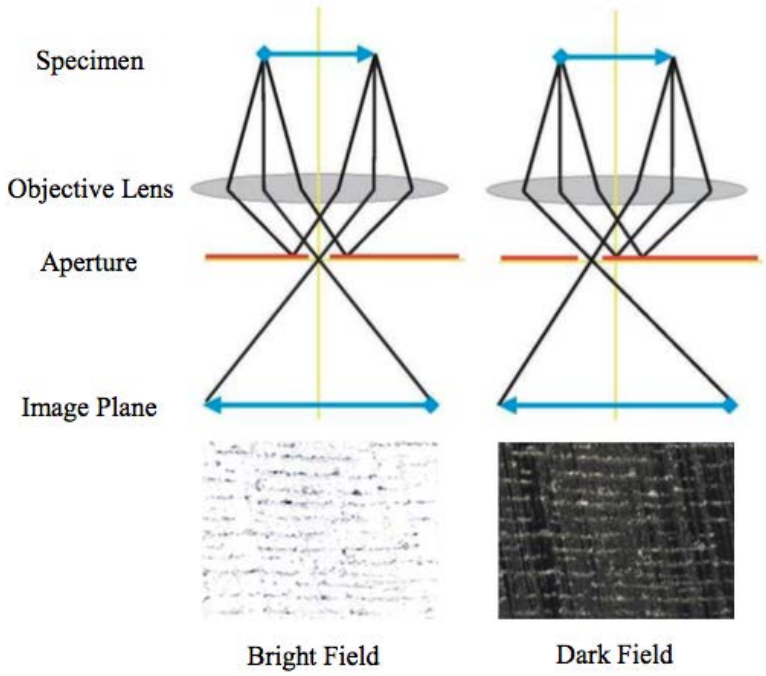

Fig. 4.1 Schematic of optical microscopy bright field and dark field configurations.

As shown schematically in Fig. 4.1, standard bright field microscopy relies upon the light intensity difference in the directly transmitted light to produce contrast, which is dependent on the refractive index and opacity of the specimen.

For a specimen that has a refractive index very close to the surroundings, the bright field microscopy produces low contrast.

Dark field microscopy, however, blocks the direct light from the specimen, capturing only oblique light scattered by the specimen to form an image. As a result, the specimen appears bright in a dark background, which greatly enhances the contrast. This technique is ideal for revealing outlines, edges, and boundaries in a specimen containing very low inherent contrast in bright field microscopy. For example in Fig. 4.1, when observing the formation of magnetic particle chaining layers in a composite, dark field microscopy produces an image with much improved contrast compared with bright field microscopy.

4.1.2 Video Capture of Magnetic Particle Motion

I have designed and implemented a three-axis electromagnet that fits on an optical microscope (Eclipse Ti-S, Nikon Instruments Inc., NY, USA) for applying the aligning field and capturing the magnetic particle motion (Fig. 4.2). To investigate the dynamics of magnetic particles in fluids, magnetic disks are dispersed in silicone fluid standards (Brookfield Engineering Laboratories, Inc., MA, USA).

The suspension, labeled as “Sample” in Fig. 4.2b, is contained in a transparent cuvette tube (UV Cuvette ultra-micro, BrandTech® Scientific, CT, USA) and placed inside the three-axis electromagnet. The suspension is illuminated by the microscope light from the bottom, and the transmitted light is observed by a specialized objective lens (CFI Super Plan Fluor ELWD Objective Lens, Nikon Instruments Inc., NY, USA). The objective lens comes with a correction ring, which can be used to compensate spherical aberration caused by viewing through the tube and the medium. Videos of the magnetic particle motion are captured at 1292 × 964 resolution and 30 frame/s with a microscope camera (Guppy Pro F-125, Allied Vision, PA, USA).

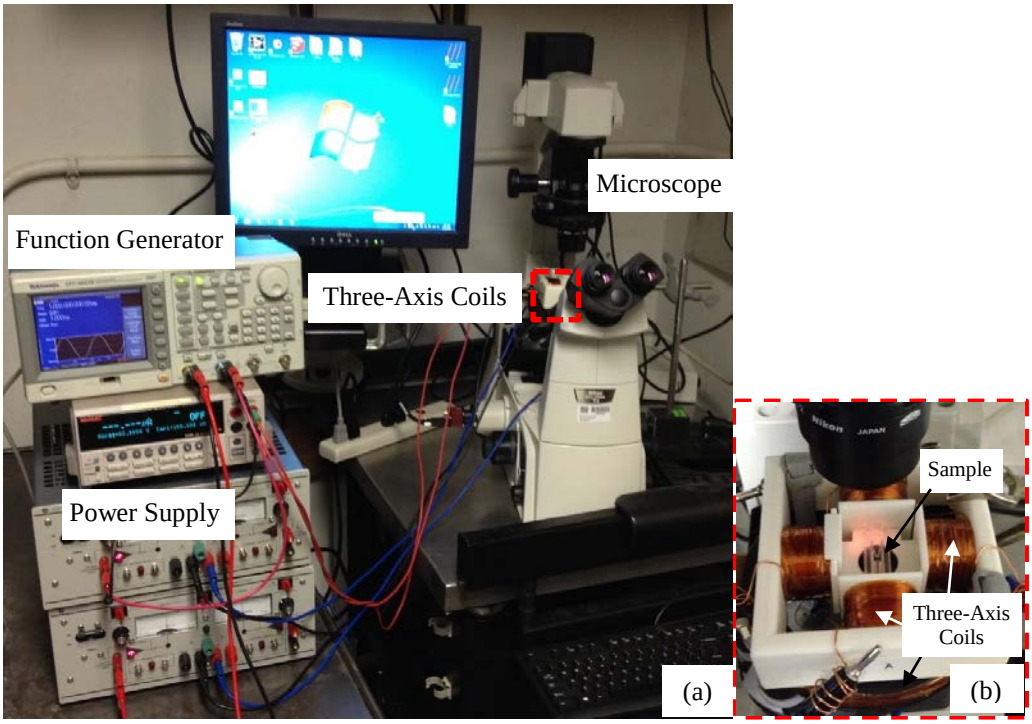

Fig. 4.2 (a) An optical microscope fitted with a three-axis electromagnet for video capture of magnetic particle motion. (b) A three-axis electromagnet for generating the aligning magnetic field.

The three-axis electromagnet is connected to the power supplies, and controlled by a LabVIEW program. Two KEPCO power supplies (BOP 20-20ML, KEPCO, Inc., NY, USA) are used to drive the in-plane coils, and their voltage outputs are under analog control of an arbitrary waveform generator (AFG3022B, Tektronix, Inc., OR, USA). The arbitrary waveform generator is in turn controlled by the LabVIEW program, and an in-plane rotating field is generated by applying two sine wave signals with a 90° phase difference to the two sets (in x- and y-directions) of in-plane coils. The perpendicular coil is powered by a power supply (2440 5A Sourcemeter, Keithley Instrument, OH, USA) to generate a constant perpendicular field.

As shown in Fig. 4.3, I have written a Matlab code (see Appendix C for details) for processing and analyzing the captured videos of magnetic disk rotation, which consists of four major steps:

1) The images are first normalized (pixel intensity normalization), stabilized (remove the vibrations caused by the power supplies), and cropped around the magnetic particle.
2) A luminance threshold is set to turn the images into binary; pixels with luminance greater than the threshold are turned into white (luminance = 1), while the rest pixels are turned into black (luminance = 0).
3) The edges of the binary magnetic particle are detected and fitted to an ellipse. As a result, the projected area of magnetic particle on the image plane can be obtained at each frame.
4) Define the angle between the magnetic disk plane and image plane to be θ. The projected area is linearly proportionally to cos θ. As the magnetic disk rotates toward in-plane orientation ($\theta \rightarrow 0$), the projected area expands due to the increasing cos θ. At last when the particle is perfectly aligned in-plane, the projected area reaches the maximum ($\cos \theta = 1$). By comparing the projected area with the maximum area at each frame, the particle orientation can be tracked over time.

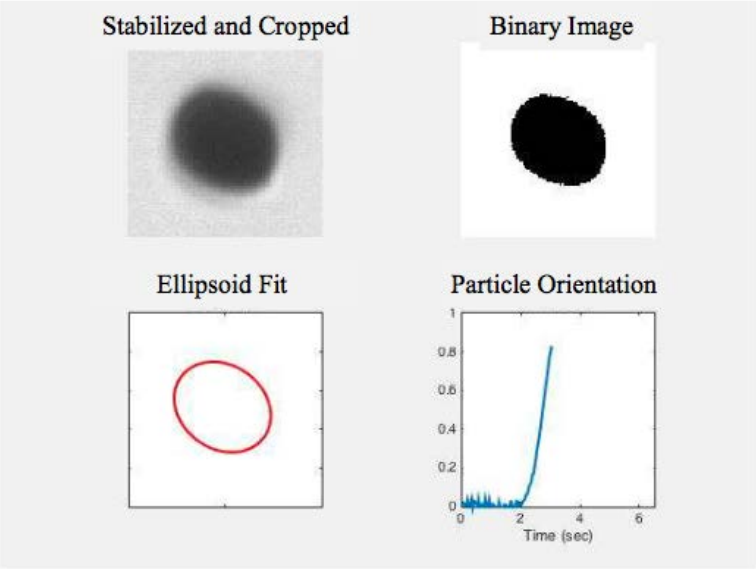

Fig. 4.3 Processing and analysis of the captured magnetic disk rotation in fluids.

The obtained cos θ versus time data can be further analyzed to extract the alignment time, Δt, which is defined as the time for cos θ to change from 0.1 to 0.9, and used to study the particle alignment dynamics at different conditions (see Section 5.5).

4.2 Magnetic Characterizations

4.2.1 Vibrating Sample Magnetometry (VSM)

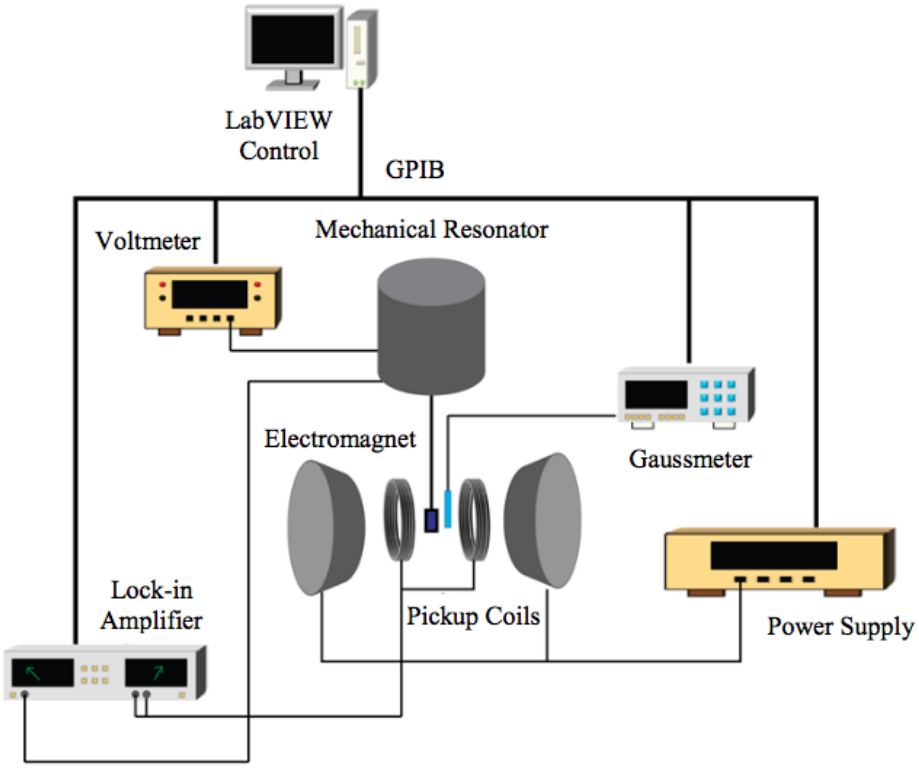

Fig. 4.4 Schematic of a vibrating sample magnetometer (VSM) setup.

Magnetic hysteresis loops can be measured by a vibrating sample magnetometer (VSM), which is originally developed by Foner [54-55]. As shown in Fig. 4.4, a magnetic sample is placed inside an electromagnet, which applies a uniform magnetic field, H, to magnetize the sample. The sample is then physically

vibrated sinusoidally by a mechanical resonator. The magnetic flux from the sample is in turn changing sinusoidally, which can be detected by pick-up coils. The resulting voltage induced in the pick-up coils, V_{pickup}, is proportional to the magnetic moment, m, of the sample.

$$V_{pickup} = 2\pi f N_c m A C_s \sin(2\pi f t) , \quad (4.1)$$

where N_c is the number of turns in pick-up coils, A is the amplitude of oscillation, f the frequency of oscillation, and C_s the sensitivity constant of pick-up coils.

This induced voltage, V_{pickup}, is amplified and detected by a lock-in amplifier, in which the reference frequency is set to be the same as the mechanical vibration frequency. The magnetic moment of the sample is calculated from the detected V_{pickup} using Eqn. (4.1), and plotted versus the applied field, H, to produce the hysteresis loops. A magnetic standard sample with a known magnetic moment is measured to calibrate the pick-up sensitivity constant, C_s, before making the measurement.

The lab-built VSM used for hysteresis measurement in this work has a maximum field strength of ±0.7 T, a field resolution of 0.5 mT, and a minimum detectable magnetic moment of 10^{-8} Am^2, which is about the magnetic moment of 0.04 mg iron. The VSM sample dimension is limited to 1 cm by 1 cm with 1 mm maximum in thickness.

4.2.2 High Frequency Permeability Measurement

Conventionally, the magnetic permeability is measured by winding wires aournd the magnetic core and deriving the effective permeability from its inductance. An alternative inductance measurement method using a 7 mm coaxial line can be implemented on Agilent E4991A RF impedance/material analyzer (Keysight Technologies, CA, USA) by installation of an Agilent 16454A magnetic material test fixture (Fig. 4.5). The magnetic sample needs to be molded into a toroid, and inserted into the test fixture (Fig. 4.6). As a result, an ideal, single-turn inductor, with no flux leakage, is formed, and the permeability can be derived from

the measured inductance of the sample loaded fixture. This measurement technique has a wide frequency from 1 kHz to 3 GHz, and the build-in software of impedance analyzer enables direct readouts of complex permeability.

The self-inductance in the test fixture without the toroid sample, L_{short}, is determined by

$$L_{short} = h_0 \frac{\mu_0}{2\pi} \ln \frac{e}{a}, \tag{4.2}$$

where h_0 is the height of test fixture, a the diameter of the 7 mm terminal, and e the inner diameter of test fixture.

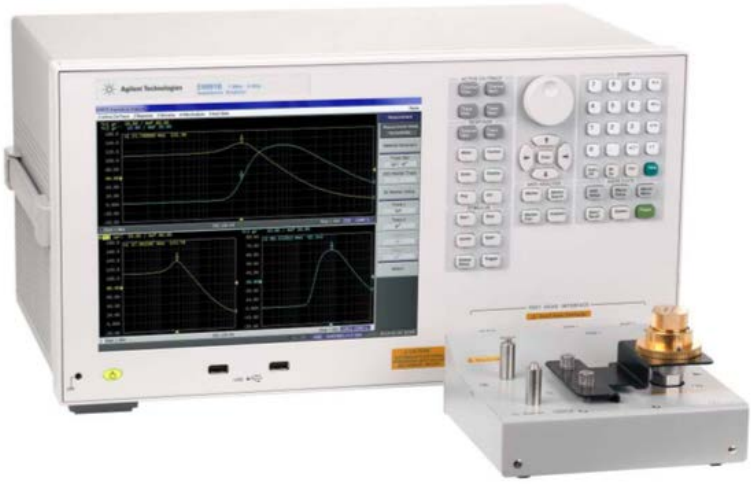

Fig. 4.5 Photo of Agilent E4991A RF impedance/material analyzer equipped with an Agilent 16454A magnetic material test fixture (photo courtesy of Keysight Technologies).

If the toroid sample is inserted into the test fixture, the self-inductant now becomes

$$L = \frac{\mu_0}{2\pi} (\mu_r - 1) h \ln \frac{n}{b} + \frac{\mu_0}{2\pi} h_0 \ln \frac{e}{a}, \tag{4.3}$$

where μ_r is the permeability of the toroid sample, h the height of toroid sample, n the outer diameter, and b the inner diameter.

Using Eqns. (4.2) and (4.3), the relative permeability of the toroid sample can be calculated from

$$\mu_r = \frac{2\pi\,(L - L_{short})}{\mu_0 h \ln(n/b)} + 1. \tag{4.4}$$

The toroid sample should have a low permittivity; thus, the measured impedance has a negligible amount of capacitance. Otherwise, the resulting parallel LC circuit causes an impedance-resonance at a certain frequency, interferring with the precise measurement of impedance.

In this work, toroid samples are made by mixing magnetic particles with either acrylic UV-resin or epoxy, and curing the suspension in a toroid mold. The dimensions of toroid samples can be found in Table 4.1.

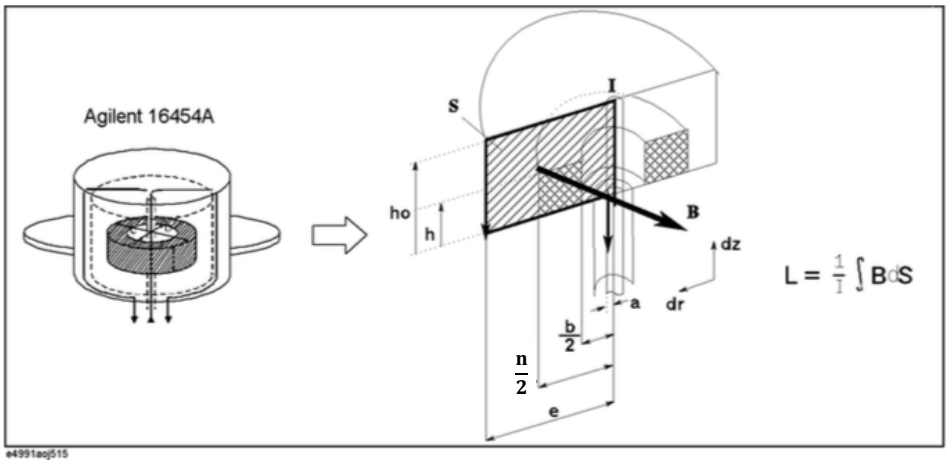

Fig. 4.6 Schematic of measurement principles of Agilent 16454A magnetic material test fixture (photo courtesy of Keysight Technologies).

Table 4.1 Dimensions of toroid samples for permeability measurement.

Magnetic Particles	Matrix	n (mm)	b (mm)	h (mm)
Ni-Fe Microdisks	Acrylic UV-Resin	8.0	5.0	1.0
$NiFe_2O_4$ Nanopowder	Epoxy	7.2	3.6	3.0

4.2.3 Ferromagnetic Resonance Spectroscopy

Ferromagnetic resonance spectroscopy is an accurate and versatile experimental technique for probing magnetization dynamics. Ferromagnetic properties, such as anisotropy, gyromagnetic ratio, and damping constant, can be extracted by analyzing multiple FMR responses measured at different conditions (see Section 2.6).

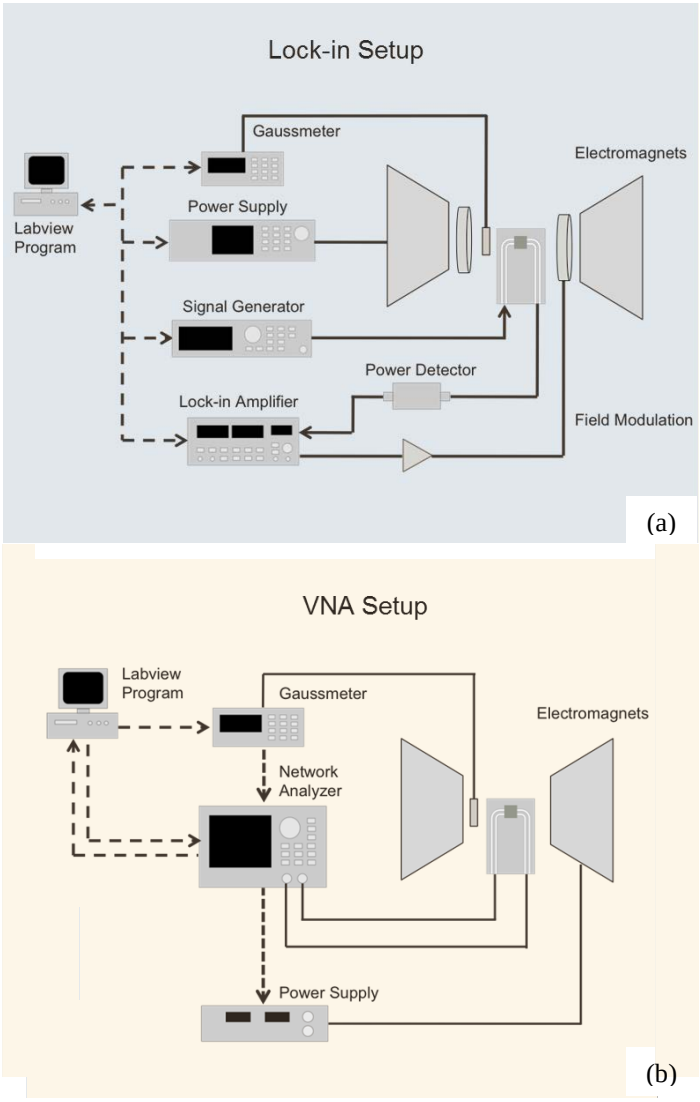

Fig. 4.7 Comparison between lock-in FMR setup and VNA-FMR setup.

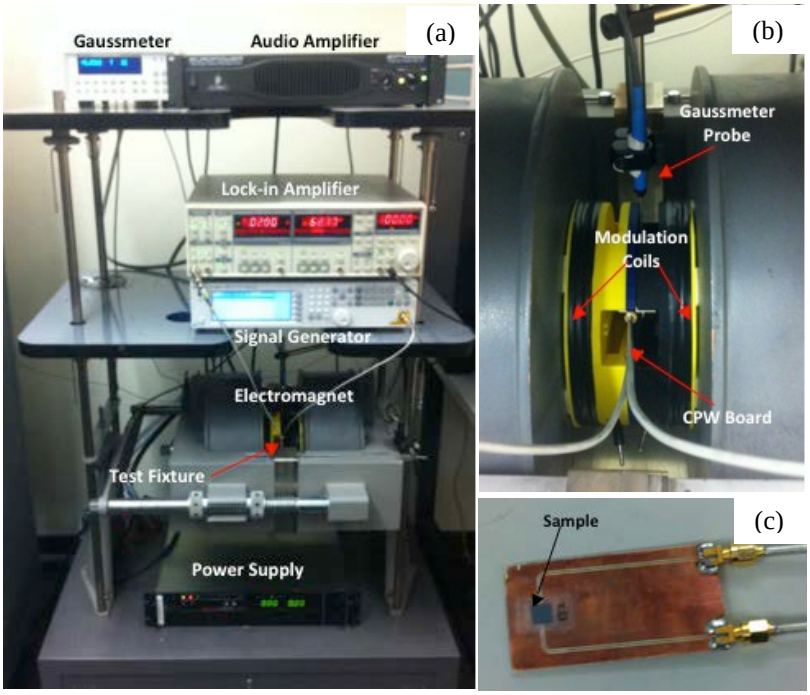

Fig. 4.8 (a) Photo of lock-in FMR setup. (b) Zoom-in photo of CPW board fixture. (c) 1st version U-shaped CPW board loaded with the sample.

I have designed and implemented two types of broadband FMR experimental setups for magnetic composite characterization [56]: lock-in detection FMR setup (lock-in FMR) and vector network analyzer FMR setup (VNA-FMR). The two experimental setups are compared in block diagram in Fig. 4.7, and reviewed in details below.

Photos of the lock-in detection FMR setup are shown in Fig. 4.8. The magnetic sample under study is first mounted on the center trace of a 50 Ω, U-shaped coplanar waveguide (CPW) (Fig. 4.8c). An insulating spacer is placed below the sample to prevent shorting of the CPW. The sample along with the CPW board is then inserted inside the test fixture pressed between two electromagnet pole pieces (Fig. 4.8b). The electromagnet is driven by a power supply to apply a *dc* magnetic field, H, up to 0.9 T. The CPW board can be placed either parallel (in-plane) or perpendicular (out-of-plane) with the *dc* field, enabling FMR investigation of sample geometry. The waveguide is excited at a constant frequency

using a microwave signal generator (Agilent N5183A, 100 kHz - 20 GHz frequency range, Keysight Technologies, CA, USA) to generate a transverse microwave field, $H_{microwave}$, at the sample, while the *dc* field, H, is swept to locate the resonance field. The microwave field, $H_{microwave}$, is kept low to ensure small angle excitation of magnetization precession, which limits the sample geometry to thin films; the sample size is limited to 10 mm by 10 mm.

At the resonance point, maximum microwave power is absorbed by the ferromagnetic sample, which can be detected by a power detector. To detect this very small power absorption, a modulation scheme and a lock-in amplifier (SR830, Stanford Research Systems, CA, USA) are employed. A small modulation field (3 mT, 100 Hz) is added to the *dc* field. The induced oscillations in absorbed power is detected by the power detector, and extracted by the lock-in amplifier at the modulation frequency. As a result, rather than the absorbed power, the field derivative of absorbed power (dP / dH) is measured as a function of the *dc* field (see Fig. 7.5 for example). The zero crossing of the signal corresponds to the peak in power absorption and thus, identifies the resonance field. Assuming the power absorption profile to be Lorentzian, the peak-to-peak linewidth can be converted to FWHM linewidth using the equation below,

$$\Delta H = \sqrt{3}\,\Delta H_{pp} \,. \tag{4.5}$$

The above measurement is repeated at different excitation frequencies to assess the magnetic anisotropy.

The lock-in FMR setup is simple to implement, and the measured FMR response is generally undistorted and symmetric. However, this technique has limited sensitivity.

The VNA-FMR approach uses a vector network analyzer for both microwave signal excitation and FMR signal detection (Fig. 4.9a). Instead of microwave signal generator and power detector in the lock-in setup, the sample loaded U-shaped CPW is connected to an Agilent network analyzer (Agilent N5224A-200, Keysight Technologies, CA, USA). The scattering parameters (S-

parameters), especially S_{21} which is a measure of transmitted microwave power through CPW, are measured at a constant frequency while sweeping the *dc* field. The microwave power absorption profile can be extracted from the field dependent S-parameters to locate the resonance. Higher sensitivity is achieved, as it takes advantage of the full amplitude and phase analysis capability of vector network analyzer. The Agilent network analyzer also provides a broader frequency range up to 43.5 GHz.

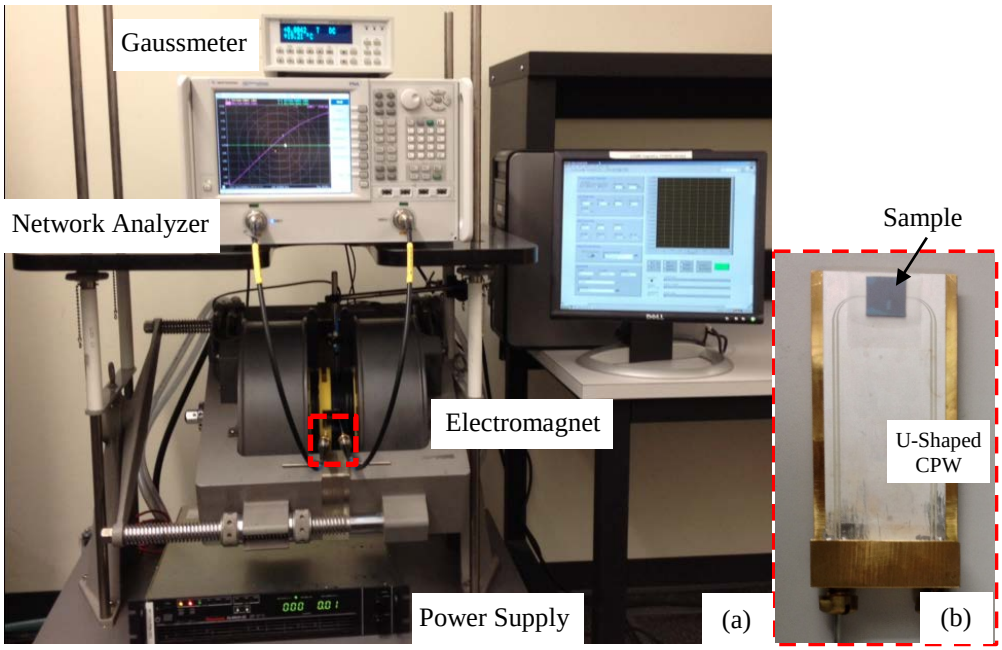

Fig. 4.9 (a) Photo of VNA-FMR setup. (b) 2nd version U-shaped CPW board with improved design.

A 2nd version CPW board with improved design (Fig. 4.9b) is used to further improve the sensitivity and reduce loss: 1) the connections from cable to CPW are optimized to improve the impedance matching; 2) the CPW is patterned on an Alumina (Al_2O_3) substrate, which offers lower dielectric loss; and 3) The CPW center trace is tapered to improve sensitivity.

This approach, however, requires a careful calibration and proper subtraction of reference signals in order to obtain accurate results from the magnetic

sample [56-58]. The S-parameters measure the response from all components between the two ports of network analyzer, including microwave cables, CPW board, and the magnetic sample. To isolate the absorption from the magnetic sample, prior to the sample measurement, 1) a full two-port calibration to the end of the cable is carried out, and 2) reference measurements of unloaded CPW board, or CPW board loaded with a blank substrate, are measured using the same settings as the sample measurement for de-embedding. The reference measurement could show a dependence of the *dc* field, which may be caused by electron paramagnetic resonance in the waveguide and cables, or ferromagnetic contamination.

Two methods have been employed to isolate the magnetic sample response from the CPW board: simply dividing the measured S_{21} parameter by that of the reference measurement [56-57], or a more complete de-embedding using all four S-parameters [58]. The first method works well for samples with large signals and low distortion from waveguide non-idealities. Otherwise, the second method is employed for accurate anisotropy and FMR linewidth measurements.

CHAPTER 5. EFFECT OF PARTICLE ALIGNMENT

5.1 Introduction to Magnetic Particle Alignment

As discussed in Sections 2.7 and 3.2, the Snoek's limit can be overcome with induced planar anisotropy from aligning oblate- or disk-shaped particles, making the composite material possessing both high permeability and high FMR frequency. Magnetic particle alignment, which applies an external magnetic torque to align the easy axes of constituent magnetic particles inside the composites, is a rapid, non-contact, and energy efficient method compared with other particle manipulation techniques [59]. Acquiring uniaxial anisotropy from constant field alignment has been well studied both theoretically and experimentally [59-62]. More complex forms of magnetic alignment, like planar alignment by a rotating field or a pulsed field, are being increasingly investigated for 2-axis or even 3-axis alignment of magnetic particles [63-71].

In this work, a detailed experimental and theoretical study of the alignment dynamics of magnetic disks in an in-plane rotating field is conducted. A theoretical model is developed to describe the rotation of an isolated disk suspended in a Newtonian fluid in response to a rotating field. The model is experimentally examined by imaging disks alignment behavior in silicone fluid standards while systematically varying 1) fluid viscosity, 2) aligning field strength and rotation frequency, 3) disk size and magnetic susceptibility, and 4) volume fraction. The effect of aligning field duration and particle chaining on planar anisotropy is further studied in Ni-Fe microdisk composites, which is made from aligning Ni-Fe microdisks in a UV-curable matrix and curing the suspension to fix the particle orientations. Combined, the modeling and experimental results yield the insight necessary for both optimzation of planar alignment process and fine-tuning of magnetic composite anisotropy.

5.2 Hydrodynamic Model

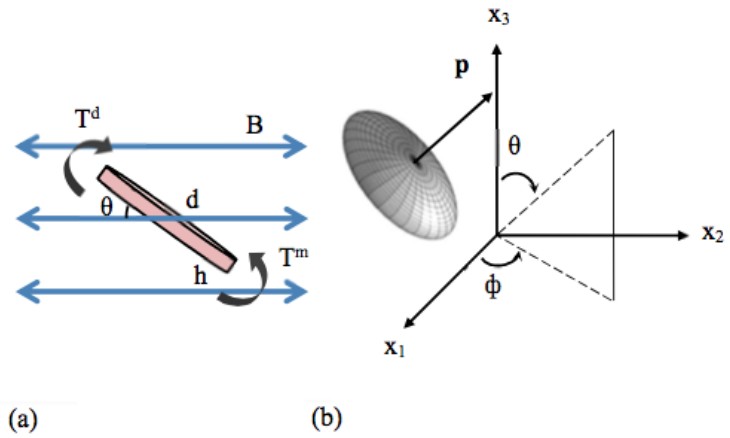

Fig. 5.1 (a) Schematic of torque balance on a magnetic disk in a viscous fluid. (b) The disk is approximated as an oblate-ellipsoid with orientation vector, **p**.

To enable understanding of the hydrodynamic behavior of disk-shaped particles in a Newtonian fluid at small Stokes numbers, a theoretical model is developed based on the assumptions of 1) quiescent flow field, 2) viscous forces dominating over the inertial force of an isolated disk (low-Reynolds-number Stokes flow), 3) oblate-ellipsoid approximation of the disk-shaped particle, and 4) negligible Brownian motion for the micron-sized particle. The following modeling work is done by Mingyang Tan and Dr. Travis W. Walker from Chemical Engineering, Oregon State University.

The forces exerted on the particle are gravity, magnetic force, and hydrodynamic drag. In this study, 1) the particle is far (at least 10 times particle size) away from the cuvette wall, and the ratio between sedimentation time to alignment time is over 10^3 for Ni-Fe microdisks, making the sedimentation effect negligible; 2) the disk suspension is prepared with a very low volume fraction of 10^{-5}, a fraction much smaller than necessary to assume hydrodynamic interactions between particles; 3) since the aligning field has a variation <5% over the sample area and the volume fraction is very low, the time for a particle to move a distance of 10 times particle size by the magnetic force is much (about 10^4 times) longer

than the alignment time, confirming the particles are magnetically isolated.

The rotary Péclet number, Pe_r, which characterizes the relative importance of the imposed magnetic torque and Brownian motion, is very high ($\mathcal{O}(10^4)$) in this study. Thus, randomizing torque from Brownian motion [72] is negligible. Dipole interactions between the magnetic disks are also not included. As shown in Fig. 5.1a, there are only two torques left on an isolated disk: magnetic (T^m) and viscous drag torques (T^d). The magnetic torque, T^m, rotates the disk easy axis parallel to the external field, while the viscous drag torque, T^d, opposes this rotation. The resulting torque balance is therefore simply

$$T^d = T^m, \text{ or}$$

$$C_{ij}\omega_j = \varepsilon_{ijk} m_j B_k \,, \tag{5.1}$$

such that C_{ij} is the viscous resistance tensor; ω_j the angular velocity; ε_{ijk} the Levi-Civita tensor; m_j the magnetic moment; and B_k the magnetic field. Aspect ratio, κ, is defined as the ratio of the disk diameter, d, to the disk thickness, h. If aspect ratio $\kappa >> 1$, then $C_{ij} = \delta_{ij}\zeta_r$, where δ_{ij} is the Kronecker delta, and ζ_r the rotational mobility [73]. The orientation vector, **p**, is defined as a unit vector directed at the axis of symmetry of the ellipsoid (Fig. 5.1b). The effective susceptibility tensor has two components: $\chi_{\parallel}^{E}$, which is parallel to **p** (magnetic hard axis), and $\chi_{\perp}^{E}$, a component perpendicular to **p** (magnetic easy axis). Then, m_j can be described as $m_j = \frac{V}{\mu_0}\left(\chi_{\parallel}^{E} p_j p_n + \chi_{\perp}^{E}\left(\delta_{jn} - p_j p_n\right)\right) B_n$, where V is the particle volume, and μ_0 the permeability of free space.

The transient motion of the ellipsoidal particle can be tracked by following the change in **p** with respect to time. An explicit expression for the angular velocity ω_j can be solved at the torque balance. Then, using the equation $\frac{dp_i}{dt} = \varepsilon_{ijk}\omega_j p_k$, the time evolution of the orientation vector can be derived as

$$\frac{dp_i}{dt} = \frac{(\chi_{\perp}^{E} - \chi_{\parallel}^{E})V}{\mu_0 \zeta_r} B_n p_n (B_i - B_k p_k p_i), \tag{5.2}$$

where p_i is the i^{th} component of the particle's orientation vector. Assuming an infinitely thin oblate-ellipsoid, the rotational mobility is approximated as

$$\zeta_r = \frac{4}{3}\eta d^3, \tag{5.3}$$

where η is the fluid viscosity [73].

The external magnetic field is taken to be rotating in the (x_1,x_2)-plane, such that

$$B_i = B(\delta_{i1}\cos\omega t + \delta_{i2}\sin\omega t), \tag{5.4}$$

where B is the magnetic field strength, and ω the angular frequency of the rotating magnetic field.

Eqn. (5.2) can be non-dimensionalized by using the square of the aligning field strength such that a dimensionless time is defined as $\tau = AB^2t$, where

$$A = \frac{(\chi_\perp^E - \chi_\parallel^E)V}{\mu_0\zeta_r}, \tag{5.5}$$

containing the material and geometry parameters for the particle and the fluid viscosity. The dimensionless frequency is defined as $\xi = \omega/(AB^2)$. Rewriting time and frequency in dimensionless form, and converting the orientation vector to spherical coordinates, $\mathbf{p} = (\sin\theta\cos\phi, \sin\theta\sin\phi, \cos\theta)$, Eqn. (5.2) then becomes

$$\frac{d\phi}{d\tau} = \sin[2(\phi - \xi\tau)], \text{ and} \tag{5.6}$$

$$\frac{d\theta}{d\tau} = -\sin 2\theta\cos^2[\phi - \xi\tau]. \tag{5.7}$$

These two equations describe the alignment trajectory dependence on the dimensionless frequency, ξ. As ξ increases, the cos θ versus τ curves become smoother and overlap with each other (Fig. 5.2a). If the field rotation frequency is low, the magnetic torque, T^m, dominates over viscous drag torque, T^d, and the magnetic disk rotates synchronously with the field [69]. To force the easy plane of magnetic disk to align with the rotating field, the magnetic field must rotate at higher frequencies such that the disk rotation is hindered by fluid drag torque, T^d.

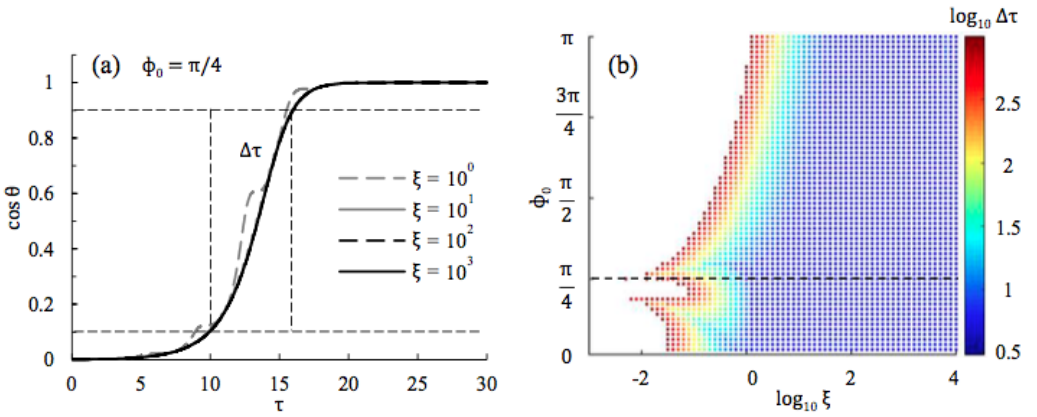

Fig. 5.2 (a) Modeled magnetic disk alignment (cos θ) versus τ at different ξ values with an initial azimuthal angle, $\phi_0 = \pi/4$. (b) Numerical simulation of Δτ for different dimensionless frequencies, ξ, and initial azimuthal orientations, ϕ_0 (τ step equals 10^{-3}).

Defining dimensionless alignment time, Δτ, as the time for cos θ to change from 0.1 to 0.9, Eqns. (5.6) and (5.7) can be solved using the finite-difference time-domain (FDTD) method. With a τ step of 10^{-3}, the dependence of Δτ on dimensionless frequency, ξ, and initial azimuthal angle, ϕ_0, is simulated numerically and shown in Fig. 5.2b. In the low ξ region ($\xi < 1$), the alignment process takes a considerably longer time with decreasing ξ; Δτ is highly sensitive to the initial azimuthal angle, ϕ_0. Whereas in the high ξ region ($\xi > 10$), Δτ does not depend on ϕ_0 or ξ (equivalently, the field angular frequency, ω), indicating high ξ to be ideal for achieving uniform magnetic alignment in many-particle systems. Eqns. (5.6) and (5.7) can also be solved analytically in the high ξ region to show

$$\tan\theta = \tan\theta_0 \exp\left[-\frac{\tau}{2}\right], \tag{5.8}$$

where θ_0 is the initial polar angle. This solution is in agreement with [66]. The dimensionless alignment time, Δτ, is then determined to be a constant that only depends on initial polar angle, θ_0, and final polar angle, θ,

$$\Delta\tau = 2\log\left[\frac{\tan[\cos^{-1}[0.1]]}{\tan[\cos^{-1}[0.9]]}\right]. \tag{5.9}$$

Converting $\Delta\tau$ back to dimensional alignment time using the relation $\Delta t = \Delta\tau/(AB^2)$, Δt is found to be proportional to the particle aspect ratio, κ, and fluid viscosity, η, and inversely proportional to the intrinsic susceptibility of the particle, χ, as well as the square of aligning field strength, B:

$$\Delta t \propto \frac{\kappa\eta}{\chi B^2}. \tag{5.10}$$

Note that Δt is independent of field rotation frequency and initial azimuthal orientation at the high ξ region.

5.3 Sample Preparation

Table 5.1 Properties of Ni-Fe microdisk and Metglas disk.

Magnetic Disk	Material	d (μm)	h (μm)	κ	$\chi_{\perp}^{E}$	$\chi_{\parallel}^{E}$
Ni-Fe microdisk	$Ni_{81}Fe_{19}$	5.0	0.15	33	18	1
Metglas disk	Metglas	360	29	12	12	1

Two types of magnetic disks are fabricated: Ni-Fe microdisks and Metglas disks (Table 5.1). Ni-Fe microdisks are made by photolithography and wet etching of sputtered Permalloy ($Ni_{81}Fe_{19}$) thin films. The Ni-Fe microdisks have a nominal dimension of 5 μm in diameter and 150 nm in thickness. They have an in-plane effective susceptibility ($\chi_{\perp}^{E}$) of 18 and an out-of-plane effective susceptibility ($\chi_{\parallel}^{E}$) of 1 from VSM measurement at 1 to 10 mT. Metglas disks, with a dimension of 360 μm in diameter and 29 μm in thickness, are fabricated by laser milling (ESI 5330 UV Laser uVIA Drill, Electro Scientific Industries, Inc., OR, USA) a Metglas cast ribbon (Metglas® 2826MB3, Metglas, Inc., SC, USA). The measured effective susceptibilities in-plane and out-of-plane are 12 and 1, respectively.

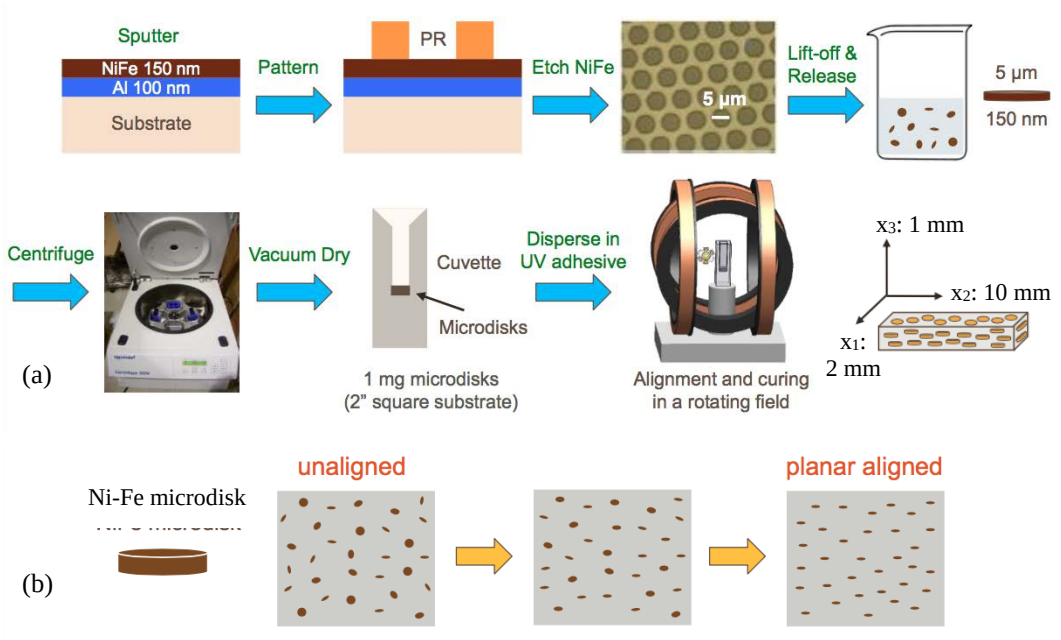

Fig. 5.3 (a) Ni-Fe microdisk fabrication process. (b) Schematic of Ni-Fe microdisk alignment in a composite.

To observe the dynamics of isolated magnetic disk rotation, a magnetic disk suspension with a low volume fraction (0.001 vol%) is prepared to minimize inter-particle dipole interactions. The magnetic disks are dispersed in silicone fluid standards (Brookfield Engineering Laboratories, Inc., MA, USA) with various viscosities (215 cP, 550 cP, and 5068 cP at room temperature, as measured by a DHR-3 Rheometer from TA Instruments, DE, USA). Compared with other fluid mediums like mineral oil, silicone fluid is chosen because its viscosity is less sensitive to temperature fluctuations.

The fabrication process of Ni-Fe microdisks composites is shown in Fig. 5.3a (see Appendix A for details). The microdisks are first dispersed in a UV-curable matrix (Loctite 3301 or Loctite 3106, Henkel Corporation, OH, USA) to make a suspension of 0.1 vol%. The UV-curable matrix is used here for fixing the particle orientations in place and measuring its effect on magnetic properties. An in-plane rotating magnetic field is applied to the suspension for various durations to obtain different degrees of alignment (Fig. 5.3b). Then, a UV light of 365 nm

wavelength (optimal wavelength for the UV-resins used) is applied for 1 min to pin the alignment state. The resulting composites have a rectangular shape with the easy planes of the disks aligned with the (x_1,x_2)-plane of the samples.

Table 5.2 Magnetic alignment parameters of Ni-Fe microdisk composites.

UV-Resin	Viscosity (cP)	Field Strength (mT)	Field Frequency (Hz)	Duration (s)
Loctite 3301	143	10	1.5	0, 1, 5, 10, 20, 40
Loctite 3106	5640	2	100	0, 20, 40, 60, 80

5.4 Characterization Techniques

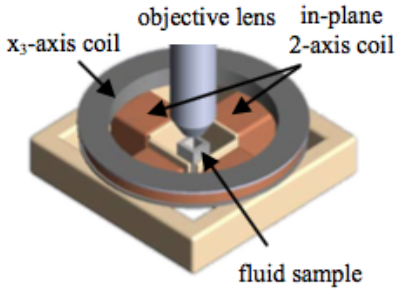

Fig. 5.4 Schematic of an optical microscope fitted with a three-axis electromagnet for observation of magnetic disk alignment dynamics [77].

To test the validity of Eqn. (5.10) in the medium and high ξ regions (that is for $\xi > 1$), dynamics of disk rotation in suspension in a rotating field is studied under an optical microscope fitted with a three-axis electromagnet (Fig. 5.4). The initial orientations of the disks are set by applying a constant magnetic field using the x_3-axis coil to align them perpendicular to the image plane. The disk appears edge-on in the microscope view. Subsequently, an in-plane rotating magnetic field from the two-axis coils is turned on to align the disk parallel to the image plane. The disk rotation under different fluid viscosities, aligning field strengths and rotation frequencies is captured by a microscope camera (see Appendix B for the detailed

settings). To verify the repeatability of measurements, five different Ni-Fe microdisks are imaged for each experimental condition.

The effect of aligning field duration on the microstructural and magnetic properties of the composite samples is studied by dark field optical microscopy, VSM, FMR spectrometer, and frequency dependence of permeability.

5.5 Results and Discussion

5.5.1 Effect of Aligning Field Strength

Ni-Fe microdisks are dispersed in a 550 cP viscosity silicone fluid (0.001 vol%). A 3 mT constant field generated by x_3-coil is first turned on to align the suspended Ni-Fe microdisks perpendicular. Then switch to a 5 mT, 50 Hz in-plane rotating field in the image plane to align the Ni-Fe microdisks parallel. The rotation of an isolated Ni-Fe microdisk is imaged by an optical microscope (40X magnification). The projected area of the disk on the image plane can be extracted from the snapshots of the disk, and used to plot the cos θ reponse over time, t (Fig. 5.5a). This result is compared with the simulated curve from the model, and good agreement is found between them.

Repeat the experiment with aligning field strength varied from 3 to 7 mT (Fig. 5.5b). The alignment time, Δt, which is the time for cos θ to change from 0.1 to 0.9, is extracted and plotted over inverse square of aligning field strength, $1/B^2$ (Fig. 5.5c). The alignment time, Δt, is found to be decreasing with stronger aligning field strength. The reproducibility of the measurement is tested by imaging five different Ni-Fe microdisks for each field. Good reproducibility is found, as the error bars in Fig. 5.5c are small. This data establishes that the alignment time of magnetic disks scales linearly with the inverse square of aligning field strength ($\Delta t \propto 1/B^2$) as predicted by Eqn. (5.10).

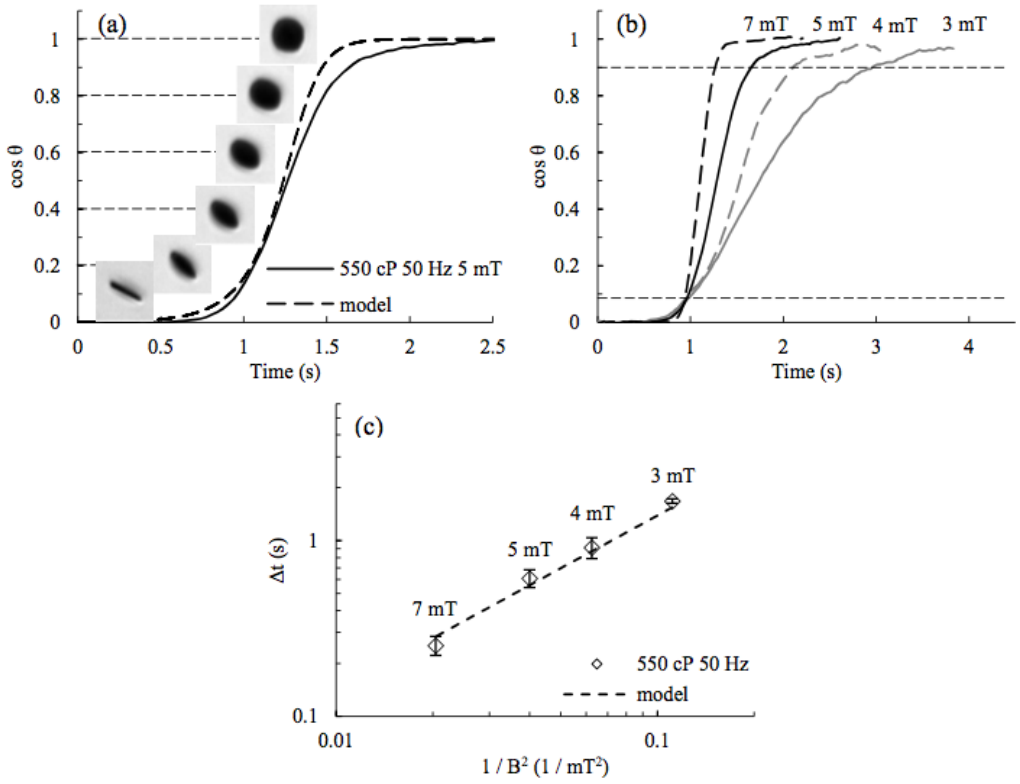

Fig. 5.5 (a) A Ni-Fe microdisk rotates from perpendicular to parrallel in a 550 cP fluid, under a 5 mT, 50 Hz in-plane rotating field. (b) Dependence of cos θ on field strength, B. (c) Dependence of Δt on field strength, B [77].

5.5.2 Effect of Fluid Viscosity

Ni-Fe microdisk alignment in fluids with different viscosities (215 cP, 550 cP, and 5068 cP) is experimented, and the effect of fluid viscosity is summarized in Fig. 5.6. Comparison between different viscosities confirms that the alignment time scales proportionally with the fluid viscosity ($\Delta t \propto \eta$).

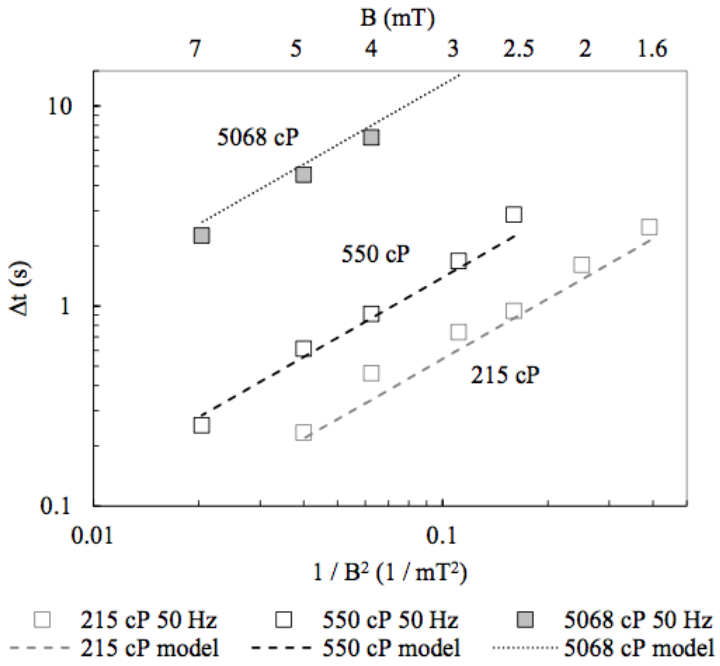

Fig. 5.6 Alignment time, Δt, of Ni-Fe microdisks is measured with varying fluid viscosities, η.

5.5.3 Effect of Field Rotation Frequency

Shown in Fig. 5.7 are the alignment times, Δt, measured with varying field rotation frequencies. As predicted by the model, no dependence of field rotation frequency is found in alignment time, Δt; alignment times with different field rotation frequencies overlap with each other. The deviation of the measured Δt from the model is examined as a function of field rotation frequency, and no dependence is found. In summary, the measured alignment times in Ni-Fe microdisks follow the $\Delta t \propto \eta/B^2$ relationship in Eqn. (5.10).

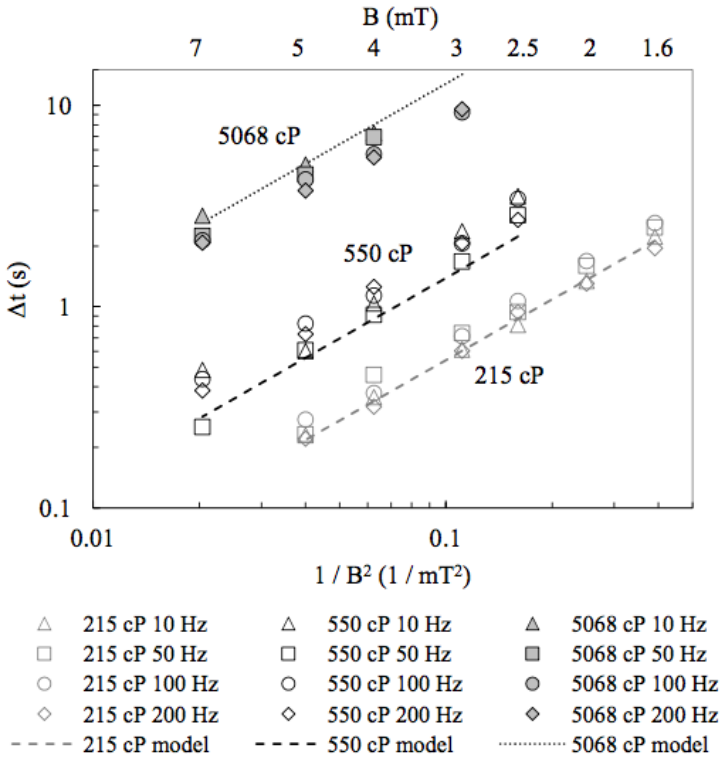

Fig. 5.7 Alignment time, Δt, of Ni-Fe microdisks is measured with varying field rotation frequencies [77].

5.5.4 Effect of Aspect Ratio and Susceptibility

Using a 10X magnification objetive lens, a single Metglas disk suspended in a 5068 cP silicone fluid is imaged to test the model for larger particle size (360 μm in diameter, compared to 5 μm for Ni-Fe microdisks) and smaller susceptibility ($\chi_{\perp}^{E}$ = 12, compared to 18 for Ni-Fe microdisks). As particle size increases and the sedimentation Péclet number, Pe_s, becomes $\mathcal{O}(10)$, gravitational force needs to be considered in the model as it starts to affect particle hydrodynamics. The model, however, still provides a reasonable estimate of alignment time, Δt, as seen from Fig. 5.8.

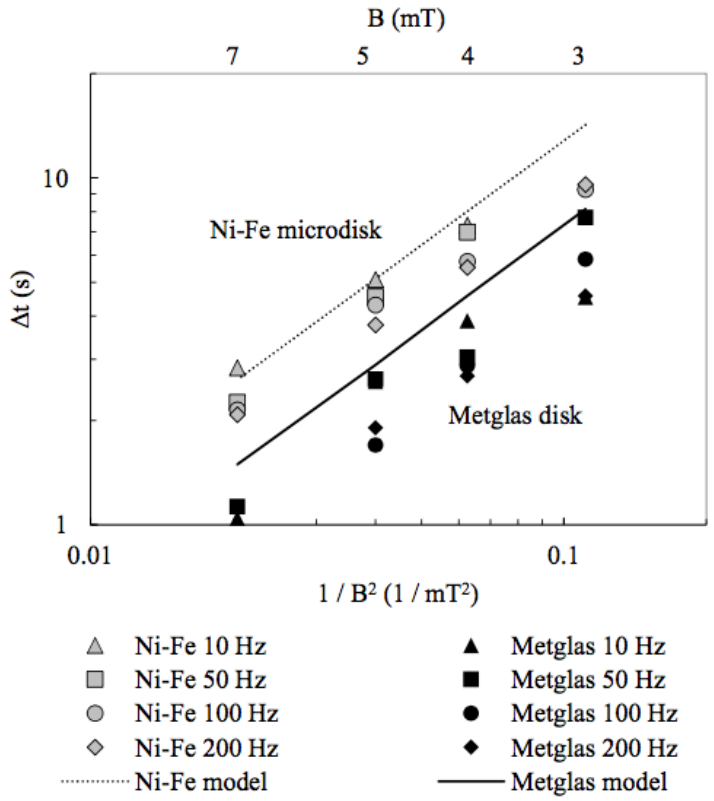

Fig. 5.8 Alignment times, Δt, of Ni-Fe microdisks and Metglas disks are imaged in a 5068 cP fluid and compared.

5.5.5 Comparison with Model

In Fig. 5.9, the FDTD numerical simulation results at $\phi_0 = \pi/4$ (dashed line across Fig. 5.2b) as well as the analytical results calculated from Eqn. (5.8) are plotted. Both modeled results show a flat $\Delta\tau$ versus ξ for $\xi > 1$. To test the validity of the model, the measured results are converted to dimensionless alignment time, $\Delta\tau$, versus dimensionless frequency, ξ, and plotted over the modeled results. The dimensionless alignment time, $\Delta\tau$, of Ni-Fe microdisks and Metglas disks also show a flat response versus ξ. The deviation observed between measurement and model is mainly attributed to the uncertainty in disk shape (that is, any deviation from perfectly round shape), which can greatly affect the rotation dynamics. The deviation can also be caused by temperature dependent fluctuations in viscosity.

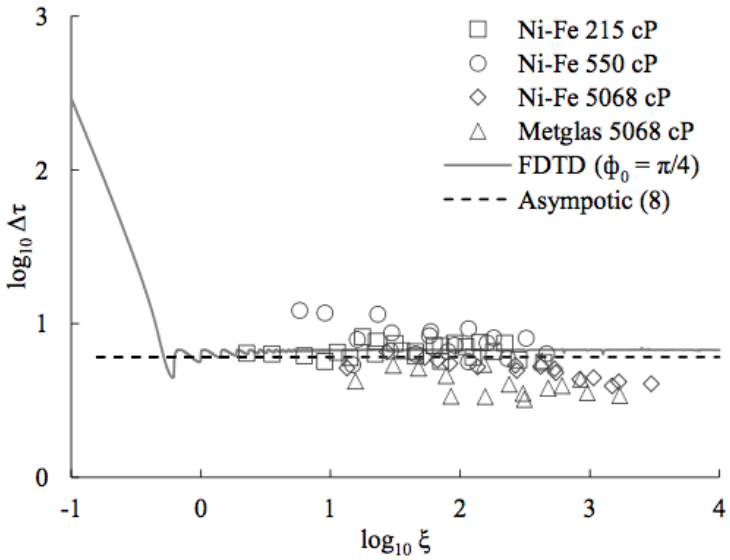

Fig. 5.9 Validity of analytical and FDTD numerical simulation results for $\xi > 1$ are tested by comparing with measured dimensionless alignment time ($\Delta\tau$) versus ξ responses.

5.5.6 Effect of Volume Fraction

To study the multiple-particle rotation, the volume fraction of Ni-Fe microdisks suspended in a 5068 cP silicone fluid is increase to 0.1 vol%. Rather than zooming in and capturing the rotation of an isolated Ni-Fe microdisk, the microdisk alignment dynamics in this multiple-particle system are studied by measuring the average brightness of the suspension under transmitted light in an optical microscope. A 10X magnification objective lens is used to image a larger sample area. The average brightness of the imaged sample area starts with maximum brightness because the microdisks are aligned perpendicular to the image plane. As the aligning field is turned on and applied over time, the microdisks rotate toward in-plane orientation, covering larger and larger area in the image plane and decreasing the brightness. When all microdisks finally reach the in-plane orientation, the brightness drops to a minimum. The change of average brightness over time, showing a response similar to isolated microdisk rotation shown in Fig. 5.5a, represents averged cos θ versus t response of multiple particles. Therefore,

alignment times can be extracted in a similar way (shown in Fig. 5.10). Alignment times of Ni-Fe microdisks suspension with 0.001 vol% (isolated particle system) and 0.1 vol% (multiple-particle system) fall in the same linear response when plotted versus $1/B^2$. The inter-particle dipole interactions do not have a significant effect on the rotational behavior of Ni-Fe microdisks in a 0.1 vol% suspension.

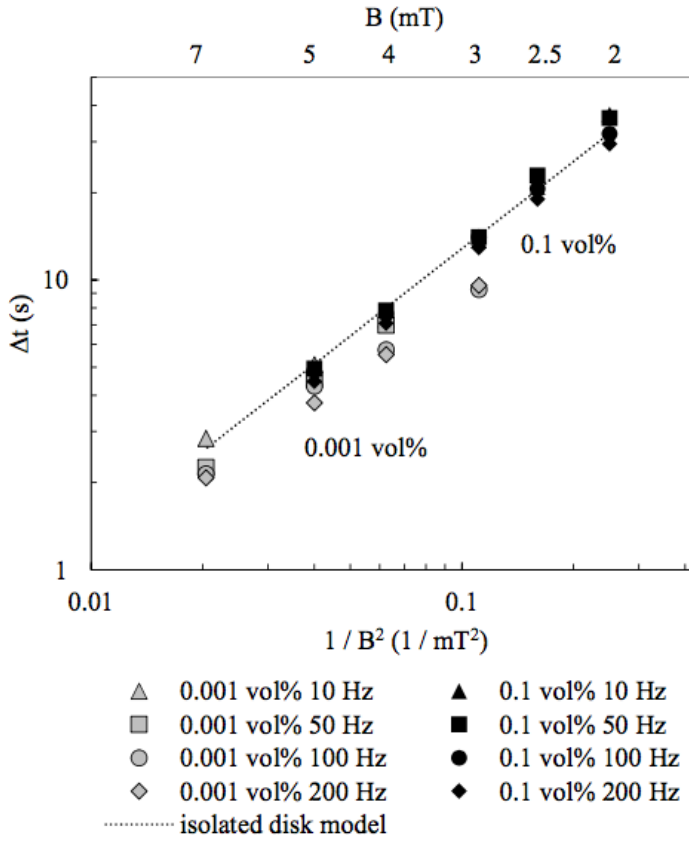

Fig. 5.10 Comparison of alignment time in 0.001 vol% and 0.1 vol% samples of Ni-Fe microdisks suspended in a 5068 cP silicone fluid [77].

5.5.7 Effect of Particle Chaining

The inter-particle interaction, however, has a significant effect on the transverse motion of Ni-Fe microdisks in a multiple-particle system [74-77]. If continue to apply the in-plane rotating field to already aligned Ni-Fe microdisks,

the microdisks will start moving toward each other due to the attraction between neighboring magnetized particles, and eventually form particle chaining layers. Such inhomogeneous distribtuion of microdisks is undesirable for high frequency applications, as it reduces the electrical resistance, and hence, increases eddy current loss in the material.

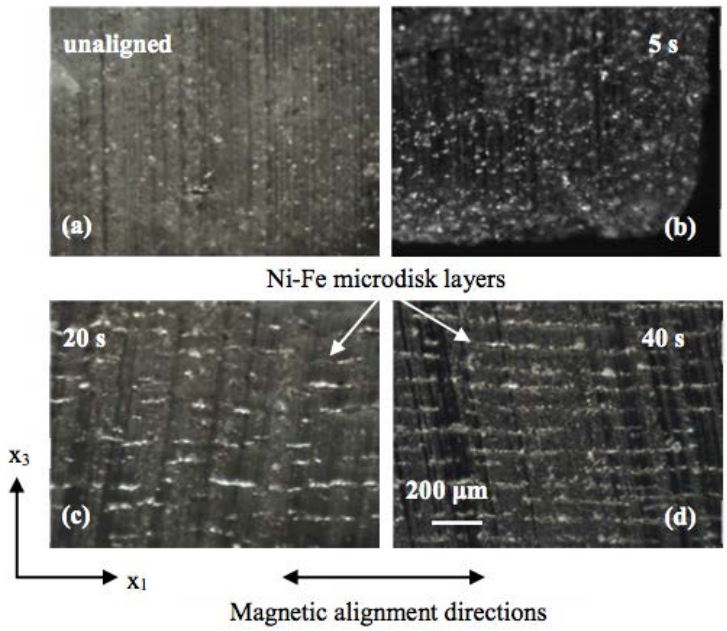

Fig. 5.11 Cross sections of Ni-Fe microdisk composites (0.1 vol%) in the (x_1,x_3)-plane imaged by dark field optical microscopy. The constituent Ni-Fe microdisks are aligned under a 10 mT, 1.5 Hz rotating field for (a) 0 s (unaligned), (b) 5 s, (c) 20 s, (d) 40 s in the composites [77].

To study the forming of microdisk layers and its effect on Ni-Fe microdisk microstructural and magnetic properties, Ni-Fe microdisks with random orientations are suspended in a 143 cP viscosity UV-curable matrix (Loctite 3301, Henkel Corporation, OH, USA), aligned in a 10 mT, 1.5 Hz rotating field in (x_1,x_2)-plane from 0 to 40 s, and finally cured in a UV light.

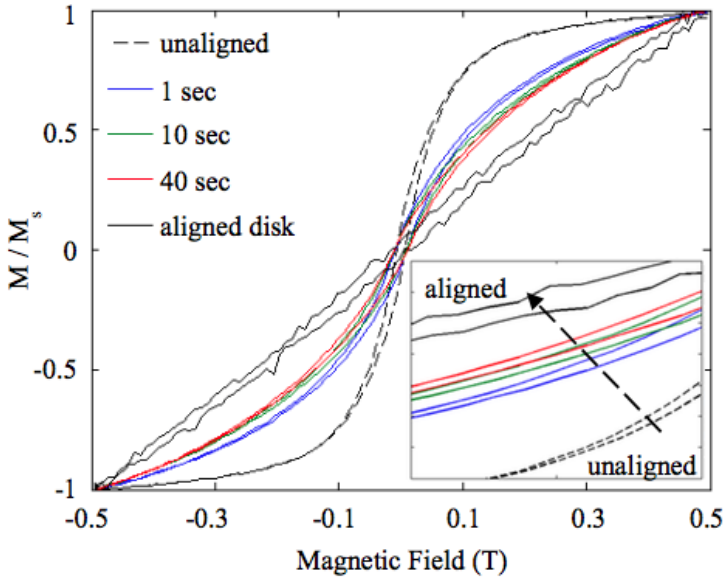

Fig. 5.12 Normalized hysteresis curves of Ni-Fe microdisk composites (0.1 vol%) measured in the x_3-direction. The constituent Ni-Fe microdisks are aligned under a 10 mT, 1.5 Hz rotating field from 0 (unaligned) to 40 s. Ni-Fe microdisks unreleased from substrate is also measured in the x_3-direction and plotted as "aligned disk."

The cross sections of these composites, both in (x_2,x_3)-plane and (x_1,x_3)-plane of the rectaugular samples, are examined by dark field optical microscopy. The images taken in (x_2,x_3)-plane are identical to those of (x_1,x_3)-plane, and therefore not included. Ni-Fe microdisks in the unaligned sample are uniformly distributed and randomly oriented. As the aligning field duration increases, inter-particle interactions begin to affect microdisk distribution. In addition to being oriented in-plane, the microdisks also start chaining and forming layers under the rotating field. With increasing aligning field duration, the chaining layers 1) grow into larger areas in (x_1,x_2)-plane, and 2) become more uniformly spaced in x_3-direction.

The effect of particle chaining on hysteresis curves is measured by VSM and shown in Fig. 5.12. Ni-Fe microdisks unreleased from substrate, which has perfect particle alignment, is also measured ("aligned disk" in Fig. 5.12). As the aligning field duration increases from 0 (unaligned) to 40 s, the hysteresis curves

gradually migrate from the response of randomly oriented (unaligned) to the response of perfectly aligned (microdisks unreleaseed). Beyond 40 s, the hysteresis curves overlap with the response of 40 s aligned sample.

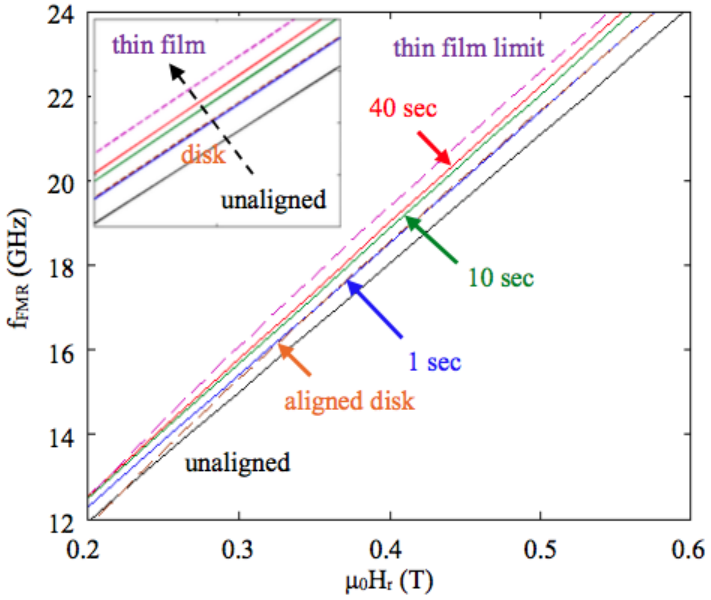

Fig. 5.13 Ferromagnetic resonance frequency, f_{FMR}, dependence of resonance field, H_r, in Ni-Fe microdisk composites (0.1 vol%) measured in the (x_1,x_2)-plane (*dc* field in x_1-direction, microwave field in x_2-direction). The constituent Ni-Fe microdisks are aligned under a 10 mT, 1.5 Hz rotating field from 0 (unaligned) to 40 s. Also plotted are FMR responses of a fullly aligned Ni-Fe microdisk and a Ni-Fe thin film calculated from Kittel's equation.

This result is further supported by the ferromagnetic resonance data (Fig. 5.13). Planar anisotropy in the composite is increased as the alignment time increases, which shifts the resonance frequency, f_{FMR}, higher. Also plotted are FMR responses of an aligned Ni-Fe microdisk and a Ni-Fe thin film calculated from the Kittel's equation with the resonance field, H_r, applied in the easy plane:

$$f_{FMR} = \frac{\gamma}{2\pi}\,\mu_0\sqrt{H_r(H_r + (N_{out} - N_{in})M_s)}\,, \qquad (5.11)$$

where N_{in} is the demagnetizing factor in the disk plane, and N_{out} the out-of-plane demagnetizing factor. For an isolated Ni-Fe microdisk, N_{out} and N_{in} are calculated

[16-17] to be 0.92, and 0.04, respectively; while for Ni-Fe thin film, $N_{out} = 1$, $N_{in} = 0$. As shown in Fig. 5.13, the response of 1 s aligned overlaps with the aligned disk response, which is in agreement with the predicted very fast alignment process. As the aligning field duration increases, the FMR response of Ni-Fe microdisk composite approaches the Ni-Fe thin film response. This shift in ferromagnetic resonance frequency comes from an increase in the anisotropy of microdisk chaining layers, indicating the microdisk layers are expanding due to particle chaining.

In summary, the degree of particle chaining and microdisk layer formation is aligning field duration dependent; to avoid the particle chaining, the aligning field needs to be turned off as soon as the alignment process finishes. Additionally, using a UV-curable matrix with a yield stress may prevent chaining, as the matrix is reported to arrest magnetic particle chaining [78].

5.5.8 Effect of Aligning Field Duration

To achieve precise control of magnetic particle alignment and minimize chaining, high fluid viscosity (~5000 cP), high aligning field frequency (~100 Hz), and low aligning field strength (~2 mT) are recommended to slow the particle transverse movement. Following this insight, Ni-Fe microdisks are dispersed in a high viscosity UV-curable matrix (5640 cP visocisty, Loctite 3106, Henkel Corporation, OH, USA), and aligned in a rotating field of 2 mT, 100 Hz in (x_1,x_2)-plane. The resulting Ni-Fe microdisk composites have a volume fraction of 0.1 vol%. The alignment time in this condition is estimated to be about 60 s from the alignment behavior of Ni-Fe microdisks in a 5068 cP silicone fluid (Fig. 5.10). Dissimlar to the random orientations in particle chaining experiments, the microdisks start perpendicularly aligned by a constant magnetic field. To obtain different degrees of planar alignment, an in-plane rotating field in (x_1,x_2)-plane is applied from 0 to 80 s prior to UV-curing.

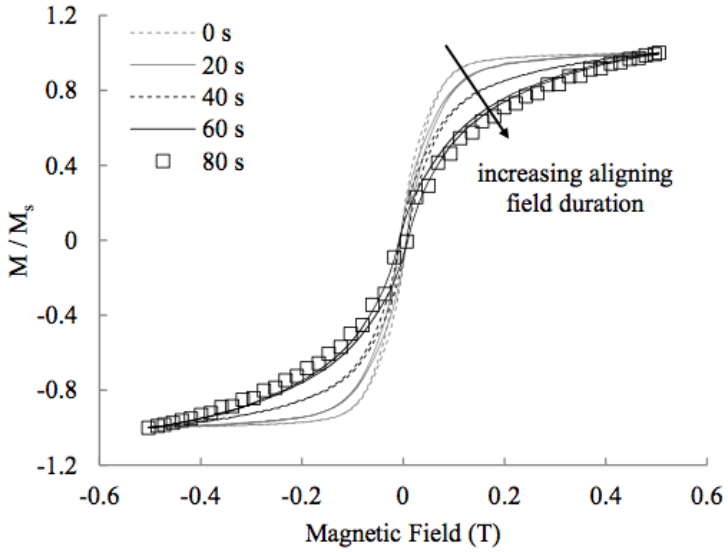

Fig. 5.14 Normalized hysteresis curves measured in x_3-direction (induced hard axis) for magnetic composites with 0.1 vol% Ni-Fe microdisks. The constituent microdisks are aligned under various durations by a 2 mT, 100 Hz in-plane rotating field, and cured in a 5640 cP UV-curable matrix [77].

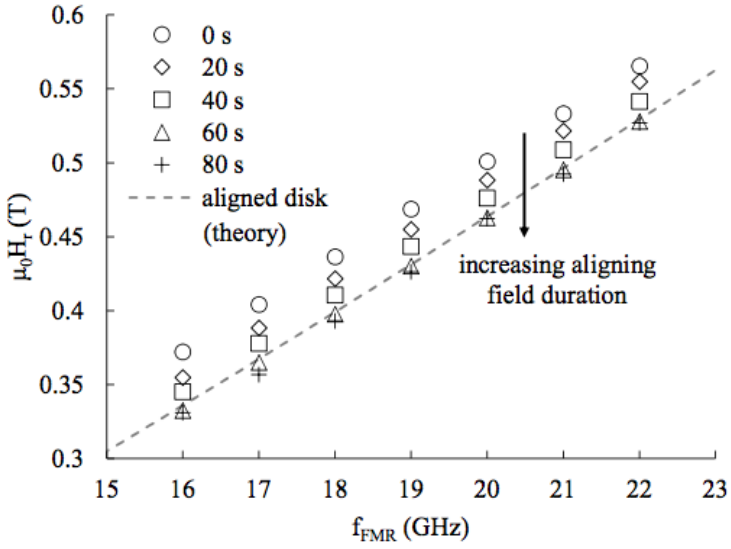

Fig. 5.15 Ferromagnetic resonance frequency measured in-plane for magnetic composites with 0.1 vol% Ni-Fe microdisks. The constituent microdisks are aligned under various durations by a a 2 mT, 100 Hz in-plane rotating field, and cured in a 5640 cP UV-curable matrix [77].

Shown in Fig. 5.14 are the normalized hysteresis curves of Ni-Fe microdisk composites measured in x_3-direction (induced hard aixs) with varying aligning field durations. A gradual transition of hysteresis curves from an easy axis response to a hard axis response is observed with increasing aligning field duration up to 60 s. This result reveals that the constituent microdisks are gradually oriented to be parallel with (x_1,x_2)-plane, which raises the planar anisotropy of Ni-Fe microdisk composites. No further change is observed with an aligning field duration of 80 s.

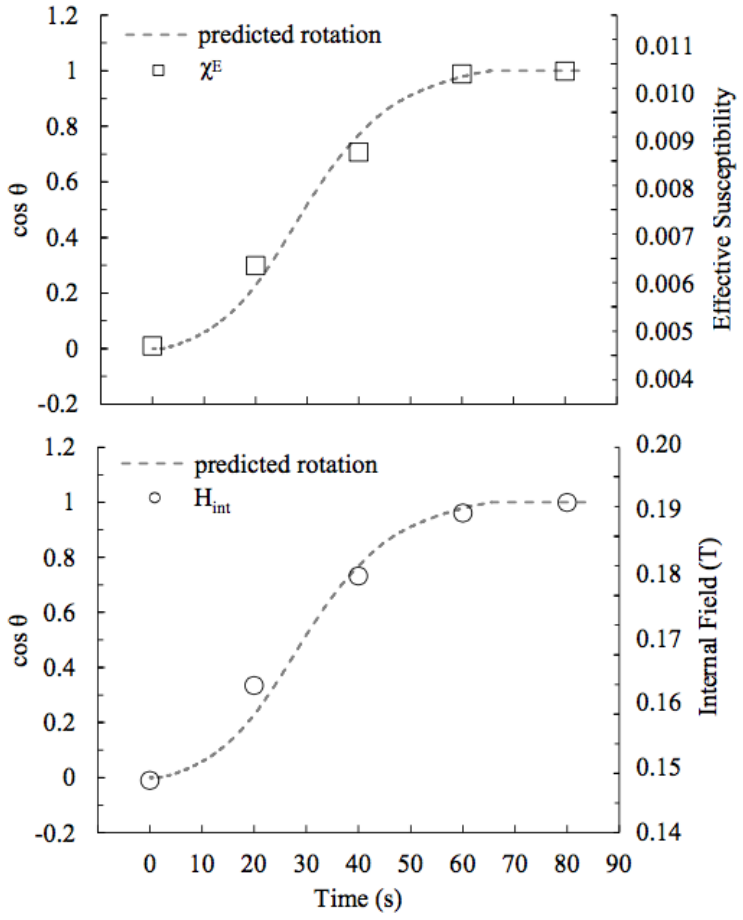

Fig. 5.16 Dependence of in-plane effective susceptibility at 1 to 10 mT and magnetic anisotropy of Ni-Fe microdisk composites on aligning field duration of a 2 mT, 100 Hz in-plane rotating field [77].

The effect of aligning field duration on planar anisotropy can be also observed in the ferromagnetic resonance of composites (Fig. 5.15). The ferromagnetic resonance frequency, f_{FMR}, is measured in (x_1,x_2)-plane, and a shift to higher frequencies is observed as the rotating field is applied over a longer duration, indicating an increase in planar anisotropy. Using Kittel's equation (Eqn. 5.11), ferromagnetic resonance response of a fully aligned Ni-Fe micordisk is calculated and plotted in Fig. 5.15 as a dotted line. The theoretical response overlaps with the measured result of 60 s aligned, confirming the alignment time for Ni-Fe microdisks is indeed around 60 s.

The degree of alignment in microdisks determines the composite's planar anisotropy, which is shown in Fig. 5.16 by plotting the change of composite's magnetic properties on top of microdisk rotation over time (predicted from Fig. 5.10). The effective susceptibility, χ^E, at 1 to 10 mT in (x_1,x_2)-plane (measurd by VSM) as well as the planar anisotropy field, H_{int}, closely tracks the predicted microdisk rotation behavior. This result demonstrates that the microdisks gradually rotate to the rotating field plane ((x_1,x_2)-plane) over a time span of 60 s. By varying the aligning field duration within 60 s, the planar anisotropy of Ni-Fe microdisk composites can be precisely tuned. Beyond 60 s, aligned microdisks start slowly moving toward each other to form chaining layers.

The Ni-Fe microdisk alignment also increases the high frequency permeability of the composites. To compare the permeability between a perpendicularly aligned (0 s in-plane rotating field applied) and a parallel aligned Ni-Fe microdisk composite (aligned in a 2 mT, 100 Hz in-plane rotating field for 60 s), composite samples are molded into a toroid shape with 8 mm outer diameter, 5 mm inner diameter, and 1 mm thickness. The permeability is measured by an impedance analyzer from 1 to 3 GHz (Fig. 5.17). With the easy planes of constituent Ni-Fe microdisks aligned parallel by the rotating field, the 60 s aligned composite exhibits improved high frequency permeability compared with the perpendicularly aligned (0 s) sample. However, due to the low volume fraction (0.1 vol%) of the

composites, the real part of permeability is close to 1. Combined, the data in Figs. 5.15 and 5.17 demonstrate that Snoek's limit can be overcome by the induced planar anisotropy in Ni-Fe microdisk composites, improving both permeability and ferromagnetic resonance frequency.

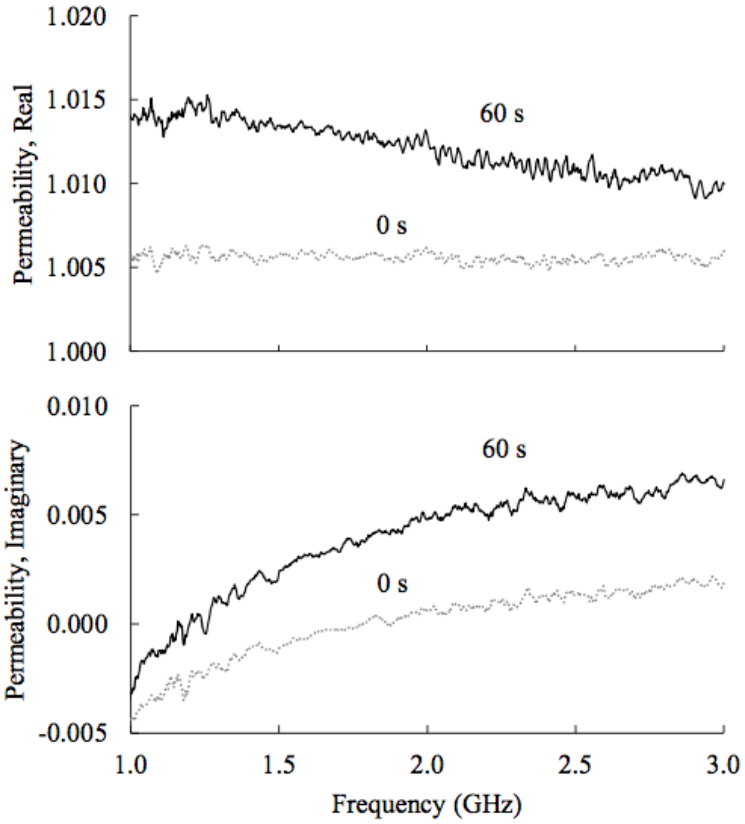

Fig. 5.17 Comparison of permeability between a perpendicularly aligned (0 s in-plane rotating field applied) and a parallel aligned Ni-Fe microdisk composite (aligned in a 2 mT, 100 Hz in-plane rotating field for 60 s) [77].

5.6 Summary

The alignment dynamics of magnetic disks in an in-plane rotating field is investigated by a systemic experimental and theoretical study. A model is developed to describe the dynamics of magnetic disks in a Newtonian fluid under an in-plane rotating field. Planar alignment of the disks with high ξ (high fluid

viscosity, high field rotation frequency, low aligning field strength), in which the particles with different initial azimuthal orientations can be uniformly aligned, is recommended. The model is tested experimentally at $\xi > 1$ with different viscosities, aligning field strengths and frequencies, and disk sizes. Good agreement is found between the model and measured results. To optimize this planar alignment process under high ξ conditions, a trade-off between faster processing time (high aligning field strength, low viscosity) and material homogeneity (low aligning field strength for minimizing particle chaining, high viscosity for slowing sedimentation) must be considered. Moreover, by varying aligning field duration, the orientations of magnetic disks, and hence, the planar anisotropy of the magnetic composites can be fine-tuned without chaining of particles.

A comparison between this work and previous studies [48-52] on planar alignment in magnetic composites is shown in Table 5.3. In previous studies, the particles are made by ball milling for achieving high volume fractions. However, the resulting magnetic flakes have very wide shape and size distributions compared with the cleanroom-made microdisks, making the rotation dynamics hard to model. The composite fabrication process in previous studies involves dispersing the flakes in paraffin wax or epoxy, and rotating the suspension in a constant magnetic field around 1 T until solidification. This work offers a composite fabrication and alignment process with better control: 1) the curing of the UV-resin is on-demand and the aligning field duration is controlled to fine-tune the planar anisotropy and avoid particle chaining; 2) rather than rotating the suspension, the aligning field is rotated, which allows a higher frequency and a more uniform alignment of multiple-particle systems; 3) a much smaller aligning field strength is needed according to the model, making the aligning field setup low cost and easy to implement.

Table 5.3 Comparison between previous studies on planar alignment and this work.

	Previous Studies [48-52]	**This Work**
Particle Shape	flakes (wide distribution)	disks (narrow distribution)
Matrix Curing	slow solidification	on-demand curing
Field Strength	~ 1 T (high power process)	< 10 mT
Field Frequency	~ 1 Hz (rotating sample)	~ 100 Hz (rotating field)
Field Duration	applied until solidification	timed according to the model

In conclusion, this work not only demonstrates the possibility of precisely tuning planar anisotropy in composite materials by applying various durations of in-plane alignment to the constituent magnetic disks, which can be a useful technique to customize the composites for high frequency applications, but it also provides the crucial theoretical understanding and experimental evidence for optimization of this planar alignment process.

CHAPTER 6. MAGNETIC INKJET PRINTING

6.1 Introduction to 3D Magnetic Printing

3D printing processes as a rapid, versatile, and cost-effective production technology has great potential in designing and prototyping magnetic components [79-82]. Unlike conventional thin-film deposition and lithography, the proposed 3D magnetic inkjet printing technique allows for arbitrary magnetic alignment [83] and curing of "magnetic ink" [84], which is a dispersion of magnetic nanoparticles in a UV-curable resin (Fig. 6.1). The alignment of magnetic particles improves the high frequency magnetic properties, while the curing capability enables layer-by-layer printing to build up 3D structures.

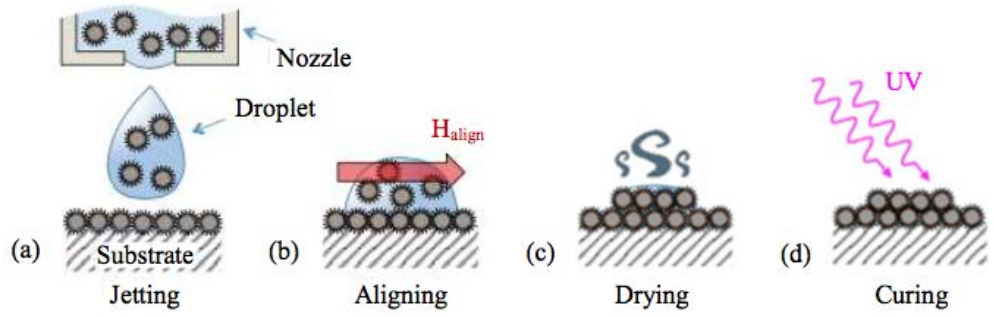

Fig. 6.1 Schematic for 3D printing magnetic structures with custom anisotropy [84]. (a) A magnetic ink drop is jetted onto the substrate. (b) A magnetic field is then applied to align the nanoparticles. (c) The thinner component of magnetic ink, which is added to reduce viscosity, is evaporated. (d) Apply a UV light to cure the UV-curable resin for pinning the particle alignment state. The process is repeated to obtain the 3D magnetic structure of desired shape, dimension, and anisotropy.

In this work, an inkjet printing technique with magnetic alignment and UV-curing capability is developed. The magnetic alignment is explored by printing magnetic films with and without particle alignment, and comparing their magnetic properties by VSM, FMR, and high frequency permeability measurements. The UV-curing capability is demonstrated by printing and curing samples with varying numbers of layers.

6.2 Experimental Setup and Sample Preparation

6.2.1 Hewlett-Packard Thermal Inkjet Pipette System (TIPS)

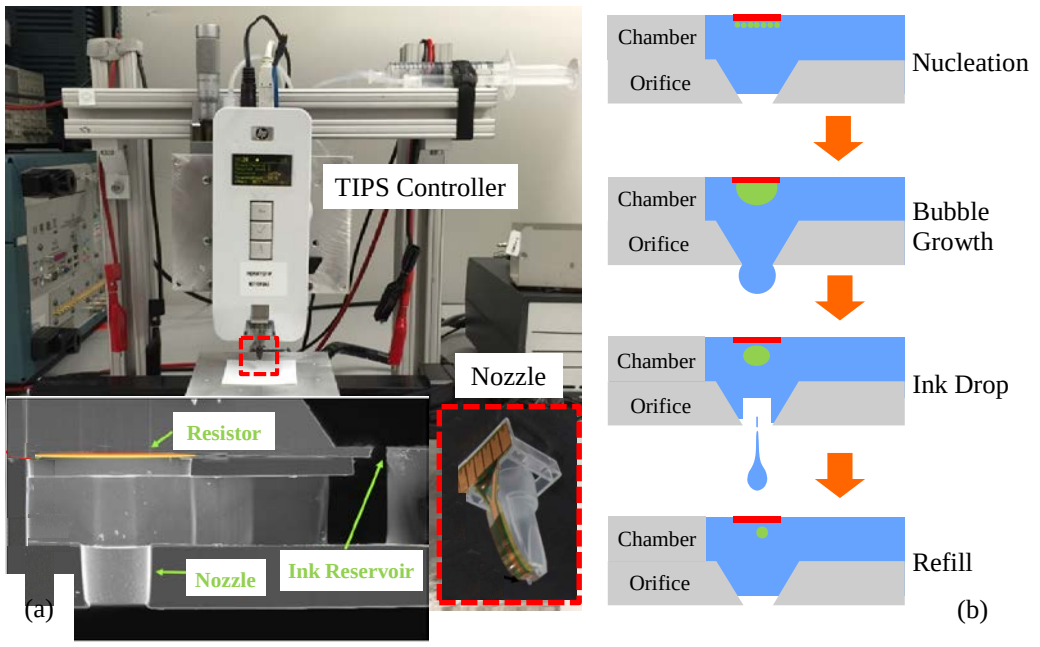

Fig. 6.2 (a) TIPS controller with nozzles installed (photos courtesy of Hewlett-Packard Company). (b) Schematic of thermal inkjet process.

Thermal Inkjet Pipette System (TIPS), designed by Hewlett-Packard Company (Fig. 6.2a), is used for printing the magnetic ink. The TIPS controller can be installed with refillable, disposable printheads, and programmed using a universal serial bus (USB) interface for computer control of droplet ejection parameters, drop quantity, number of nozzles, and jetting energy. The size of the droplet can be modified by choosing printheads with various orifice diameters. The printhead used in this experiment has an orifice diameter of 60 μm.

The thermal inkjet printing process is shown in (Fig. 6.2b). 1) The resistor inside the orifice chamber is heated up by an electrical pulse. The ink close to the resistor is consequently heated, and forms small vapor bubbles (bubble nucleation). 2) Nucleated bubbles expand and force a small volume of ink through the orifice

(bubble growth). 3) The ink is ejected, and the droplet breaks free from the orifice (ink drop stage). 4) Ink from the reservoir refills the orifice for jetting of the next drop (ink refill).

6.2.2 Magnetic Printing Setup

The TIPS controller is fixed above a stepper motor XY-stage (Fig. 6.3a). Commercial photo paper, which can quickly absorb the ink solvent, is taped on the XY-stage and used as the substrate. The printhead to substrate distance is 4 mm. A two-axis electromagnet is integrated on the TIPS controller just below the printhead to apply a magnetic field with arbitrary strength and direction for precise alignment of the constituent nanoparticles in each droplet (Fig. 6.3b). The nozzle is magnetically shielded from the aligning field by Mu-metal (a high permeability Ni-Fe alloy) to keep it from clogging (Fig. 6.3c). Four optic cables are used to guide UV light (400 nm wavelength) onto the drop on the substrate, for curing the ink and fixing its alignment state. During printing, the magnetic ink droplet is jetted from the nozzle, aligned by the magnetic field, and cured by a UV light on the substrate, while the substrate is moved by the XY-stage under the nozzle. The whole magnetic printing process is controlled and automated by a LabVIEW program (see Appendix D for details).

Two magnetic inks with different compositions are used for printing: pure MICR ink and MICR - Objet ink. MICR ink is a high solid content (40 vol%), low viscosity (~6 cP) aqueous suspension of ferromagnetic Co-based nanoparticles (40 nm mean particle size). To make the magnetic ink UV-curable, dried MICR ink (dried at 80 °C) is mixed with a UV-curable resin (Objet RGD720, Stratasys, Ltd., MN, USA). The Objet UV-resin is thinned with Ethanol (1 part Objet : 4 part Ethanol) to lower its viscosity for ease of jetting from the nozzle. The resulted “MICR - Objet” ink has a 0.5 vol% of Co-based nanoparticles, and a low viscosity of ~2 cP.

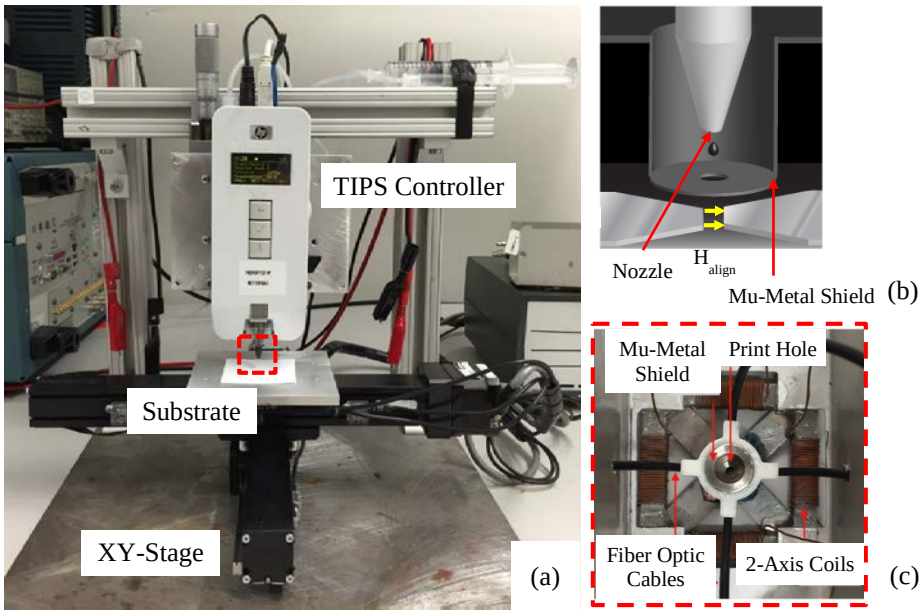

Fig. 6.3 (a) Magnetic inkjet printer setup showing the TIPS controller. (b) Schematic of magnetic alignment setup. (c) Top view photo of magnetic alignment setup and UV optic fibers.

6.2.3 Printed Magnetic Sample with Alignment

Two types of samples are printed using MICR ink to study the effect of magnetic alignment: square-shaped and ring-shaped samples (Fig. 6.4). The square-shaped samples have a dimension of 5 mm by 5 mm, with a 10 mT aligning field applied in x-direction. The ring-shaped samples have an inner diameter of 4 mm and an outer diameter of 7 mm, with a 10 mT aligning field applied in radial direction. Both types of samples are printed with and without the aligning field. These samples are printed with one layer and air-dried.

To make 3D magnetic samples, 5 mm by 5 mm square-shaped samples with 1, 2, and 3 layers are printed using the UV-curable “MICR - Objet” ink. No magnetic aligning field is applied during printing. Each printed layer is cured by exposure to a 400 nm UV light.

A summary of printed magnetic samples can be found in Table 6.1.

Fig. 6.4 Photos and schematics of (a) a x-direction aligned square-shaped sample and (b) a radial direction aligned ring-shaped sample. (Reprinted with permission from Song *et al.* [83].)

Table 6.1 A list of inkjet printed magnetic samples.

#	Composition	Shape	Layers	Alignment	Curing
A1	MICR ink (40 vol%)	square	1	No alignment	Air-dried
A2	MICR ink (40 vol%)	square	1	10 mT in x-direction	Air-dried
B1	MICR ink (40 vol%)	ring	1	No alignment	Air-dried
B2	MICR ink (40 vol%)	ring	1	10 mT in radial direction	Air-dried
C1	MICR - Objet (0.5 vol%)	square	1	No alignment	UV-curing
C2	MICR - Objet(0.5 vol%)	square	2	No alignment	UV-curing
C3	MICR - Objet (0.5 vol%)	square	3	No alignment	UV-curing

6.3 Characterization Techniques

The effect of magnetic alignment is studied by VSM, FMR, and high frequency permeability measurements. For square-shaped samples, magnetic properties in x- and y-directions are compared by VSM and FMR measurements. For ring-shaped samples, the high frequency permeability is first measured by the impedance analyzer. The ring-shaped samples are then cut into slices along radial direction and measured by VSM and FMR in both radial and circumferential directions. The effect of number of printing layers is examined on C1, C2 and C3 (MICR - Objet) samples by VSM measurements.

6.4 Results and Discussion

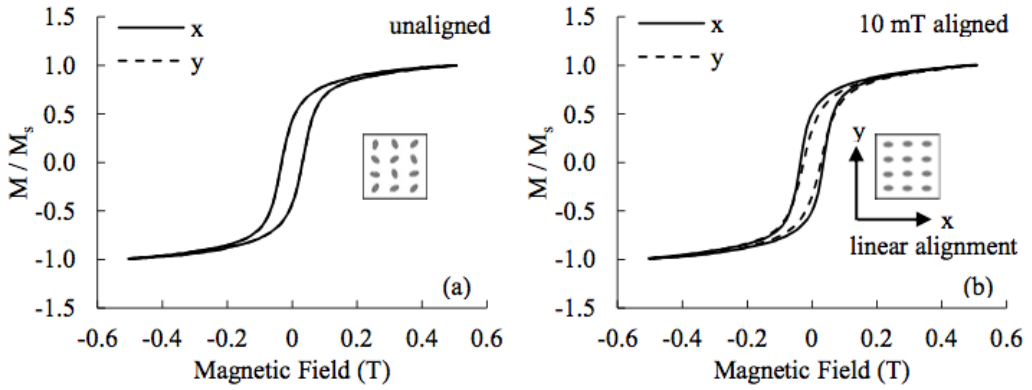

Fig. 6.5 Normalized hysteresis curves measured in both x- and y-directions for (a) an unaligned square-shaped sample and (b) a 10 mT, x-direction aligned square-shaped sample. (Reprinted with permission from Song *et al.* [83].)

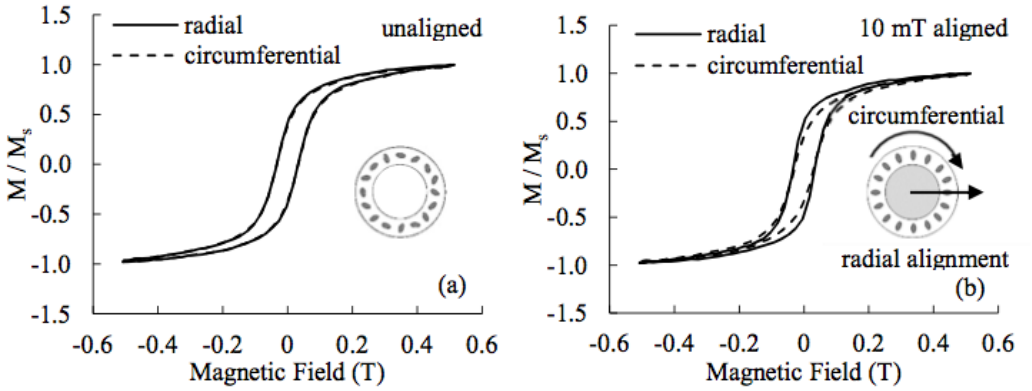

Fig. 6.6 Normalized hysteresis curves measured in both radial and circumferential directions for (a) an unaligned ring-shaped sample and (b) a 10 mT, radial direction aligned ring-shaped sample. (Reprinted with permission from Song *et al.* [83].)

The effect of magnetic alignment on printed samples is first investigated by VSM (Fig. 6.5 and 6.6). The unaligned samples exhibit an isotropic magnetic response for both square-shaped and ring-shaped samples: after normalization, the hysteresis curves for different directions overlap with each other and show no magnetic anisotropy. In contrast, 10 mT aligned samples exhibit anisotropy in the alignment direction: compared with unaligned samples, the hysteresis curves show

higher hysteresis loss in the alignment direction, and lower loss in the direction perpendicular. The repeabability of this result is confirmed by VSM measurement of three aligned ring-shaped samples.

This induced anisotropy reveals that the aligning field, to some extent, physically rotates the magnetic nanoparticles, and orients their easy axes in the ink drop. This effect of particle alignment is further corroborated by ferromagnetic resonance data (Fig. 6.7). From the vertical shift in FMR frequency, f_{FMR}, between the unaligned and the 10 mT aligned sample, a 0.028 T increase in anisotropy is observed in the square-shaped sample, while the ring-shaped sample shows a 0.040 T increase in anisotropy due to the particle alignment.

High frequency permeability measurement is performed on the ring-shaped samples from 1 to 3 GHz (Fig. 6.8). Compared with the unaligned sample, the real part of permeability in the aligned sample greatly improves as frequency increases (a 77% increase at 3 GHz); the imaginary part of permeability stays relatively the same.

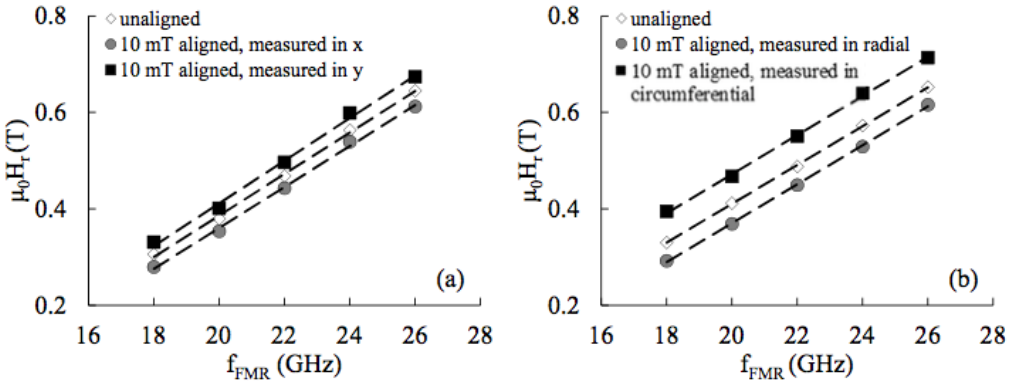

Fig. 6.7 FMR frequency, f_{FMR}, dependence of the resonance field, H_r, for (a) square-shaped samples in both x- and y-directions, and (b) ring-shaped samples in both radial and circumferential directions. (Reprinted with permission from Song *et al.* [83].)

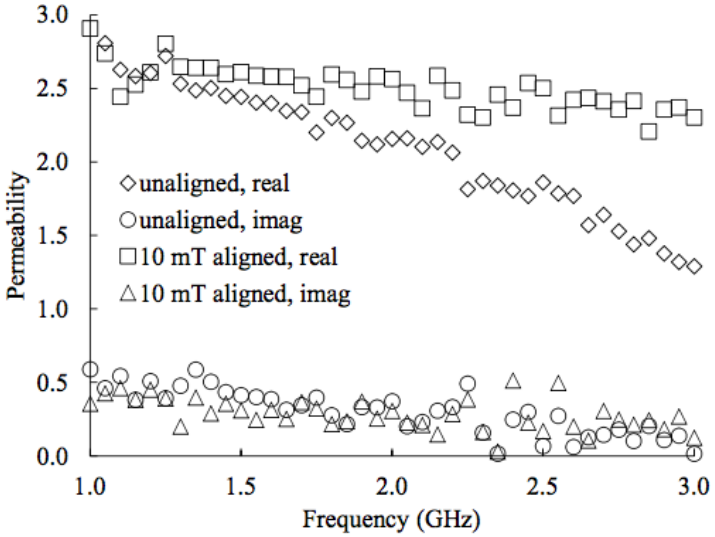

Fig. 6.8 Complex permeability of an unaligned ring-shaped sample and a 10 mT aligned, ring-shaped sample in the frequency range of 1 to 3 GHz. (Reprinted with permission from Song *et al.* [83].)

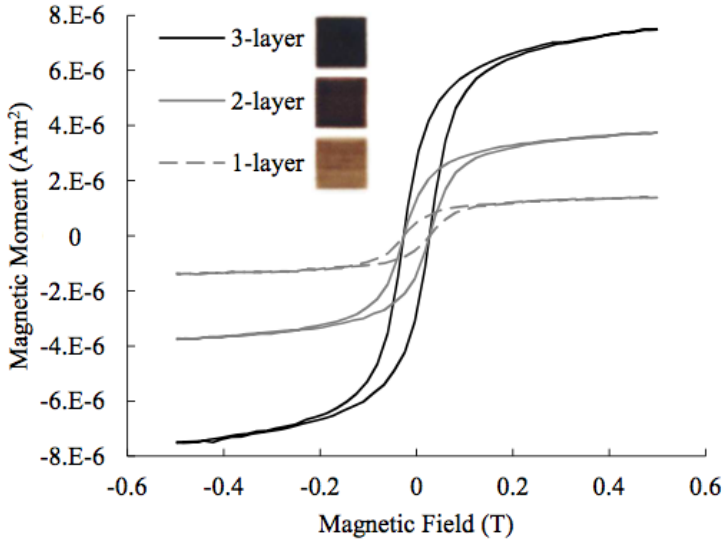

Fig. 6.9 Hysteresis curves and photos of the square-shaped samples with varying numbers of layers [83].

Photos and hysteresis loops of printed samples with varying numbers of layers (MICR - Objet sample C1, C2 and C3) are shown in Fig. 6.9. The opacity of samples is seen to increase with the number of layers. Similarly, with increasing number of layers (that is, increasing magnetic nanoparticle content) the saturation magnetic moment of the printed sample increases. However, the magnetic moment does not scale proportionally with the number of layers, which is caused by magnetic particle sedimentation in the ink reservoir over time. The ink composition still needs optimization to improve stability and nanoparticle loading before practical use.

6.5 Summary

A 3D magnetic inkjet printing technique with arbitrary magnetic alignment and UV-curing capability is developed. A magnetic nanoparticle suspension is inkjet printed, aligned with a programmable electromagnet, and characterized magnetically. The magnetic alignment is demonstrated to increase the permeability and reduce hysteresis loss in the alignment-induced hard axis direction. With further magnetic ink optimization to improve particle shape anisotropy, magnetic nanoparticle loading, and ink stability, inkjet printed magnetic devices will have the potential to meet the customization and performance needs of future high frequency magnetic components.

CHAPTER 7. EFFECT OF VOLUME FRACTION AND COMPOSITE SHAPE

7.1 Introduction

By increasing volume fraction and optimizing composite shape, composite demagnetizing field can also be used to enhance the high frequency magnetic properties of composite materials. As discussed in Section 2.8, Ramprasad's model [9-10] predicts that the high frequency magnetic behavior in composites is influenced by particle anisotropy, volume fraction and composite shape in a complex way. In this effort, $NiFe_2O_4$ nanocomposites consisting of commercially available $NiFe_2O_4$ nanopowder in a non-magnetic matrix is used as the study system, and an experimental study on the effect of volume fraction, composite shape and orientation on high frequency permeability and magnetic anisotropy is presented.

7.2 Sample Preparation

Two types of magnetic nanocomposite samples are fabricated: pellet-shaped $NiFe_2O_4$ - KBr nanocomposite samples for magnetic hysteresis and ferromagnetic resonance study, and toroid-shaped $NiFe_2O_4$ - Epoxy nanocomposite samples for high frequency permeability measurement.

To prepare the pellet-shaped magnetic nanocomposite samples, near spherical $NiFe_2O_4$ nanopowder (MTI Corporation, CA, USA, average diameter = 30 nm. See Fig. 7.1a) are first mixed with a non-magnetic binder (potassium bromide, KBr) in a mortar. The powder mixture is then compressed into pellet-shaped composites (7 mm in diameter, 1 mm in thickness) using a hand press (E-Z™ Quick table top press, International Crystal Laboratories, NJ, USA. See Fig.7.1b) under zero magnetic field. A series of samples with volume fractions ranging from 0.5 to 31.6 vol% are made (see Table 7.1).

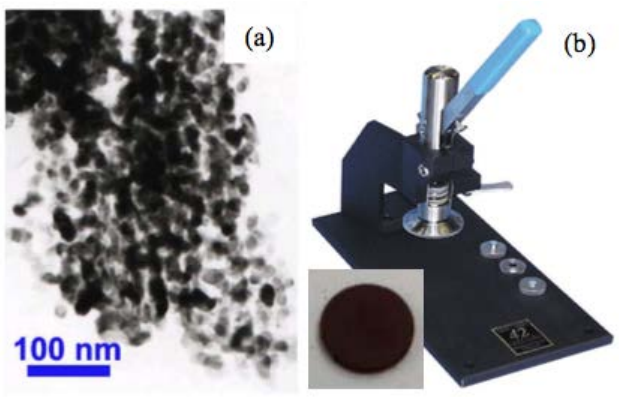

Fig. 7.1 (a) TEM image of $NiFe_2O_4$ nanopowder with an average diameter of 30 nm (photo courtesy of MTI Corporation). (b) E-Z™ Quick table top press (photo courtesy of International Crystal Laboratories). The inset shows the 20.4 vol% pellet-shaped $NiFe_2O_4$ - KBr nanocomposite samples.

Table 7.1 A list of pellet-shaped $NiFe_2O_4$ - KBr nanocomposite samples.

Sample #	$NiFe_2O_4$ - KBr Weight Ratio	$NiFe_2O_4$ Volume Fraction
A1	1 : 100	0.5 vol%
A2	2 : 100	1.0 vol%
A3	5 : 100	2.5 vol%
A4	10 : 100	4.9 vol%
A5	20 : 100	9.3 vol%
A6	30 : 100	13.3 vol%
A7	50 : 100	20.4 vol%
A8	70 : 100	26.4 vol%
A9	90 : 100	31.6 vol%

Toroid-shaped magnetic nanocomposite samples are made by first dispersing the $NiFe_2O_4$ nanopowder in a two-part Epoxy (105 Epoxy Resin / 205 Fast Hardener, 5:1 mixing ratio, West System Inc., MI, USA). The resulting

suspension is then molded into a toroid (7.2 mm outer diameter, 3.6 mm inner diameter, 3 mm thick) and cured in air. Three samples with different volume fractions are made (see Table 7.2). The achievable highest volume fraction is limited by the curability of $NiFe_2O_4$ - Epoxy suspension.

Table 7.2 A list of toroid-shaped $NiFe_2O_4$ - Epoxy nanocomposite samples.

Sample #	$NiFe_2O_4$ - Epoxy Weight Ratio	$NiFe_2O_4$ Volume Fraction
B1	20 : 100	3.8 vol%
B2	35 : 100	6.5 vol%
B3	50 : 100	9.1 vol%

7.3 Characterization Techniques

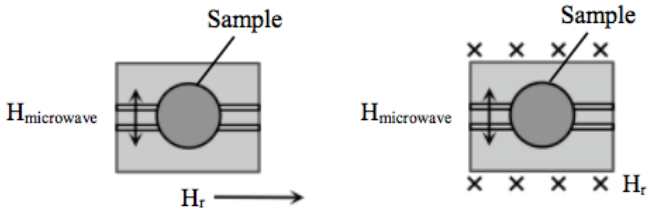

Fig. 7.2 In-plane and out-of-plane FMR measurement configurations. $H_{microwave}$ is the microwave field. H_r is the resonance field. (Reprinted with permission from Song *et al*. [85].)

The toroid-shaped $NiFe_2O_4$ - Epoxy nanocomposite samples are put in the impedance analyzer for high frequency permeability measurement. The real part of the complex permeability is measured from 0.5 to 2 GHz, and compared between different volume fractions.

The pellet-shaped $NiFe_2O_4$ - KBr nanocomposite samples are first measured out-of-plane by VSM, are then characterized by FMR spectrometer to further study the effect of volume fraction and composite shape on magnetic anisotropy. All samples were measured with the *dc* field directed both in-plane and perpendicular

to the pellet (out-of-plane), as shown in Fig. 7.2, to investigate the effect of composite shape and orientation on ferromagnetic resonance. Reproducibility of the results is verified by measuring multiple samples for each volume fraction.

7.4 Results and Discussion

Plotted in Fig. 7.3 is the high frequency permeability measured in toroid-shaped nanocomposite samples with varying volume fractions. As volume fraction increases from 3.8 to 9.1 vol%, the real part of permeability increases from 1.04 to 1.27, which is expected from the effective medium theory.

The effect of volume fraction is also shown on hysteresis loops of pellet-shaped nanocomposite samples (Fig. 7.4). The out-of-plane hysteresis loops are first normalized and then zoomed-in for better comparison of magnetic anisotropy. With volume fraction increased from 0.5 to 31.6 vol%, the hysteresis loop becomes more linear, transitioning to a hard axis like response and indicating a rise in magnetic anisotropy.

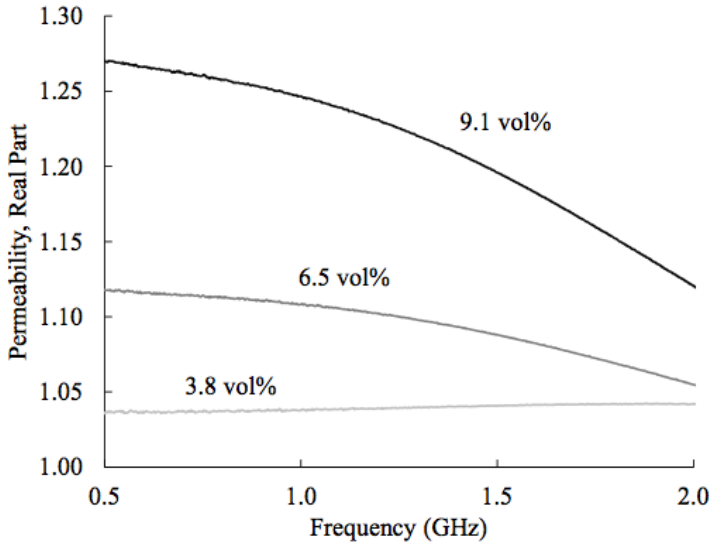

Fig. 7.3 Real part of permeability measured from toroid-shaped nanocomposite samples with different volume fractions.

FMR measurement of pellet-shaped nanocomposite samples, both in-plane and out-of-plane, are carried out to study the effect of volume fraction and composite shape on magnetic anisotropy. The lock-in detection FMR setup measures the field derivative of absorbed microwave power (dP / dH) as a function of the applied *dc* magnetic field. Example FMR signal traces, obtained from out-of-plane measurement of a 20.4 vol% pellet-shaped sample, are shown in Fig. 7.5. The zero crossing (indicated by solid circles) corresponds to the peak in microwave absorption, and thus, identifies the resonance field, H_r.

As discussed in Section 2.6, the ferromagnetic resonance of an ideal bulk magnetic sample without any anisotropy is

$$f_{FMR} = \frac{\gamma}{2\pi} \mu_0 H_r \, . \tag{7.1}$$

While for a composite of finite shape the above equation is modified as

$$f_{FMR} = \frac{\gamma}{2\pi} \mu_0 (H_r + H_{int}) \, , \tag{7.2}$$

with $H_{int} = H_{dem} + H_{pa}$. H_{dem} is the demagnetizing field within the composite, and H_{pa} the particle anisotropy field.

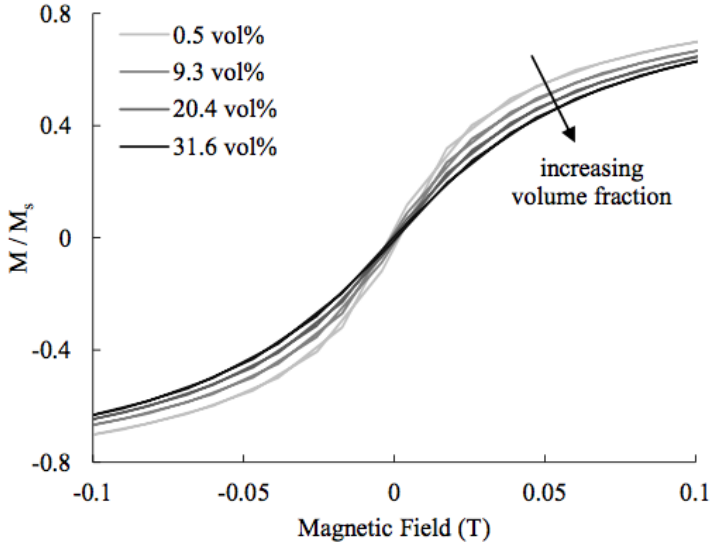

Fig. 7.4 Normalized hysteresis loops of pellet-shaped nanocomposite samples with different volume fractions. The magnetic field is applied in out-of-plane direction.

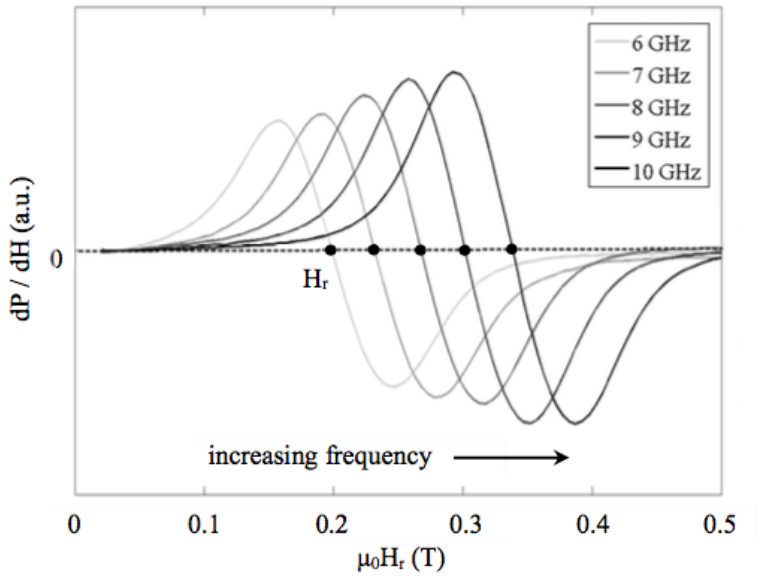

Fig. 7.5 FMR responses (out-of-plane) of a 20.4 vol% pellet-shaped $NiFe_2O_4$ nanocomposite sample measured from 6 to 10 GHz. (Reprinted with permission from Song *et al*. [85].)

The demagnetizing field, H_{dem}, which acts against the resonance field, H_r, is determined by saturation magnetization of the magnetic particles, volume fraction, composite shape and orientation. In this study, no magnetic alignment is applied when preparing the nanocomposite samples. Therefore, unlike the composite samples in Chapters 5 and 6, the particles are randomly oriented in the matrix. The particle anisotropy term, H_{pa}, is an effective field arising from the particle shape anisotropy and magnetocrystalline anisotropy. Due to the random orientations, H_{pa} has no orientation dependence, and would remain the same for different particle volume fractions, composite shapes and orientations.

As discussed in Section 2.8, at the isolated particle limit, the demagnetizing field, H_{dem}, becomes negligible, leaving only particle anisotropy, H_{pa}, to influence the resonance. In this case, by extrapolating the internal magnetic field, H_{int}, to zero vol% the average particle anisotropy, H_{pa}, can be estimated. On the other hand, though not experimentally possible, the internal magnetic field, H_{int}, of a magnetic composite approaching 100 vol% would be dominated by the demagnetizing field,

H_{dem}. Thus the resonance response, in this case, would follow Kittel's equation (Eqn. (2.14)):

$$f_{FMR} = \frac{\gamma}{2\pi}\mu_0\sqrt{(H_r + (N_y - N_z)M_s)(H_r + (N_x - N_z)M_s)}\,, \qquad (7.3)$$

In-between these two extreme cases, the resonance response gradually transitions from that of isolated magnetic particles to that of a single-phase magnetic material.

Fig. 7.6 shows FMR frequency, f_{FMR}, dependence of the resonance field, H_r, in pellet-shaped $NiFe_2O_4$ nanocomposite samples with different volume fractions. As the particles become more closely packed, the resonance field, H_r, is seen to decrease for in-plane measurements, while increase for out-of-plane measurements. An "ideal bulk" response, which is described by Eqn. (7.1), is also plotted for comparison. According to Eqn. (7.2), the internal magnetic field, H_{int}, can be extracted from the vertical offset of the measured responses from the "ideal bulk" trace, which is plotted as a function of volume fraction in Fig. 7.6 inset. The average particle anisotropy of 0.041 T is obtained by extrapolation of the in-plane and out-of-plane measurements to zero volume fraction. By conducting similar measurements, particle anisotropy between different magnetic particles can be compared.

As the volume fraction increases, due to the differing effects of demagnetizing field, the in-plane and out-of-plane curves of H_{int} diverge. The increasingly strong out-of-plane demagnetizing field is perpendicular to H_r in the in-plane measurement, and opposite to H_r in the out-of-plane measurement. Therefore, the FMR frequency, f_{FMR}, raises for in-plane measurements, while decreases for out-of-plane measurements.

This result is normalized to the "ideal bulk" response given by Eqn. (7.1) and compared with Ramprasad's model [9-10] (Fig. 7.7). The model uses spherical (no shape anisotropy) and rod-shaped (high shape anisotropy) particles made from the same material, and studies the FMR frequency of magnetic composites with varying volume fractions.

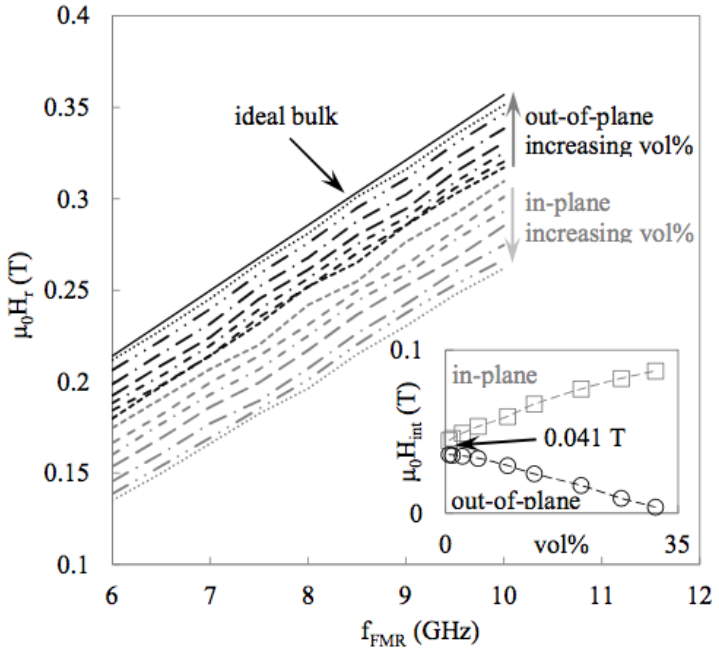

Fig. 7.6 FMR frequency, f_{FMR}, dependence of the resonance field, H_r, in pellet-shaped $NiFe_2O_4$ nanocomposite samples with different volume fractions. The "ideal bulk" line is given by Eqn. (7.1). The inset shows the derived effective internal magnetic field, H_{int}, as a function of volume fraction and composite orientation. (Reprinted with permission from Song *et al.* [85].)

At the isolated particle limit, the response of $NiFe_2O_4$ nanocomposites lie slightly above the modeled sphere-shaped particles, indicating a small particle shape anisotropy. This is supported by the reported near-spherical shape of $NiFe_2O_4$ nanopowder. As the particles become more closely packed, the demagnetizing field starts to dictate the FMR response. Approaching 100 vol%, the modeled curves collapse to values of the assumed sample geometries, either an infinite thin film or a "bulk" sample of infinite extent in all dimensions, for both spherical and rod-shaped particles. The single-phase limit is calculated for pellet-shaped nanocomposites using Kittel's equation (Eqn. (7.3)), and plotted on Fig. 7.7. Although the results are limited at 31.6 vol% experimentally, the curves for the in-plane and out-of-plane measurements are trending toward their respective limits.

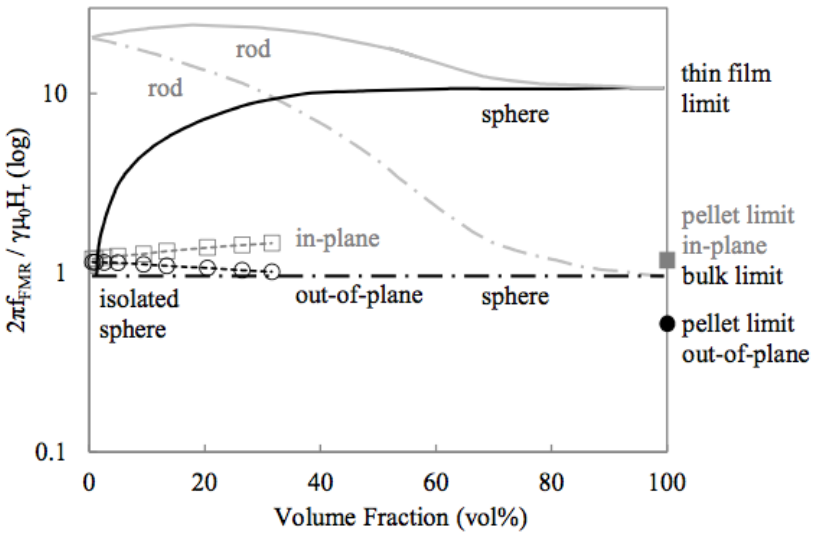

Fig. 7.7 Comparison between Ramprasad's model and experimentally measured FMR frequency normalized by ($\gamma\mu_0 H_r$ / 2π) for different volume fractions. (Reprinted with permission from Song *et al*. [85].)

7.5 Summary

Effects of volume fraction, composite shape and orientation are investigated on magnetic nanocomposites consisting of $NiFe_2O_4$ nanopowder in a non-magnetic matrix by VSM, FMR, and high frequency permeability measurements. As the particles become more closely packed, improvements in both high frequency permeability and magnetic anisotropy are observed in composites. The total magnetic anisotropy of the composite is found to be determined by the sometimes-competing influences of composite demagnetizing field and particle shape anisotropy.

CHAPTER 8. CONCLUSIONS AND FUTURE WORK

8.1 Conclusions

To achieve high frequency operations for the integrated inductor and antenna applications, the soft magnetic composite must meet the following requirements: 1) high permeability, 2) high ferromagnetic resonance frequency, 3) low hysteresis loss, and 4) low eddy current loss. In particular, planar magnetic anisotropy needs to be introduced to the composites to overcome the Snoek's limit, which enables simultaneous high ferromagnetic resonance frequency and high permeability.

In this effort, the effects of constituent particle shape and alignment, composite volume fraction and shape on the microstructural and magnetic properties are examined in Ni-Fe microdisk composites and $NiFe_2O_4$ nanocomposites, respectively. The total magnetic anisotropy of the composite is found to be determined by the sometimes-competing influences of composite demagnetizing field and particle shape anisotropy.

By aligning the particle shape anisotropy of individual Ni-Fe microdisks under an in-plane rotating field, planar anisotropy is introduced to the composites, and Snoek's limit is overcome to achieve both high permeability and high ferromagnetic resonance frequency. This planar alignment process is then examined by a systemic experimental and theoretical study of magnetic disk rotation in a Newtonian fluid. A planar alignment process with high fluid viscosity, high field rotation frequency, and low aligning field strength is recommended, which can uniformly align microdisks with different initial in-plane orientations. This insensitivity to initial orientations enables precise control of the magnetic disk orientations by applying various durations of the aligning field. From this insight, varying degrees of planar anisotropy are obtained in Ni-Fe microdisk composites without chaining of particles. This process is a promising technique for customizing composites for high frequency operations.

The above principles also enable fast prototyping of magnetic components by an inkjet printer. By magnetic alignment of a magnetic nanoparticle bearing ink, samples with arbitrary anisotropy alignment are printed and tested, demonstrating a 3D magnetic printing technique with great potential.

8.2 Future Work

This dissertation work opens up several opportunities for future research in magnetic disk rotation modeling, magnetic particle chaining modeling, and UV-curable magnetic ink development.

1) The theoretical model of magnetic disk rotation predicts that at the low ξ region ($\xi < 1$), the cos θ versus τ curves start to show steps (Fig. 5.2a), because the field rotation is slow enough for the disk rotation to catch up from time to time. And the alignment time becomes sensitive to the initial azimuthal angle, ϕ_0, as shown in Fig. 5.2b. Experimental verification of the model at low to medium ξ region can be conducted by applying an aligning field with a frequency ranging from 0.1 to 1 Hz to the Ni-Fe microdisk suspension. To study the effect of initial azimuthal angle on alignment time, the starting orientations of Ni-Fe microdisks can be fixed by applying an out-of-plane rotating field (for example, in (x_1,x_3)-plane in Fig. 5.1b), and the ϕ_0 can be set by starting the in-plane rotation at the corresponding angle. A LabVIEW program that can fast switch between out-of-plane and in-plane field rotations and configure the starting angle of in-plane rotation is necessary for improving the automation and repeatability of this measurement.

2) The good agreement between the measured results of Ni-Fe microdisk alignment and the theoretical model suggests that the model can be extended to other particle dimensions, in particular nanoparticles, for which the rotation dynamics cannot be observed by optical microscopy. At nanometer scale, the randomizing torque from Brownian motion can no longer be

ignored. A modified model that takes Brownian motion into consideration can be developed, and compared with the magnetic properties of aligned and cured magnetic nanodisk composites. This is also crucial for understanding the alignment process in magnetic inkjet printing, in which the magnetic nanoparticle alignment, ink thinner evaporation, and ink absorption by the substrate happen simultaneously.

3) With increasing volume fraction, chaining of magnetic particles becomes more significant due to the decreasing distance between particles. Particle interactions in two-particle and multiple-particle systems can be observed by optical microscopy and simulated to study the effect of volume fraction and aligning field strength.

4) Complex fluids, such as UV-resins with yield stress, can be used to arrest magnetic particle chaining [78]. The magnetic particles are relatively free to rotate in the matrix, but the translational motion from particle chaining is hindered by the yield stress. Theoretical and experimental studies can be carried out to study this effect.

5) As discussed in Chapter 6, the MICR - Objet ink suffers from low magnetic particle loading and sedimentation over time. To enable a 3D magnetic printing technique that can print and cure multi-layer samples with controlled anisotropy, development of a UV-curable magnetic ink with highly anisotropic particles, good stability, and high volume fraction is pivotal.

BIBLIOGRAPHY

[1] M. Yamaguchi, K. H. Kim, S. Ikedaa, "Soft magnetic materials application in the RF range," *J. Magn. Magn. Mater.*, vol. 304, no. 2, pp. 208-213 (2006).

[2] L. J. Martin, S. Ooi, D. Staiculescu, M. D. Hill, C. P. Wong, M. M. Tentzeris, "Effect of permittivity and permeability of a flexible magnetic composite material on the performance and miniaturization capability of planar antennas for RFID and wearable wireless applications," *IEEE Trans. Compon. Packag. Technol.*, vol. 32, no. 4, pp. 849-858 (2009).

[3] S. H. Park, W. K. Ahn, J. S. Kum, J. K. Ji, K. H. Kim, W. M. Seong, "Electromagnetic properties of dielectric and magnetic composite material for antenna," *Electron. Mater. Lett.*, vol. 5, no. 2, pp. 67-71 (2009).

[4] H. Greve, C. Pochstein, H. Takele, V. Zaporojtchenko, F. Faupel, A. Gerber, M. Frommberger, E. Quandt, "Nanostructured magnetic Fe–Ni–Co/Teflon multilayers for high-frequency applications in the gigahertz range," *Appl. Phys. Lett.*, vol. 89, no. 24, 242501 (2006).

[5] C. Yang, F. Liu, T. Rena, L. Liu, H. Feng, A. Z. Wang, H. Long, "Fully integrated ferrite-based inductors for RF ICs," *Sensor Actuat. A-Phys.*, vol. 130-131, pp. 365-370 (2006).

[6] Y. Zhuang, M. Vroubel, B. Rejaei, J. N. Burghartz, "Integrated RF inductors with micro-patterned NiFe core," *Solid-State Electron.*, vol. 51, no. 3, pp. 405-413 (2007).

[7] T. Miki, T. Ohya, H. Yoshino, N. Umeda, "The overview of the 4th generation mobile communication system," *2005 Fifth International Conference on Information, Communications and Signal Processing*, pp. 1600-1604 (2005).

[8] F. Mazaleyrata, L. K. Varga, "Ferromagnetic nanocomposites," *J. Magn. Magn. Mater.*, vol. 215-216, pp. 253-259 (2000).

[9] R. Ramprasad, P. Zurcher, M. Petras, M. Miller, P. Renaud, "Fundamental limits of soft magnetic particle composites for high frequency applications," *Phys. Stat. Sol. (b)*, vol. 233, no. 1, pp. 31-38 (2002).

[10] R. Ramprasad, P. Zurcher, M. Petras, M. Miller, P. Renaud, "Magnetic properties of metallic ferromagnetic nanoparticle composites," *J. Appl. Phys.*, vol. 96, no. 1, pp. 519-529 (2004).

[11] S. Chikazumi, "Physics of ferromagnetism, second edition," *Oxford University Press* (1997).

[12] R. M. Bozorth, "Ferromagnetism," *IEEE Press* (1993).

[13] Ümit Özgür, Yahya Alivov, Hadis Morkoç, "Microwave ferrites, part 1: fundamental properties," *J. Mater. Sci. Mater. Electron.*, vol. 20, no. 9, pp. 789-834 (2009).

[14] S. Bedanta, W. Kleemann, "Supermagnetism," *J. Phys. D: Appl. Phys.*, vol. 42, no. 1, 013001 (2009).

[15] R. S. de Biasi, T. C. Devezas, "Anisotropy field of small magnetic particles as measured by resonance," *J. Appl. Phys.*, vol. 49, no. 4, pp. 2466-2469 (1978).

[16] J. A. Osborn, "Demagnetizing factors of the general ellipsoid," *Phys. Rev.*, vol. 67, no. 11-12, pp. 351-357 (1945).

[17] R. I. Joseph, "Ballistic demagnetizing factor in uniformly magnetized cylinders," *J. Appl. Phys.*, vol. 37, no. 13, pp. 4639-4643 (1966).

[18] T. Tsutaoka, "Frequency dispersion of complex permeability in Mn–Zn and Ni–Zn spinel ferrites and their composite materials," *J. Appl. Phys.*, vol. 93, no. 5, pp. 2789-2796 (2003).

[19] L. Landau, E. Lifshitz, "On the theory of the dispersion of magnetic permeability in ferromagnetic bodies," *Phys. Zeitsch. der Sow.*, vol. 8, pp. 153-169 (1935).

[20] C. Kittel, "On the theory of ferromagnetic resonance absorption," *Phys. Rev.*, vol. 73, no. 2, pp. 155-161 (1948).

[21] M. Farle, "Ferromagnetic resonance of ultrathin metallic layers," *Rep. Prog. Phys.*, vol. 61, no. 7, pp. 755-826 (1998).

[22] J. Smith, H. G. Beljers, "Ferromagnetic resonance absorption in $BaFe_{12}O_{19}$, a highly anisotropic crystal," *Phillips Res. Rep.*, vol. 10, no. 2, pp. 113-130 (1955).

[23] Kh. Zakeri, J. Lindner, I. Barsukov, R. Meckenstock, M. Farle, U. von Hörsten, H. Wende, W. Keune, J. Rocker, S. S. Kalarickal, K. Lenz, W. Kuch, K. Baberschke, Z. Frait, "Spin dynamics in ferromagnets: Gilbert damping and two-magnon scattering," *Phys. Rev. B*, vol. 76, no. 10, 104416 (2007).

[24] J. M. Beaujour, D. Ravelosona, I. Tudosa, E. E. Fullerton, A. D. Kent, "Ferromagnetic resonance linewidth in ultrathin films with perpendicular magnetic anisotropy," *Phys. Rev. B*, vol. 80, no. 18, 180415(R) (2009).

[25] K. D. Sossmeier, F. Beck, R. C. Gomes, L. F. Schelp. M. Carara, "Ferromagnetic resonance linewidth mechanisms in annealed CoFeSiB glass-covered microwires," *J. Phys. D: Appl. Phys.*, vol. 43, no. 5, 055003 (2010).

[26] H. T. Nembach, T. J. Silva, J. M. Shaw, M. L. Schneider, M. J. Carey, S. Maat, J. R. Childress, "Perpendicular ferromagnetic resonance measurements of damping and Landé g-factor in sputtered $(Co_2Mn)_{1-x}Ge_x$ thin films," *Phys. Rev. B*, vol. 84, no. 5, 054424 (2011).

[27] J. L. Snoek, "Dispersion and absorption in magnetic ferrites at frequencies above one Mc/s," *Physica*, vol. 14, no. 4, pp. 207-217 (1948).

[28] D. S. Xue, F. S. Li, X. L. Fan, F. S. Wen, "Bianisotropy picture of higher permeability at higher frequencies," *Chin. Phys. Lett.*, vol. 25, no. 11, pp. 4120-4123 (2008).

[29] K. N. Rozanov, Z. W. Li, L. F. Chen, M. Y. Koledintseva, "Microwave permeability of Co_2Z composites," *J. Appl. Phys.*, vol. 97, no. 1, 013905 (2005).

[30] R. M. Walser, W. Win, P. M. Valanju, "Shape-optimized ferromagnetic particles with maximum theoretical microwave susceptibility," *IEEE Trans. Magn.*, vol. 34, no. 4, pp. 1390-1392 (1998).

[31] D. A. G. Bruggeman, "Berechnung verschiedener physikalischer konstanten von heterogenen substanzen," *Ann. Phys. (Germany)*, vol. 24, no. 7, pp. 636-664 (1935).

[32] L. Z. Wu, J. Ding, H. B. Jiang, C. P. Neo, L. F. Chen, C. K. Ong, "High frequency complex permeability of iron particles in a nonmagnetic matrix," *J. Appl. Phys.*, vol. 99, no. 8, 083905 (2006).

[33] A. N. Largakov, K. N. Rozanov, “High-frequency behavior of magnetic composites,” *J. Magn. Magn. Mater.*, vol. 321, no. 14, pp. 2082-2092 (2009).

[34] T. Liu, P. H. Zhou, L. J. Deng, W. Tang, “Spatial orientation and position distribution effect on the effective permeability of composites consisting of aligned flakes,” *J. Appl. Phys.*, vol. 106, no. 11, 114904 (2009).

[35] J. H. Paterson, R. Devine, A. D. R. Phelps, “Complex permeability of soft magnetic ferrite/polyester resin composites at frequencies above 1 MHz,” *J. Magn. Magn. Mater.*, vol. 196-197, pp. 394-396 (1999).

[36] H. Shokrollahi, K. Janghorban, “Soft magnetic composite materials (SMCs),” *J. Mater. Process. Technol.*, vol. 189, no. 1-3, pp. 1-12 (2007).

[37] B. C. Webb, M. E. Re, C. V. Jahnes, M. A. Russak, “High-frequency permeability of laminated and unlaminated, narrow, thin-film magnetic stripes,” *J. Appl. Phys.*, vol. 69, no. 8, pp. 5611-5615 (1991).

[38] A. V. Svalov, I. R. Aseguinolaza, A. Garcia-Arribas, I. Orue, J. M. Barandiaran, J. Alonso, M. L. Fernández-Gubieda, G. V. Kurlyandskaya, “Structure and magnetic properties of thin permalloy films near the transcritical state,” *IEEE Trans. Magn.*, vol. 46, no. 2, pp. 333-336 (2010).

[39] E. F. Kneller, F. E. Luborsky, “Particle size dependence of coercivity and remanence of single-domain particles,” *J. Appl. Phys.*, vol. 34, no. 3, pp. 656-658 (1963).

[40] D. Hasegawa, H.Yang, T. Ogawa, M. Takahashi, “Challenge of ultrahigh frequency limit of permeability for magnetic nanoparticle assembly with organic polymer—Application of superparamagnetism,” *J. Magn. Magn. Mater.*, vol. 321, no. 7, pp. 746-749 (2009).

[41] Xian Wang, R. Gong, P. Li, L. Liu, W. Cheng, “Effects of aspect ratio and particle size on the microwave properties of Fe–Cr–Si–Al alloy flakes,” *Mater. Sci. Eng., A*, vol. 466, no. 1-2, pp. 178-182 (2007).

[42] H. Yun, X. Liu, T. Paik, D. Palanisamy, J. Kim, W. D. Vogel, A. J. Viescas, J. Chen, G. C. Papaefthymiou, J. M. Kikkawa, M. G. Allen, C. B. Murray, “Size- and composition-dependent radio frequency magnetic permeability of iron oxide nanocrystals,” *ACS Nano*, vol. 8, no. 12, pp. 12323–12337 (2014).

[43] N. N. Song, H. T. Yang, H. L. Liu, X. Ren, H. F. Ding, X. Q. Zhang, Z. H. Cheng, "Exceeding natural resonance frequency limit of monodisperse Fe_3O_4 nanoparticles via superparamagnetic relaxation," *Sci. Rep.*, vol. 3, 3161 (2013).

[44] S. S. Kim, S. T. Kim, Y. C. Yoon, K. S. Lee, "Magnetic, dielectric, and microwave absorbing properties of iron particles dispersed in rubber matrix in gigahertz frequencies," *J. Appl. Phys.*, vol. 97, no. 10, 10F905 (2005).

[45] P. H. Zhou, L. J. Deng, J. L. Xie, D. F. Liang, "Effects of particle morphology and crystal structure on the microwave properties of flake-like nanocrystalline Fe_3Co_2 particles," *J. Alloys Compd.*, vol. 448, no. 1-2, pp. 303–307 (2008).

[46] M. Han, W. Tang, W. Chen, H. Zhou, L. Deng, "Effect of shape of Fe particles on their electromagnetic properties within 1-18 GHz range," *J. Appl. Phys.*, vol. 107, no. 9, 09A958 (2010).

[47] R. B. Yang, W. F. Liang, "Microwave properties of high-aspect-ratio carbonyl iron/epoxy absorbers," *J. Appl. Phys.*, vol. 109, no. 7, 07A311 (2011).

[48] B. Weidenfeller, M. Anhalt, W. Riehemann, "Variation of magnetic properties of composites filled with soft magnetic FeCoV particles by particle alignment in a magnetic field," *J. Magn. Magn. Mater*., vol. 320, no. 14, pp. e362-e365 (2008).

[49] W. Yang, L. Qiao, J. Wei, Z. Zhang, T. Wang, F. Li, "Microwave permeability of flake-shaped FeCuNbSiB particle composite with rotational orientation," *J. Appl. Phys.*, vol. 107, no. 3, 033913 (2010).

[50] X. Chi, H. Yi, W. Zuo, L. Qiao, T. Wang, F. Li, "Complex permeability and microwave absorption properties of Y_2Fe_{17} micropowders with planar anisotropy," *J. Phys. D: Appl. Phys.*, vol. 44, no. 29, 295001 (2011).

[51] R. Han, L. Qiao, T. Wang, F. Li, "Microwave complex permeability of planar anisotropy carbonyl-iron particles," *J. Alloys Compd.*, vol. 509, no. 6, pp. 2734-2737 (2011).

[52] X. Liu, S. W. Or, C. M. Leung, S. L. Ho, "Microwave complex permeability of Fe_3O_4 nanoflake composites with and without magnetic field-induced rotational orientation," *J. Appl. Phys.*, vol. 113, no. 17, 17B307 (2013).

[53] M. Anhalta, B. Weidenfeller, “Magnetic properties of polymer bonded soft magnetic particles for various filler fractions,” *J. Appl. Phys.*, vol. 101, no. 2, 023907 (2007).

[54] S. Foner, “Versatile and sensitive vibrating-sample magnetometer,” *Rev. Sci. Instrum.*, vol. 30, no. 7, pp. 548-557 (1959).

[55] B. D. Cullity, C. D. Graham, “Introduction to magnetic materials, second edition,” *IEEE Press*, pp. 67-70 (2009).

[56] S. S. Kalarickal, P. Krivosik, M. Z. Wu, C. E. Patton, M. L. Schneider, P. Kabos, T. J. Silva, J. P. Nibarger, “Ferromagnetic resonance linewidth in metallic thin films: Comparison of measurement methods,” *J. Appl. Phys.*, vol. 99, no. 9, 093909 (2006).

[57] C. Bilzer, T. Devolder, P. Crozat, C. Chappert, S. Cardoso, P. P. Freitas, “Vector network analyzer ferromagnetic resonance of thin films on coplanar waveguides: Comparison of different evaluation methods,” *J. Appl. Phys.*, vol. 101, no. 7, 074505 (2007).

[58] B. Buford, P. Dhagat, A. Jander, “A technique for error estimation of linewidth and damping parameters extracted from ferromagnetic resonance measurements,” *J. Appl. Phys.*, vol. 117, no. 17, 17E109 (2015).

[59] L. Sun, K. Keshoju, H. Xing, “Magnetic field mediated nanowire alignment in liquids for nanocomposite synthesis,” *Nanotechnology*, vol. 19, 405603 (2008).

[60] T. Kimura, M. Yamato, W. Koshimizu, M. Koike, T. Kawai, “Magnetic orientation of polymer fibers in suspension,” *Langmuir*, vol. 16, no. 2, pp. 858-861 (2000).

[61] Y. Gu, R. Burtovyy, J. Townsend, J. R. Owens, I. Luzinov, K. G. Kornev, “Collective alignment of nanorods in thin Newtonian films,” *Soft Matter*, vol. 9, pp. 8532-8539 (2013).

[62] Y. Gu, K. G. Kornev, “Alignment of magnetic nanorods in solidifying films,” *Part. Part. Syst. Charact.*, vol. 30, pp. 958-963 (2013).

[63] Y. D. Zhang, J. I. Budnick, W. A. Hines, “Three dimensional alignment of magnetic particles,” *J. Appl. Phys.*, vol. 81, no. 8, pp. 5647-5649 (1997).

[64] S. Melle, M. A. Rubio, G. G. Fuller, “Orientation dynamics of magnetorheological fluids subject to rotating external fields,” *Int. J. Mod. Phys. B*, vol. 15, no. 6-7, pp. 758-766 (2001).

[65] T. Kimura, M. Yoshino, T. Yamane, M. Yamato, M. Tobita, “Uniaxial alignment of the smallest diamagnetic susceptibility axis using time-dependent magnetic fields,” *Langmuir*, vol. 20, no. 14, pp. 5669-5672 (2004).

[66] T. Kimura, “Orientation of feeble magnetic particles in dynamic magnetic fields,” *Jpn. J. Appl. Phys.*, vol. 48, 020217 (2009).

[67] M. Yamaguchi, S. Ozawa, I. Yamatmoto, “Dynamic behavior of magnetic alignment in rotating field for magnetically weak particles,” *Jpn. J. Appl. Phys.*, vol. 49, no. 8, 080213 (2010).

[68] S. Tsukui, T. Kimura, “Magnetic alignment of magnetically biaxial diamagnetic rods under rotating magnetic fields,” *Jpn. J. Appl. Phys.*, vol. 51, no. 5, 057301 (2012).

[69] R. M. Erb, J. Segmehl, M. Charilaou, J. F. Loffler, A. R. Studart, “Non-linear alignment dynamics in suspensions of platelets under rotating magnetic fields,” *Soft Matter*, vol. 8, no. 29, pp. 7604-7609 (2012).

[70] R. M. Erb, R. Libanori, N. Rothfuchs, A. R. Studart, “Composites reinforced in three dimensions by using low magnetic fields,” *Science*, vol. 335, no. 6065, pp. 199-204 (2012).

[71] R. Libanori, R. M. Erb, A. R. Studart, “Mechanics of platelet-reinforced composites assembled using mechanical and magnetic stimuli,” *ACS Appl. Mater. Interfaces*, vol. 5, no.21, pp. 10794-10805 (2013).

[72] S. Kim, C. J. Lawrence, “Similarity solutions for the orientation distribution function and rheological properties of suspensions of axisymmetric particles with external couples,” *J. Non-Newton Fluid*, vol. 24, no. 3, pp. 297-310 (1987).

[73] S. Kim, S. J. Karrila, “Microhydrodynamics: principles and selected applications,” *Dover Publications*, pp. 61-69 (2005).

[74] V. Raman, A. Bose, B. D. Olsen, T. A. Hatton, “Long-range ordering of symmetric block copolymer domains by chaining of superparamagnetic nanoparticles in external magnetic fields,” *Macromolecules*, vol. 45, no. 23, pp. 9373-9382 (2012).

[75] K. van Netten, J. Zhou, K. P. Galvin, R. Moreno-Atanasio, “Influence of magnetic and hydrodynamic forces on chain-aggregation and motion of magnetisable particles and composites,” *Chem. Eng. Sci.*, vol. 93, pp. 229-237 (2013).

[76] P. Song, Z. J. Peng, Y. L. Yue, H. Zhang, Z. Zhang, Y. C. Fan, “Mechanical properties of silicone composites reinforced with micron- and nano-sized magnetic particles,” *Polym. Lett.*, vol. 7, no. 6, pp. 546-553 (2013).

[77] H. Song, M. Tan, T. W. Walker, A. Jander, P. Dhagat, “Planar alignment of magnetic microdisks in composites using rotating fields,” *IEEE Trans. Magn.*, to be published (2015).

[78] J. P. Rich, G. H. McKinley, P. S. Doyle, “Arrested chain growth during magnetic directed particle assembly in yield stress matrix fluids,” *Langmuir*, vol. 28, no. 8, pp. 3683-3689 (2012).

[79] W. Voit, W. Zapka, L. Belova, K. V. Rao, “Application of inkjet technology for the deposition of magnetic nanoparticles to form micron-scale structures,” *IEE Proc.-Sci. Meas. Technol.*, vol. 150, no. 5, pp. 252-256 (2003).

[80] M. Singh, H. M. Haverinen, P. Dhagat, G. E. Jabbour, “Inkjet printing—process and its applications,” *Adv. Mater.*, vol. 22, no. 6, pp. 673-685 (2010).

[81] J. P. Isaza, A. Avila, “Iron microparticle deposition at high concentration,” *Rapid Prototyping J.*, vol. 18, no. 4, pp. 281-286 (2012).

[82] P. Tiberto, G. Barrera, F. Celegato, M. Coïsson, A. Chiolerio, P. Martino, P. Pandolfi, P. Allia, “Magnetic properties of jet-printer inks containing dispersed magnetite nanoparticles,” *Eur. Phys. J. B.*, vol. 86, pp. 173-179 (2013).

[83] H. Song, J. Spencer, A. Jander, J. Nielsen, J. Stasiak, V. Kasperchik, P. Dhagat, "Inkjet printing of magnetic materials with aligned anisotropy," *J. Appl. Phys.*, vol. 115, no. 17, 17E308 (2014).

[84] G. Clay, H. Song, J. Nielsen, J. Stasiak, M. Khavari, A. Jander, P. Dhagat, "3D printing magnetic material with arbitrary anisotropy," *NIP31/Digital Fabrication 2015 Conference Proceedings*, to be published (2015).

[85] H. Song, S. Mulley, N. Coussens, P. Dhagat, A. Jander, A. Yokochi, "Effect of packing fraction on ferromagnetic resonance in $NiFe_2O_4$ nanocomposites," *J. Appl. Phys.*, vol. 111, no. 7, 07E348 (2012).

APPENDICES

Appendix A: Procedures for Preparation of Ni-Fe Microdisk Composites

1) First clean the 2” glass substrates with Acetone, IPA (isopropyl), and DI water. Dehydrate on a hot plate (200 °C) for 10 min.

2) Use Gun #3 of the AJA ATC Orion Sputter System in Microproducts Breakthrough Institute for Al sputtering. The Al target (Kurt J. Lesker Company) is 99.99% pure, with a dimension of 3” in diameter and 0.25” in thickness. When the base pressure reaches 2×10^{-6} Torr or below, load recipe “Han Al gun 3 100”, which sets 5 mTorr operating pressure and 20 sccm Ar flow. Sputter at 300 W power for 700 s to get 100 nm thickness of Al thin film.

3) Expose Al thin films to air for 10 min. The resulted surface oxidation helps prevent the Ni-Fe thin film from peeling off during the wet etch process.

4) Use Gun #4 of the AJA ATC Orion Sputter System in Microproducts Breakthrough Institute (MBI, Corvallis OR) for Ni-Fe sputtering. The Ni-Fe target (Kurt J. Lesker Company) is 81% Ni and 19% Fe, with a purity of 99.5%. The target dimension is 2” in diameter and 0.125” in thickness. When the base pressure reaches 2×10^{-6} Torr or below, load recipe “Han NiFe_150”, which sets 5 mTorr operating pressure and 20 sccm Ar flow. Sputter at 200 W power for 1800 s to get a 150 nm thickness of Ni-Fe thin film.

5) Clean the thin film surface using Step 1 before photolithography.

6) Put the sample on photoresist spinner for 2 min to cool down. Cover the surface with S1818 photoresist, then spin at 4000 rpm for 30 s. Soft bake the sample on hot plate at 115°C for 1 min.

7) Use 5 um dot array (diagonal array) mask for exposure. Clean mask with Acetone, IPA (isopropyl), and DI water before use. Align the sample with the mask, and hard-contact exposure the photoresist for 10 s. Develop the photoresist in 1:4 ratio 351 developer solution (10 mL 315 developer in 40 mL DI water) for 8 s while shaking the developer solution left to right. Rinse the sample with DI water, air blow it dry, and inspect the developed photoresist pattern under an optical microscope.

8) Scrape the 2" sample into 8 pieces for the Ni-Fe wet etch process. Remove the four corners of the sample. Wet etch using 1:4 HNO_3 solution (20 mL HNO_3 and 80 mL DI water) with no agitation for about 2 min. The Ni-Fe thin film color changes from dark silver, to blue/purple, to shiny silver. Just after the blue/purple color is all gone from the surface, take the piece out and rinse with DI water to stop the etching.

9) Remove photoresist with Acetone. Wet etch Al using 1:1 NH_4OH solution (20 mL NH_4OH and 20 mL DI water) with no agitation for 40 min.

10) Put the piece in a 25 mL beaker with about 5 mL DI water in it. Sonicate each piece for 30 s in DI water to release the Ni-Fe microdisks. Transfer the Ni-Fe suspension from the beaker to a 15 mL centrifuge tube. Use DI water to wash the glass pieces and the beaker, and pour it also into the centrifuge tube.

11) Take the centrifuge tube to Dr. Julie A. Greenwood's lab, and use the swing-out centrifuge (eppendorf centrifuge 5804). Put counter balance in the centrifuge. Centrifuge at 3500 rpm for 2 min. Then use pipette (with low retention tips) to draw out most of the DI water, leaving about 50 μL DI water along with Ni-Fe microdisks at the bottom of the tube. Use pipette to draw up and dispense DI water to re-disperse the Ni-Fe microdisks. Then transfer the solution into an ultra-micro cuvette (BrandTech ultra micro UV transparent disposable cuvette, 70 μL, window size 2 mm by 3.5 mm by 10 mm) using the pipette.

12) Fill the 15 mL centrifuge tube with DI water to about 2 mL. Sonicate it to release the Ni-Fe microdisks on the tube wall. Centrifuge it for another 2 min. Use pipette to remove most of the DI water, leaving only 100 μL, and transfer the remaining microdisks into the cuvette.

13) Let the microdisks settle down in the cuvette for 10 min. Use pipette to remove most of the DI water, leaving about 50 μL. Put the cuvette in a Vacuum Chamber, and evaporate the DI water and dry the Ni-Fe microdisks for 12 hours.

14) Add about 30 μL UV-resin (Loctite 3301 and Loctite 3106) into the cuvette, use pipette tip to stir and draw up the resin to mix it with Ni-Fe microdisks.

15) If using the solenoid coil setup, put the cuvette on the rotational stage inside the coil. Use square wave (5 V, 1 kHz, 99% duty) generated by Tektronix AFG3022B arbitrary waveform generator to get a stage rotation speed of 90 rpm (1.5 Hz). Rotate the cuvette while applying the magnetic aligning field, which is powered by KEPCO BOP 20-20ML power supply (voltage mode: 8 V output for 10 mT field). After magnetic alignment, turn on the UV

LEDs (two LZ4-00UA10 UV LEDs, peak wavelength at 400 nm, LED Engin, Inc., CA, USA) for 3 min to cure the composite.

16) If using the two-axis coils setup, put the cuvette in the center inside the coils. Use Tektronix AFG3022B arbitrary waveform generator to control the current outputs of two KEPCO BOP 20-20ML power supplies to generate a rotating magnetic field with certain frequencies and magnitudes. To generate a 100 Hz, 2 mT aligning field, use a 0.492 V amplitude, 100 Hz frequency sine wave on the arbitrary waveform generator for the inner coil, and a 1.042 V amplitude, 100 Hz frequency cosine wave for the outer coil. After the magnetic alignment, turn on the UV LEDs (two LZ4-00U600 UV LEDs, peak wavelength 365 nm, LED Engin, Inc., CA, USA) for 1 min to cure the composite.

17) After curing, use razor blade to cut the composite sample out of the cuvette.

Appendix B: Settings for Optical Imaging of Ni-Fe Microdisk Motion

Nikon Eclipse Ti-S Microscope:

Filters settings: NCB, D filter in, GIF, ND filter out.

Objective lens resolving power: 0.55 μm for 40X, and 1.34 μm for 10X.

In-Plane Coils ((X,Y)-Coils):

Connect two KEPCO BOP 20-20ML power supplies to x-coil and y-coil, respectively. Then connect Tektronix AFG3022B arbitrary waveform generator to the voltage analog control of the two KEPCOs. Apply a sine wave using the arbitrary waveform generator to control voltage output on x-coil, and a cosine wave on y-coil to generate a rotating magnetic field. The sine wave amplitude settings on the arbitrary waveform generator are in Table B.1.

The error of magnetic field magnitude depends on the field uniformity over the sample area, which is measured to be about 5%.

Table B.1 Sine wave amplitude settings on arbitrary waveform generator.

Rotation Frequency (Hz)	Wave Amplitude for X-Coil (V)	Wave Amplitude for Y-Coil (V)
DC-50	0.632	0.640
100	0.816	0.820
200	1.284	1.300
500	2.960	3.000

Perpendicular Coil (Z-Axis Coil):

Use current output of a Keithley 2440 5A sourcemeter to drive the coils. Output 3.3 A for 1 mT magnetic field at the sample area. The error of magnetic field magnitude is about 5%.

Appendix C: Matlab Code for Processing and Analyzing of Magnetic Disk Rotation Videos

Main Matlab Function:

```
function [time, area_norm, algn_time, time_c, area_c, davg,
d_ratio] = ellipse_fit(videoname, bw_level, Setfps, pix_um,
export1, export2)

%
% Input:    videoname   - AVI video file location
%           bw_level    - threshold level for converting the video
to binary (black and white)
%           Setfps      - frame rate in frame/s. Enter 0 to use
the video's nature frame rate
%           pix_um      - conversion ratio from pixel size to
micron
%           export1     - file name of the output video for
monitoring the video processing. Enter '' (blank) to disable it.
%           export2     - file name of the output video for
monitoring the video analysis. Enter '' (blank) to disable it.
%
% Output:   time        - elapsed times for each frame
%           area_norm   - particle projected area smoothed and
normalized to [0,1]
%           algn_time   - time between area_norm = 0.1 and 0.9
%           time_c      - cropped ''time'' output around area_norm
= 0.1 to 0.9
%           area_c      - cropped ''area_norm'' output around
area_norm = 0.1 to 0.9
%           davg        - averaged particle diameter from ellipse
fitting
%           d_ratio     - particle shape imperfection
characterized by the ratio of short axis over long axis on
particle boundary
%

% input the video and read video frame data in RGB scale
```

```
    obj = VideoReader(videoname);
    if Setfps == 0
        fps = round(obj.FrameRate);
    else
        fps = Setfps;
    end
    frame_num = obj.NumberOfFrames;
    height = obj.height;
    width = obj.width;
    time = (1:1:frame_num)/fps;
    hist = read(obj);

% stabilize the video

    for n = 1:frame_num
        hist1(:,:,n) = hist(:,:,1,n);
        hist_temp = double(hist1(:,:,n));
        hist_norm(:,:,n) = uint8(255*mat2gray(hist_temp));
        bw(:,:,n) = im2bw(hist_norm(:,:,n),bw_level);
        bw_edge(:,:,n) = edge(bw(:,:,n),'sobel');
        bw_temp = bw_edge(:,:,n);
        [bw_x,bw_y] = find(double(bw_temp) == 1);
        xmove = round(height/2 - mean(bw_x));
        ymove = round(width/2 - mean(bw_y));
        tform = maketform('affine',[1 0 0; 0 1 0; ymove xmove 1]);
        temp_center = imtransform(hist1(:,:,n), tform, 'XData', [1
width], 'YData', [1 height]);
        max_center = max(max(temp_center));
        temp_center (temp_center == 0) = max_center;
        hist_center(:,:,n) = uint8(temp_center);
    end

% crop the stabilized video around the particle

    crop_length = 100;
    heightc = crop_length;
    widthc = crop_length;
    crop_xmin = round(height/2) - round(crop_length/2);
    crop_ymin = round(width/2) - round(crop_length/2);
```

```
    crop_rect = [crop_ymin crop_xmin crop_length crop_length];

% normalize the pixel values, turn the video into binary, find the
particle boundary, and do an ellipse fitting on the boundary

    for n = 1:frame_num
        hist_crop(:,:,n) = imcrop(hist_center(:,:,n),crop_rect);
        histc_temp = double(hist_crop(:,:,n));
        histc_norm(:,:,n) = uint8(255*mat2gray(histc_temp));
        bwc(:,:,n) = im2bw(histc_norm(:,:,n),bw_level);
        bwc_edge(:,:,n) = edge(bwc(:,:,n),'sobel');
        bwc_temp = bwc_edge(:,:,n);
        [bwc_x,bwc_y] = find(bwc_temp == 1);
        [csize,~] = size(bwc_x);
        for m = 1:csize
            bwc_2d(m,1,n) = bwc_x(m,1);
            bwc_2d(m,2,n) = bwc_y(m,1);
        end
        [ellFit(n), ellFun(:,:,n), ellVert(:,:,n), ellHerz(:,:,n)]
= EllipseFitByGal(bwc_2d(1:csize,2,n),bwc_2d(1:csize,1,n),gca);
        a(n) = ellFit(n).a;
        b(n) = ellFit(n).b;
        r(n) = min(a(n),b(n));
        d(n) = 2 * max(a(n),b(n));
        phi(n) = ellFit(n).phi;
        area(n) = pi*a(n)*b(n);
    end

    davg = max(d) * pix_um;

% calculate d_ratio from particle boundary

    d_max = 0;
    for i = 1:csize
        for j = i:csize
            d_temp = sqrt((bwc_x(i,1)-bwc_x(j,1))^2 + (bwc_y(i,1)-
bwc_y(j,1))^2);
            k_temp = (bwc_y(i,1)-bwc_y(j,1)) / (bwc_x(i,1)-
bwc_x(j,1));
            if d_temp > d_max
```

```
                d_max = d_temp;
                k_max = k_temp;
                i_max = i;
                j_max = j;
            end
        end
    end

    a0 = 1/k_max;
    b0 = 1;
    c0 = - crop_length/2 - crop_length/2/k_max;

    i_min = 1;
    j_min = 1;

    disi_min = d_max;
    for i = 1:csize
        dis_temp = abs(a0*bwc_x(i,1) + b0*bwc_y(i,1) + c0) /
sqrt(a0^2 + b0^2);
        if dis_temp < disi_min
            disi_min = dis_temp;
            i_min = i;
        end
    end

    disj_min = d_max;
    for j = 1:csize
        if j ~= i_min
            dis_temp = abs(a0*bwc_x(j,1) + b0*bwc_y(j,1) + c0) /
sqrt(a0^2 + b0^2);
            dis_2p = sqrt((bwc_x(i_min,1)-bwc_x(j,1))^2 +
(bwc_y(i_min,1)-bwc_y(j,1))^2);
            if dis_temp < disj_min && dis_2p > d_max/2
                disj_min = dis_temp;
                j_min = j;
            end
        end
    end
```

```
    d_min = sqrt((bwc_x(i_min,1)-bwc_x(j_min,1))^2 +
(bwc_y(i_min,1)-bwc_y(j_min,1))^2);

    d_min = d_min * pix_um;
    d_max = d_max * pix_um;
    d_ratio = d_min / d_max;

% particle projected area smoothed and normalized to [0,1]

    area_s = smooth(area,fps);
    area_temp = area - min(area_s(2:end-1));
    area_s = smooth(area_temp,fps);
    area_norm = area_temp / max(area_s(2:end-1));

    for n=1:frame_num
        theta2d(n) = real(acosd((area_norm(n))/(max(area_norm))));
    end

% extract algn_time. crop the area_norm versus time response
around area_norm = 0.1 to 0.9

    [~, index_min] = min(area_norm);
    [~, index_max] = max(area_norm);
    if index_max < index_min;
        limit_l = 0.9;
        limit_r = 0.1;
        [~, index_l] = find(area_norm > limit_l, 1, 'last');
        [~, index_r] = find(area_norm < limit_r, 1, 'first');
        time_le = time(index_l) + (limit_l - area_norm(index_l)) *
(time(index_l) - time(index_l+1)) / (area_norm(index_l) -
area_norm(index_l+1));
        time_re = time(index_r) + (limit_r - area_norm(index_r)) *
(time(index_r) - time(index_r-1)) / (area_norm(index_r) -
area_norm(index_r-1));
    else
        limit_l = 0.1;
        limit_r = 0.9;
        [~, index_l] = find(area_norm < limit_l, 1, 'last');
        [~, index_r] = find(area_norm > limit_r, 1, 'first');
```

```
        time_le = time(index_l) + (limit_l - area_norm(index_l)) *
(time(index_l) - time(index_l+1)) / (area_norm(index_l) -
area_norm(index_l+1));
        time_re = time(index_r) + (limit_r - area_norm(index_r)) *
(time(index_r) - time(index_r-1)) / (area_norm(index_r) -
area_norm(index_r-1));
    end
    algn_time = abs(time_re - time_le);

    time_ext = 1;
    index_ext = time_ext * fps;
    index_lc = max(1, index_l - index_ext);
    index_rc = min(frame_num, index_r + index_ext);

    time_c = time((index_lc) : (index_rc));
    time_c = time_c - min(time_c);
    area_c = area_norm((index_lc) : (index_rc));
    theta2d_c = theta2d((index_lc) : (index_rc));

% output videos for monitoring the video processing and analysis
results

    if ~isempty(export1)
        close all;
        writeObj1 = VideoWriter(export1);
        writeObj1.FrameRate = fps;
        open(writeObj1);

        for n=1:frame_num
            sub1 = subplot(2,2,1);
            imshow(hist1(:,:,n));
            title('Original');

            sub2 = subplot(2,2,2);
            imshow(hist_center(:,:,n));
            title('Centered');

            sub3 = subplot(2,2,3);
            imshow(hist_crop(:,:,n));
```

```
            title('Cropped');

            sub4 = subplot(2,2,4);
            imshow(bwc(:,:,n));
            title('Binary Image');

            M(n) = getframe(gcf);
            writeVideo(writeObj1,M(n));
        end

        close(writeObj1);
    end

    if ~isempty(export2)
        close all;
        writeObj2 = VideoWriter(export2);
        writeObj2.FrameRate = fps;
        open(writeObj2);

        for n=1:frame_num
            sub1 = subplot(2,2,1);
            imshow(hist_crop(:,:,n));
            title('Centered');

            sub2 = subplot(2,2,2);
            imshow(hist_crop(:,:,n));
            hold on;

plot(bwc_2d(:,2,n),bwc_2d(:,1,n),'d','MarkerSize',1,'Linewidth',1)
;
            title('Edge Detection');

            sub3 = subplot(2,2,3);
            plot((widthc-
ellFun(1,:,n)),ellFun(2,:,n),'r','Linewidth',2);
            xlim([0 heightc]);
            ylim([0 widthc]);
            set(sub3, 'XTickLabel', [], 'YTickLabel', []);
            axis square;
```

```
            title('Ellipse Fit');

            sub4 = subplot(2,2,4);
            plot(time(1:n),area_norm(1:n),'Linewidth',2);
            xlim([0 time(frame_num)]);
            ylim([0 1]);
            axis square;
            xlabel('Time (sec)')
            title('cos(theta)');

            M(n) = getframe(gcf);
            writeVideo(writeObj2,M(n));
        end
        close(writeObj2);
    end

   close all;
   plot(time,area_norm)

end
```

Ellipse Fitting Function:

The Matlab code is modified from Ohad Gal's "fit_ellipse.m" function (http://www.mathworks.com/matlabcentral/fileexchange/3215-fit-ellipse).

```
Copyright (c) 2003, Ohad Gal
All rights reserved.

Redistribution and use in source and binary forms, with or without
modification, are permitted provided that the following conditions
are met:

    * Redistributions of source code must retain the above
copyright
      notice, this list of conditions and the following
disclaimer.
```

```
    * Redistributions in binary form must reproduce the above
copyright notice, this list of conditions and the following
disclaimer in the documentation and/or other materials provided
with the distribution

THIS SOFTWARE IS PROVIDED BY THE COPYRIGHT HOLDERS AND
CONTRIBUTORS "AS IS" AND ANY EXPRESS OR IMPLIED WARRANTIES,
INCLUDING, BUT NOT LIMITED TO, THE IMPLIED WARRANTIES OF
MERCHANTABILITY AND FITNESS FOR A PARTICULAR PURPOSE ARE
DISCLAIMED. IN NO EVENT SHALL THE COPYRIGHT OWNER OR CONTRIBUTORS
BE LIABLE FOR ANY DIRECT, INDIRECT, INCIDENTAL, SPECIAL,
EXEMPLARY, OR CONSEQUENTIAL DAMAGES (INCLUDING, BUT NOT LIMITED
TO, PROCUREMENT OF SUBSTITUTE GOODS OR SERVICES; LOSS OF USE,
DATA, OR PROFITS; OR BUSINESS INTERRUPTION) HOWEVER CAUSED AND ON
ANY THEORY OF LIABILITY, WHETHER IN CONTRACT, STRICT LIABILITY, OR
TORT (INCLUDING NEGLIGENCE OR OTHERWISE)ARISING IN ANY WAY OUT OF
THE USE OF THIS SOFTWARE, EVEN IF ADVISED OF THE POSSIBILITY OF
SUCH DAMAGE.

function ellipse_t = EllipseFitByGal( x,y,axis_handle )

%
% fit_ellipse - finds the best fit to an ellipse for the given set
of points.
%
% Format:   ellipse_t = fit_ellipse( x,y,axis_handle )
%
% Input:    x,y         - a set of points in 2 column vectors. AT
LEAST 5 points are needed !
%           axis_handle - optional. a handle to an axis, at which
the estimated ellipse
%                         will be drawn along with it's axes
%
% Output:   ellipse_t   - structure that defines the best fit to
an ellipse
%           a           - sub axis (radius) of the X axis of the
non-tilt ellipse
%           b           - sub axis (radius) of the Y axis of the
non-tilt ellipse
%           phi         - orientation in radians of the ellipse
(tilt)
```

```
%           X0          - center at the X axis of the non-tilt
ellipse
%           Y0          - center at the Y axis of the non-tilt
ellipse
%           X0_in       - center at the X axis of the tilted
ellipse
%           Y0_in       - center at the Y axis of the tilted
ellipse
%           long_axis   - size of the long axis of the ellipse
%           short_axis  - size of the short axis of the ellipse
%           status      - status of detection of an ellipse
%
% Note:     if an ellipse was not detected (but a parabola or
hyperbola), then
%           an empty structure is returned

% initialize
orientation_tolerance = 1e-3;

% empty warning stack
warning( '' );

% prepare vectors, must be column vectors
x = x(:);
y = y(:);

% remove bias of the ellipse - to make matrix inversion more
accurate. (will be added later on).
mean_x = mean(x);
mean_y = mean(y);
x = x-mean_x;
y = y-mean_y;

% the estimation for the conic equation of the ellipse
X = [x.^2, x.*y, y.^2, x, y ];
a = sum(X)/(X'*X);

% check for warnings
if ~isempty( lastwarn )
```

```
    disp( 'stopped because of a warning regarding matrix
inversion' );
    ellipse_t = [];
    return
end

% extract parameters from the conic equation
[a,b,c,d,e] = deal( a(1),a(2),a(3),a(4),a(5) );

% remove the orientation from the ellipse
if ( min(abs(b/a),abs(b/c)) > orientation_tolerance )

    orientation_rad = 1/2 * atan( b/(c-a) );
    cos_phi = cos( orientation_rad );
    sin_phi = sin( orientation_rad );
    [a,b,c,d,e] = deal(...
        a*cos_phi^2 - b*cos_phi*sin_phi + c*sin_phi^2,...
        0,...
        a*sin_phi^2 + b*cos_phi*sin_phi + c*cos_phi^2,...
        d*cos_phi - e*sin_phi,...
        d*sin_phi + e*cos_phi );
    [mean_x,mean_y] = deal( ...
        cos_phi*mean_x - sin_phi*mean_y,...
        sin_phi*mean_x + cos_phi*mean_y );
else
    orientation_rad = 0;
    cos_phi = cos( orientation_rad );
    sin_phi = sin( orientation_rad );
end

% check if conic equation represents an ellipse
test = a*c;
switch (1)
case (test>0),  status = '';
case (test==0), status = 'Parabola found';  warning( 'fit_ellipse:
Did not locate an ellipse' );
case (test<0),  status = 'Hyperbola found'; warning( 'fit_ellipse:
Did not locate an ellipse' );
end
```

```
% if we found an ellipse return it's data
if (test>0)

    % make sure coefficients are positive as required
    if (a<0), [a,c,d,e] = deal( -a,-c,-d,-e ); end

    % final ellipse parameters
    X0          = mean_x - d/2/a;
    Y0          = mean_y - e/2/c;
    F           = 1 + (d^2)/(4*a) + (e^2)/(4*c);
    [a,b]       = deal( sqrt( F/a ),sqrt( F/c ) );
    long_axis   = 2*max(a,b);
    short_axis  = 2*min(a,b);

    % rotate the axes backwards to find the center point of the
original TILTED ellipse
    R           = [ cos_phi sin_phi; -sin_phi cos_phi ];
    P_in        = R * [X0;Y0];
    X0_in       = P_in(1);
    Y0_in       = P_in(2);

    % pack ellipse into a structure
    ellipse_t = struct( ...
        'a',a,...
        'b',b,...
        'phi',orientation_rad,...
        'X0',X0,...
        'Y0',Y0,...
        'X0_in',X0_in,...
        'Y0_in',Y0_in,...
        'long_axis',long_axis,...
        'short_axis',short_axis,...
        'status','' );
else
    % report an empty structure
    ellipse_t = struct( ...
        'a',[],...
        'b',[],...
        'phi',[],...
        'X0',[],...
```

```
        'Y0',[],...
        'X0_in',[],...
        'Y0_in',[],...
        'long_axis',[],...
        'short_axis',[],...
        'status',status );
end

% check if we need to plot an ellipse with it's axes.
if (nargin>2) & ~isempty( axis_handle ) & (test>0)

    % rotation matrix to rotate the axes with respect to an angle
phi
    R = [ cos_phi sin_phi; -sin_phi cos_phi ];

    % the axes
    ver_line        = [ [X0 X0]; Y0+b*[-1 1] ];
    horz_line       = [ X0+a*[-1 1]; [Y0 Y0] ];
    new_ver_line    = R*ver_line;
    new_horz_line   = R*horz_line;

    % the ellipse
    theta_r         = linspace(0,2*pi);
    ellipse_x_r     = X0 + a*cos( theta_r );
    ellipse_y_r     = Y0 + b*sin( theta_r );
    rotated_ellipse = R * [ellipse_x_r;ellipse_y_r];

    % draw
    % hold_state = get( axis_handle,'NextPlot' );
    % set( axis_handle,'NextPlot','add' );
    % plot( new_ver_line(1,:),new_ver_line(2,:),'r' );
    % plot( new_horz_line(1,:),new_horz_line(2,:),'r' );
    % plot( rotated_ellipse(1,:),rotated_ellipse(2,:),'r' );
    % set( axis_handle,'NextPlot',hold_state );
end
end
```

Appendix D: Operation Procedures for Magnetic Printing Setup

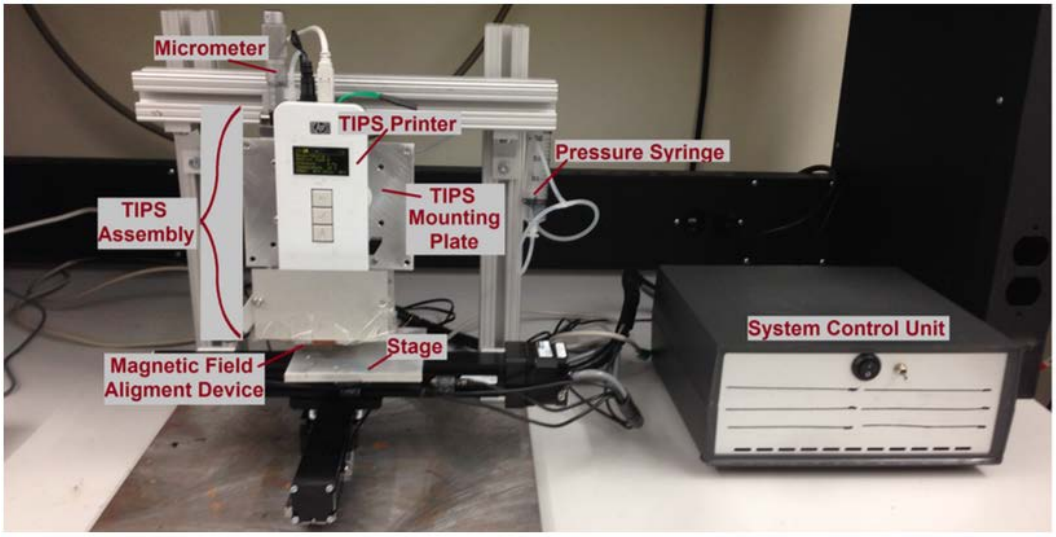

Fig. D.1 Magnetic inkjet printing setup view.

1) Plug in power cable on top of the TIPS controller. Connect x-axis and y-axis KEPCO power supply to the computer with GPIB cables. Connect KEPCO power supply outputs to the corresponding leads of the picture frame electromagnet. Turn on both KEPCO power supplies. Turn on System Control Unit for the XY-Stage.

2) Fill a TIPS printer tip (tip ID: 24) with magnetic ink up to 0.5 mL using a pipette. Slide the tip onto printer until tip ID number lights up on the TIPS printer screen. Check if individual nozzles are working by checking the resistance (normal value: 65-75 Ω).

3) Prime the nozzles by pressing the ink out. Then adjust back-pressure syringe until the pressure on TIPS display reads between 500-1500 Pa.

4) Slide the TIPS printer back into place. Ensure that the tip of the printer slides into the shield. Tighten the screws on the back of the TIPS mounting plate. Tape photo paper flat onto the stage. Adjust TIPS assembly height until the micrometer reads 6 mm.

5) Open MagneticPrinter.vi file from desktop of the control computer. The interface from Fig. D.2 will appear. From their respective selections, choose the following: 1) COM1 under XY-Stage Controller, 2) GPIB0::2::INSTR under X-axis KEPCO, and 3) GPIB0::1::INSTR under Y-axis KEPCO. Start the LabVIEW program.

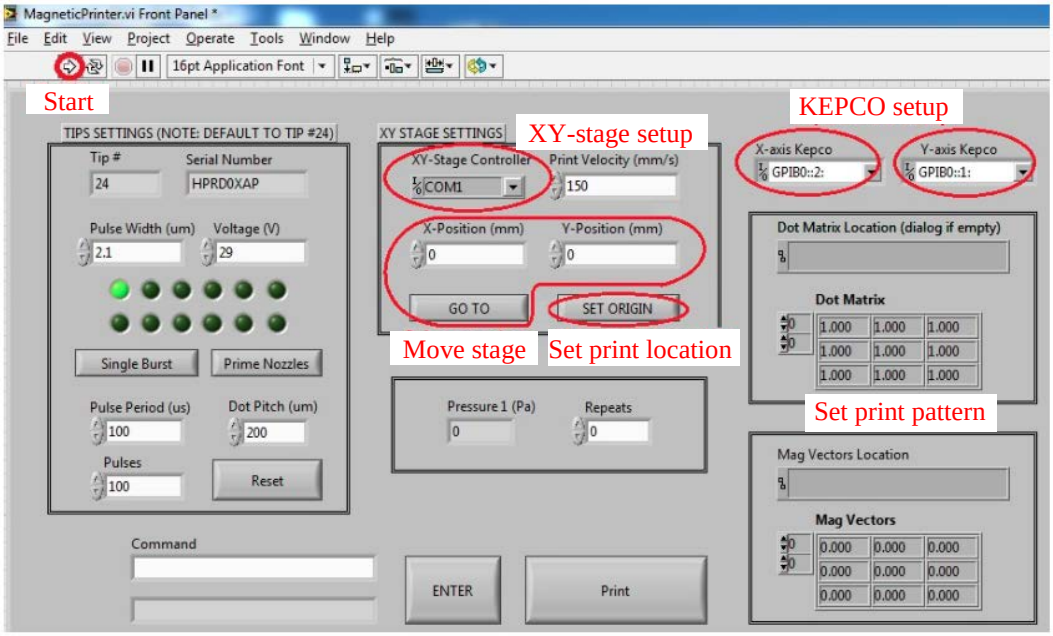

Fig. D.2 Default settings of magnetic printing LabVIEW interface.

6) Move the stage by adjust values in X-Position and Y-Position boxes and hit ”GO TO.” Once find the printing start position, hit ”SET ORIGIN” to set it as the home position. Click “Print” and select the magnetic field vector file from the first popup window, and print pattern file from the second popup window. Ensure pressure stays 500-1500 Pa during printing process.